Alternative Electrochemical Salt Waste Forms, Summary of FY11-FY12 Results

Fuel Cycle Research & Development

Prepared for
U.S. Department of Energy
B.J. Riley, J.S. McCloy, J.V. Crum,
W.C. Lepry, C.P. Rodriguez,
C.F. Windisch Jr., J. Matyas,
M.P. Westman, B.T. Rieck, J.B. Lang,
M.J. Olszta, and D.A. Pierce
Pacific Northwest National Laboratory
January 17, 2014
FCRD-SWF-2013-000025, Rev.1
PNNL-22034

DISCLAIMER

This information was prepared as an account of work sponsored by an agency of the U.S. Government. Neither the U.S. Government nor any agency thereof, nor any of their employees, makes any warranty, expressed or implied, or assumes any legal liability or responsibility for the accuracy, completeness, or usefulness, of any information, apparatus, product, or process disclosed, or represents that its use would not infringe privately owned rights. References herein to any specific commercial product, process, or service by trade name, trade mark, manufacturer, or otherwise, does not necessarily constitute or imply its endorsement, recommendation, or favoring by the U.S. Government or any agency thereof. The views and opinions of authors expressed herein do not necessarily state or reflect those of the U.S. Government or any agency thereof.

SUMMARY

The Fuel Cycle Research and Development Program, sponsored by the U.S. Department of Energy Office of Nuclear Energy, is currently investigating alternative waste forms for wastes generated from nuclear fuel processing. One such waste results from an electrochemical separations process, called the "Echem" process. The Echem process utilizes a molten KCl-LiCl salt to dissolve the fuel. This process results in a spent salt containing alkali, alkaline earth, lanthanide halides and small quantities of actinide halides, where the primary halide is chloride with a minor iodide fraction. Pacific Northwest National Laboratory (PNNL) is concurrently investigating two candidate waste forms for the Echem spent-salt: high-halide minerals (i.e., sodalite and cancrinite) and tellurite (TeO_2)-based glasses. Both of these candidates showed promise in fiscal year (FY) 2009 and FY2010 with a simplified nonradioactive simulant of the Echem waste. Further testing was performed on these waste forms in FY2011 and FY2012 to assess the possibility of their use in a sustainable fuel cycle. This report summarizes the combined results from FY2011 and FY2012 efforts.

The chemical durability results for the tellurite glasses in FY2010 revealed a wide variation of waste form performance in these materials. The most promising glass studied was a lead-tellurite glass formulation with the Echem salt simulant. This glass showed very good chemical durability with a normalized release for sodium of 0.478 g/m^2 following a seven-day product consistency test. With this in mind, the following studies were undertaken in FY2011 and FY2012 to further investigate and optimize this type of glass as a potential waste form:

1) *Expanded study on lead-tellurite glasses*. The lead-tellurite glass system was further investigated to determine the waste-loading limits and assess the tellurium-oxygen bonding structure as a function of waste loading by characterization with nuclear magnetic resonance, Raman spectroscopy, and X-ray diffraction. The Te-O network in tellurite glass is quite complex where at least eight different structures have been presented in the literature and typically include TeO_4, TeO_{3+1}, and TeO_3 structures present in either a trigonal bipyramidal or trigonal pyramidal arrangement. The structural investigation revealed that the medium-range order in the glass decreased and the tellurite network was depolymerized as the waste fraction was increased. It was apparent that glass-network breaking was predominantly caused by the additions of the waste cations and that the presence of chloride may have actually caused some repolymerization of the network by scavenging alkali and preventing it from acting as a network modifier. At the highest waste loadings, the glass became phase-separated, resulting in a Te-rich phase and a Pb-alkali-chloride-rich phase, and some chloride-containing crystals were formed. We also investigated some of the other waste-form related properties of the lead-tellurite glasses, such as the thermal diffusivity, glass transition temperature, crystallization temperature, melting temperature, and mass loss as a function of temperature.

2) *Investigated the glass network structure of P-series glasses from FY2010 with Raman spectroscopy*. Here, we studied the glass structure of the P-series glasses (TeO_2 with various other oxide additions such as ZnO, PbO, P_2O_5, Al_2O_3, B_2O_3, and WO_3); the study provided a preliminary understanding of the various Te-O structural configurations in the literature and how to identify them with Raman spectroscopy. The goal was to correlate a particular Te-O structure with a glass that had high chemical durability and reverse-engineer a glass with very high chemical durability by targeting the preferred structure with changes in composition. This has proved unsuccessful overall, but we did observe some unique frequency bands in the Raman spectra for the lead-tellurite glasses that might be a first step toward better understanding the link between the glass structure and the chemical durability.

3) *Investigated the structural effects of various components in the tellurite glasses*. For this study, we used Raman spectroscopy to look at the structure of simplified glasses in which various components had been removed and added to provide different combinations of the anions and
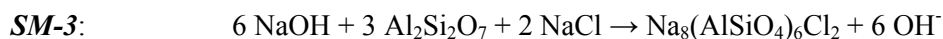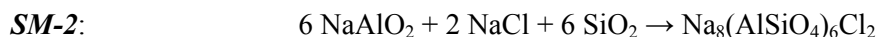
cations. This study provided some very useful information regarding the effects of Cl and alkalis on the tellurite glass network.

4) *Investigated polycrystalline tellurite compounds as a structural surrogate for tellurite glass*. We found a previous study where a large set of tellurite crystals were fabricated and the Te-O structures determined with nuclear magnetic resonance (NMR). Single-phase tellurite crystals have a single type of tellurium-oxygen structure, in contrast with tellurite glasses that have a mixture of different types of Te-O bonding configurations. The goal was to make a series of tellurite crystals from each category and assess the chemical durability of each. In FY2011, we made a series of crystals, some of which were highly phase-pure (>95%). We intended to eventually verify their structure (with NMR and/or Raman spectroscopy) and perform chemical durability tests on them to look for a correlation between the structure and the chemical durability but fabrication was more difficult than expected so budget did not allow for further testing at this point.

For the high-halide minerals, we looked at optimizing a few of the variables in the solution-based process as well as some post-process adjustments to the heat-treatments. These variable studies included the following:

1) *Alternative silica sources*. We fabricated sodalites with an organic source of silica, tetraethyl orthosilicate (TEOS), in place of the colloidal silica. The goal with this substitution was to assess the differences in reaction rates for sodalite formation among the silica sources as well as the differences in sodalite concentration. The change in silica sources resulted in a noticeable improvement from 23.8 mass% sodalite in the S5A specimen with colloidal silica to 95.7 mass% sodalite in the S5C specimen with TEOS.

2) *Alternative 4-coordinated network formers*. We performed the solution-based process with germanium (IV) ethoxide, an organic form of Ge^{4+}, in place of the TEOS to see whether we could fabricate a germanium-based sodalite. The germanium sodalite was targeted because it was predicted to (1) reduce the firing temperature resulting in an increased sodalite concentration because of the reduced chloride volatility (due to lower firing temperature) and (2) increase fired-pellet density improving volumetric waste loading. The high porosity in the initially fired pellets was a deterrent to pursuing this route any further, though we did demonstrate a high germania-based sodalite concentration (82 mass%) in the as-made gel. The high porosity in conjunction with the high cost of germanium (IV) ethoxide led us to abandon this pursuit.

3) *Alternative sintering aids*. We fabricated a series of six alternative sintering aids with different viscosities in order to consolidate the solution-derived powders at a lower temperature, retaining the sodalite structure and preventing chloride volatility. These sintering aids included four sodium borosilicate glasses, a sodium aluminophosphate glass, and a lead-tellurite glass. Each of these glasses was added to a separate batch, as a powder; the gel was dried, specimens from the batches were pressed into pellets, fired at different temperatures, and the phases quantified with X-ray diffraction. The sodium borosilicate glasses dramatically improved the densification ($\leq 96\%$ of theoretical density) of the fired pellets at much-reduced temperatures of ~750 °C, where rather large amounts of sodalite were still produced (70.6 mass%).

4) *Alternative approaches to making sodalite*. In FY2012, we took a different approach to making high density sodalite pellets. Three different solution-based approaches were evaluated to make sodalite with the same simulated XCl_{20} salt. Several aspects were varied during the process including: the reactants, the amount of sintering aid added (0, 5, and 10 mass%), the step in the process when the sintering aid was added, calcination, and the timing of the calcination step in the process. The three sodalite methods (*SM-#*) used in the current study are *SM-1*, *SM-2*, and *SM-3*, simplified below. The equations above are listed with the salt being denoted as "NaCl" but, in fact, the actual salt compositions contain R^{1+}, R^{2+}, and R^{3+} cations so the R:Cl ratio is not 1:1 (R:Cl < 1, by mole). The reactants were added in the proper amounts to obtain the targeted value

for Al:Cl (3:1) and Si:Cl (3:1), on a molar basis, where the alkali fraction (R^{1+}) was intentionally below the target of 4:1 (R^{1+}:Cl) to help influence the incorporation of alkaline earth (R^{2+}) and Ln (R^{3+}) components from the XCl_{20} into the sodalite structure. The results from this study showed that each formulation had advantages and disadvantages where SM-3 pellets had high density and low sodalite production and SM-2 pellets had very high sodalite production with modestly high densities. A mixture of these methods will likely be considered in FY2013.

SM-1: $6 \text{ NaOH} + 6 \text{ Al(OH)}_3 + 2 \text{ NaCl} + 6 \text{ SiO}_2 \rightarrow \text{Na}_8(\text{AlSiO}_4)_6\text{Cl}_2 + 24 \text{ OH}^-$

SM-2: $6 \text{ NaAlO}_2 + 2 \text{ NaCl} + 6 \text{ SiO}_2 \rightarrow \text{Na}_8(\text{AlSiO}_4)_6\text{Cl}_2$

SM-3: $6 \text{ NaOH} + 3 \text{ Al}_2\text{Si}_2\text{O}_7 + 2 \text{ NaCl} \rightarrow \text{Na}_8(\text{AlSiO}_4)_6\text{Cl}_2 + 6 \text{ OH}^-$

CONTENTS

FIGURES

TABLES

ABBREVIATIONS, SYMBOLS, AND NOMECLATURE

α	thermal diffusivity
δ_{iso}	isotropic chemical shift (nuclear magnetic resonance)
$\Delta\delta$	chemical shift anisotropy (nuclear magnetic resonance)
η	asymmetry parameter (nuclear magnetic resonance)
$\tilde{v}$	wavenumbers (cm^{-1}), shift frequency for Raman spectroscopy
ρ	density; ρ_a is the Archimedes density; ρ_b is bulk density; ρ_e is the density of ethanol; ρ_i is the density of the i-th crystalline phase; ρ_{salt} is the density of the XCl_{20} salt; and ρ_t is theoretical density
ρ_{sd}	storage density
$\Delta\sigma$	shielding anisotropy (nuclear magnetic resonance)
aq	aqueous
ASTM	American Society for Testing and Materials, now ASTM International, Inc.
ATEM	analytical transmission electron microscopy
BET	Brunauer-Emmett-Teller
BF	bright field
BSE	backscattered electron (SEM imaging mode)
Cat.	cation
CS	colloidal silica
DOE	U.S. Department of Energy
DF	dark field
DSC	differential scanning calorimetry or differential scanning calorimeter
DTA	differential thermal analysis or differential thermal analyzer
Echem	electrochemical separations process
EDS	energy dispersive spectroscopy
EMSL	Environmental Molecular Sciences Laboratory
EtOH	ethanol
FP	fission products
FTIR	Fourier transform infrared spectroscopy
FY	fiscal year
Ge-EtO	germanium(IV) ethoxide, $Ge(OC_2H_5)_4$
HFE	high-frequency envelope
HT	heat-treatment
ICSD	Inorganic Crystal Structure Database
ISP	isostatic press
K_{gl}	glass formation constant

LFA	laser flash apparatus
LFE	low-frequency envelope
Ln	lanthanides (or rare-earths)
m	mass ratio
M	molar
MAS	magic angle spinning
N/A	not applicable
NBO	non-bridging oxygen
NBS	sodium borosilicate
NL_i	normalized release of element "i" (from the PCT) in g/m^2
NMR	nuclear magnetic resonance
PCT	product consistency test
PDF	powder diffraction file
PNNL	Pacific Northwest National Laboratory
PVS	pressure variation study (pressed sodalite powders into pellets at different pressures)
QU	quenched
R	metal cation (e.g., R^{1+}, R^{2+}, R^{3+})
RDF	radial distribution function
RT	room temperature
SA	sintering aid
SAD	selected area diffraction
SEI	secondary electron imaging (SEM imaging mode)
SEM	scanning electron microscope, scanning electron microscopy
SG	space group
SM	sodalite method (i.e., SM-1, SM-2, and SM-3)
STEM	scanning transmission electron microscopy
TEM	transmission electron microscopy
tbp	trigonal bypyramidal (TeO_4)
T_c	crystallization temperature
T_g	glass transition temperature
T_L	liquidus temperature
T_M	melting temperature
TEOS	tetraethyl orthosilicate, $Si(OC_2H_5)_4$ (also tetraethoxysilane)
TGA	thermogravimetric analysis or thermogravimetric analyzer
tp	trigonal pyramidal (TeO_3)

TPb$_{\#}$ lead tellurite glass where "#" denotes the mass% of added XCl$_{20}$

T_x temperature of the crystallization onset

UAP   uniaxial press

XCl$_{20}$ mixed chloride electrochemical waste stream with 20% FP

XRD   X-ray diffraction, X-ray diffractometer

1   INTRODUCTION

An increased reliance on nuclear power is a likely solution to meet the clean-energy demands of the future (Vienna, 2010). The U.S. Department of Energy's (DOE's) Office of Nuclear Energy Fuel Cycle Research and Development (FCRD) Program is currently in the process of identifying the most efficient pathway for nuclear power production, which will likely involve a series of steps in which the fuel will be reprocessed and the reusable fuel recycled to recover fuel value. The waste from fuel processing will be immobilized in one of several different waste forms. A brief overview of the various types of proposed processing steps and waste streams is presented in our previous work (Riley et al., 2010). One of the separations methods being considered is an electrochemical process. In this method, the fuel is dissolved in molten ionic salts or a LiCl-KCl eutectic, and the resulting "spent salt" will need to be immobilized in a viable waste form. This spent salt is commonly referred to the "Echem salt" and consists primarily of an alkali chloride salt with minor amounts of alkaline earth, transition metal, lanthanide, and actinide chlorides plus a very small fraction of iodide.

The currently assumed waste form for immobilizing this salt waste is a glass-bonded sodalite, nominally $Na_4Al_3(SiO_4)_3Cl$ but often written as $Na_8(AlSiO_4)_6Cl_2$ (Bateman et al., 2007; Ebert, 2005). This baseline waste form is fabricated by mixing zeolite 4A with the salt waste. The salt is occluded in the zeolite at about 500 °C; then the salt containing zeolite is mixed with borosilicate glass in a 3:1 mass ratio. The mixture is transferred to a mold and consolidated at ~915 °C with only slight pressure (a steel plate resting on top). The loading of waste in the zeolite is given by the reaction in Equation (1) below. After the 3:1 blending with borosilicate glass, the loading of fission-product-loaded salt in the final waste form is roughly 7.5 mass%.

$$Na_{12}(AlSiO_4)_{12} + 4\ NaCl \rightarrow 2\ Na_8(AlSiO_4)_6Cl_2 \tag{1}$$

$$(\text{zeolite 4A}) \quad (\text{halite}) \quad\quad (\text{sodalite})$$
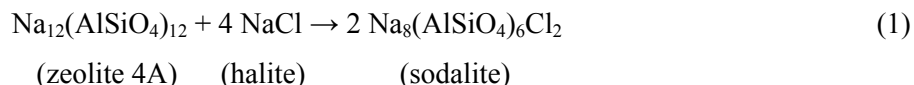
The FCRD program has been supporting the development of alternative waste forms for the Echem salt waste since 2009. Part of that work has been at Pacific Northwest National Laboratory (PNNL), where we are developing a rare type of glass called a tellurite glass and high-halide minerals made with a solution-based process (Crum et al., 2009; Riley et al., 2010).

Tellurite glass has many attractive properties for a waste form, including high halide solubility over a wide range of different and mixed halides, high density (improving volumetric waste loading capacity), and good glass formation with chlorides and many other additives (Vogel et al., 1974; Yakhkind and Chebotarev, 1980). One of the primary drawbacks with these glasses is that they cost more to make than a traditional borosilicate-based glass waste form. Another drawback to these glasses is that since they have not previously been developed for waste form applications, many of the relevant engineering properties are unknown. In our earlier work, we discussed scoping tests for candidate waste form selection and the evaluation of a series of different tellurite glass systems for chemical durability, solubility of the salt waste, and glass properties (Riley et al., 2010). A few of the formulations showed good chemical durability and high waste loading capacity. The work presented here is a continuation of that work along with some additional fabrication and characterization data.

Our work has primarily focused on sodalite. The sodalite structure was identified as one of the naturally occurring structures that contain the waste components, i.e., alkalis and halides. These minerals have been under research for the past several years for incorporating the Echem salt components for the baseline waste form (Bateman et al., 2007; Ebert, 2005) as well as for radioactive iodine (Babad and Strachan, 1980; Koyama, 1994). However, we identified the solution-based process as a potential improvement to the preparation of the sodalites. The solution-based approach was identified because it allows for a near-room temperature aqueous processing route, reducing energy costs. It also allows for complete containment of the waste in a solution versus processing the salt as a powder that can become airborne. The sodalite powders that were formed upon drying were small (~1–5 μm) and thus needed to

be sintered together to form a viable waste form. However, this firing process only yielded pellets that were ~70% dense compared to the theoretical density of sodalite, 2.27×10^3 kg/m^3. Therefore, a sintering aid was added to further densify the pellets. Small additions (2 mass%) of a high-viscosity glass, NBS-1, dramatically increased the density of the pellets to >90% of theoretical density (Vienna et al., 1998).

In FY2010, we assessed the chemical durability of these different waste forms with the Product Consistency Test (PCT)[1] and some of the waste forms we made for each family of materials showed promise. Since both of these waste forms showed good performance in the PCT, they were both candidates for further consideration.

The chemical durability results for the tellurite glasses in FY2010 revealed a wide variety of waste form performance in these materials. The most promising glass studied was a lead-tellurite glass with the Echem salt simulant. This glass showed very good chemical durability: the normalized release for sodium was 0.478 g/m^2 and comparable to borosilicate glasses (Ebert and Wolf, 1999). With this in mind, the following studies were undertaken in FY2011 to further investigate and optimize these glasses as a potential waste form:

1) *Expanded study on lead-tellurite glasses*. The lead-tellurite glass system was further investigated to determine the waste-loading limits and assess the tellurium-oxygen bonding structure as a function of waste loading by characterization with nuclear magnetic resonance, Raman spectroscopy, and X-ray diffraction (XRD). The Te-O network in tellurite glass is quite complex where at least eight different structures have been presented in the literature and typically include TeO_4, TeO_{3+1}, and TeO_3 structures present in either a trigonal bipyramidal or trigonal pyramidal arrangement. The structural investigation revealed that the medium-range order in the glass decreased and the tellurite network was depolymerized as the waste fraction was increased. It was apparent that glass-network breaking was predominantly caused by the additions of the waste cations and that the presence of chloride may have actually caused some repolymerization of the network by scavenging alkali and preventing it from acting as a network modifier. At the highest waste loadings, the glass became phase-separated, resulting in a Te-rich phase and a Pb-alkali-chloride-rich phase, and some chloride-containing crystals were formed. We also investigated some of the other waste-form related properties of the lead-tellurite glasses, such as the thermal diffusivity, glass transition temperature, crystallization temperature, melting temperature, and mass loss as a function of temperature.

2) *Investigated the glass network structure of P-series glasses from FY2010 with Raman spectroscopy*. Here, we studied the glass structure of the P-series glasses (TeO_2 with various other oxide additions such as ZnO, PbO, P_2O_5, Al_2O_3, B_2O_3, and WO_3); the study provided a preliminary understanding of the various Te-O structural configurations in the literature and how to identify them with Raman spectroscopy. The goal was to correlate a particular Te-O structure with a glass that had high chemical durability and engineer a glass with very high chemical durability by targeting the preferred structure with changes in composition. This has proved unsuccessful overall, but we did observe some unique frequency bands in the Raman spectra for the lead-tellurite glasses that might be a first step toward better understanding the link between the glass structure and the chemical durability.

3) *Investigated the structural effects of various components in the tellurite glasses*. For this study, we used Raman spectroscopy to look at the structure of simplified glasses in which various components had been removed and added to provide different combinations of the anions and cations. This study provided some very useful information regarding the effects of Cl and alkali on the tellurite glass network.

---

[1] ASTM C 1285-08. 2008. *Standard Test Methods for Determining Chemical Durability of Nuclear, Hazardous, and Mixed Waste Glasses and Multiphase Glass Ceramics: The Product Consistency Test (PCT)*, American Society for Testing and Materials International, West Conshohocken, PA.

4) *Investigated tellurite crystals as a surrogate for tellurite glass*. In addition to the tellurite glasses, we also looked at some tellurite crystals. The goal of this study was to look at the chemical durability of tellurite compounds that contained only one structural configuration of Te-O. This idea was proposed based on results presented by Sakida et al. (Sakida et al., 1999a). Sakida et al. prepared 21 tellurite crystals, characterized them with [125]Te nuclear magnetic resonance (NMR), and then categorized them based on the structural configuration of the Te present in the crystals (see Figure 1.1). Each of these crystals fell into a particular category defined as TeO_3, TeO_{3+1}, or TeO_4, where TeO_4 structural units were divided into α-TeO_2 and β-TeO_2. Single-phase tellurite crystals have a single type of tellurium-oxygen structure in contrast with tellurite glasses that have a mixed set of most of the different types of structures. The goal was to make a series of tellurite crystals from each category and assess the chemical durability of each. In FY2011, we made a series of crystals, some of which were highly phase pure (>95%). We intend to verify their structure (with NMR and/or Raman spectroscopy) and perform chemical durability tests on them to look for a correlation between the structure and the chemical durability. We wanted to achieve melting so that the chunks could be ground and sieved and a particular size fraction could be retained for chemical durability tests. We had difficulty melting all of the mixtures that we attempted.
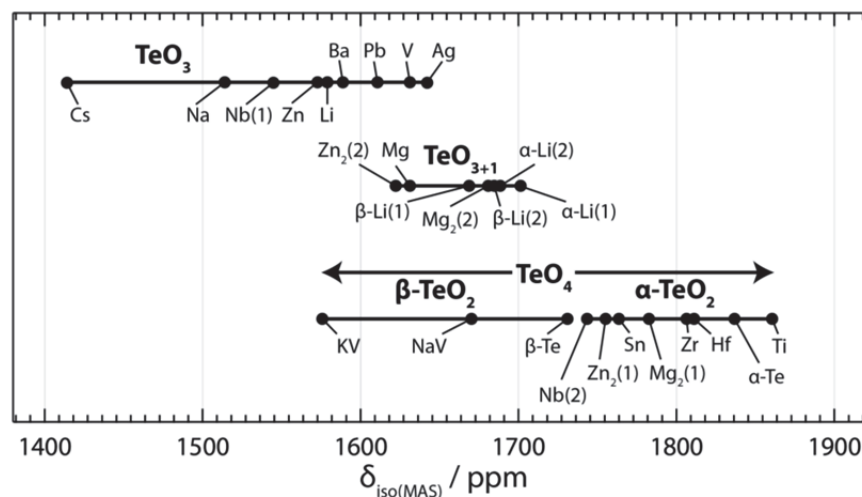
Figure 1.1. Ranges of isotropic chemical shifts (δ_{iso}) for tellurium sites with different structural units determined with [125]Te magic angle spinning (MAS) NMR at 9.4 T – recreated from Sakida et al. (1999a).

For the second candidate waste form, the high-halide minerals, we looked at optimizing a few of the variables in the solution-based process as well as some post-process adjustments to the heat-treatments. These variable studies included the following:

1) *Alternative silica sources*. We fabricated solution-derived sodalites with an organic source of silica, tetraethyl orthosilicate (TEOS), in place of the colloidal silica (CS) (see Figure 1.2a). The goal of this substitution was to assess the differences in reaction rate for sodalite formation between the silica sources as well as the differences in sodalite concentration. The change in silica sources resulted in a noticeable improvement, from 23.8 mass% sodalite in the S5A specimen with CS to 95.7 mass% sodalite in the S5C specimen with TEOS.

2) *Investigated alternative 4-coordinated network formers*. We performed the solution-based process with germanium (IV) ethoxide, an organic form of Ge^{4+}, in place of the TEOS to see whether we could fabricate a germanium-based sodalite (see Figure 1.2b). The germanium sodalite was targeted because it was predicted to (1) reduce the firing temperature resulting in an increased sodalite concentration because of the reduced chloride volatility (due to lower firing temperature) and (2) increase fired-pellet density improving volumetric waste loading. The high porosity in the initially fired pellets was a deterrent to pursuing this route any further, though we did demonstrate a high

germania-based sodalite concentration (82 mass%) in the as-made gel. The high porosity in conjunction with the high cost of germanium (IV) ethoxide led us to abandon this pursuit.
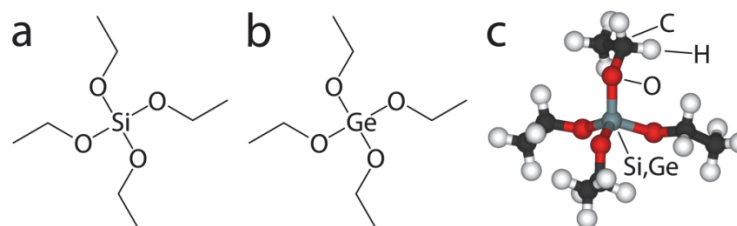
Figure 1.2. (a) Hydrocarbon stick figure of TEOS, (b) hydrocarbon stick figure of germanium(IV) ethoxide, and (c) a three-dimensional view of these structures. *Note: for (a) and (b), the atom located at each bend and terminal is a C atom where each C has four total bonds achieved with hydrogen atoms in areas where oxygen is not present.*

3) *Alternative sintering aids*. We had success in FY2010 with the NBS-1 glass, but due to the high viscosity of this glass, the temperatures required for pellet densification were rather high (850 °C) and that led to chloride volatility, evidenced by a decrease in the sodalite concentration (Vienna et al., 1998). We fabricated a series of six alternative sintering aids with different viscosities in order to consolidate the solution-derived powders at a lower temperature, retaining the sodalite structure and preventing chloride volatility. These sintering aids included four sodium borosilicate glasses, a sodium aluminophosphate glass, and a lead-tellurite glass. Each of these glasses was added to a separate batch, as a powder; the gel was dried, specimens from the batches were pressed into pellets, fired at different temperatures, and the phases quantified with XRD. The sodium borosilicate glasses dramatically improved the densification (up to 96% of theoretical density) of the fired pellets at much-reduced temperatures of ~750 °C, where rather large amounts of sodalite were still produced (70.6 mass%).

4) *Alternative approaches to making sodalite*. In FY2012, we took a different approach to making high density sodalite pellets. Three different solution-based approaches were evaluated to make sodalite with the same simulated XCl_{20} salt. Several aspects were varied during the process including: the reactants, the amount of sintering aid added (0, 5, and 10 mass%), the step in the process when the sintering aid was added, calcination, and the timing of the calcination step in the process. The three sodalite methods (*SM-#*) used in the current study are *SM-1*, *SM-2*, and *SM-3*, simplified below. The equations above are listed with the salt being denoted as "NaCl" but, in fact, the actual salt compositions contain R^{1+}, R^{2+}, and R^{3+} cations so the R:Cl ratio is not 1:1 (R:Cl < 1). The reactants were added in the proper amounts to obtain the targeted value for Al:Cl (3:1) and Si:Cl (3:1) where the alkali fraction (R^{1+}) was intentionally below the target of 4:1 (R^{1+}:Cl) to help influence the incorporation of alkaline earth (R^{2+}) and Ln (R^{3+}) components from the XCl_{20} into the sodalite structure. The results from this study showed that each formulation had advantages and disadvantages where SM-3 pellets had high density and low sodalite production and SM-2 pellets had very high sodalite production with modestly high densities. A mixture of these methods will likely be considered in FY2013.

SM-1: $\qquad 6\ NaOH + 6\ Al(OH)_3 + 2\ NaCl + 6\ SiO_2 \rightarrow Na_8(AlSiO_4)_6Cl_2 + 24\ OH^-$ $\qquad$ (2)

SM-2: $\qquad\qquad 6\ NaAlO_2 + 2\ NaCl + 6\ SiO_2 \rightarrow Na_8(AlSiO_4)_6Cl_2$ $\qquad\qquad$ (3)

SM-3: $\qquad 6\ NaOH + 3\ Al_2Si_2O_7 + 2\ NaCl \rightarrow Na_8(AlSiO_4)_6Cl_2 + 6\ OH^-$ $\qquad\qquad$ (4)
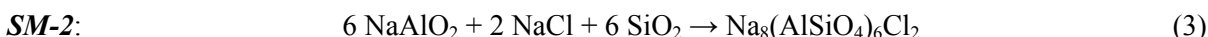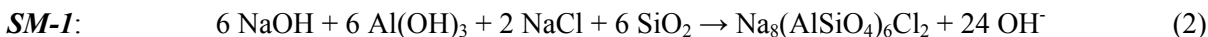
2   EXPANDED BACKGROUND AND APPROACH

The simulated (nonradioactive) waste composition used in this study is the 20 mass% fission-products (FP) waste stream (Yoo, 2009) as presented in Table 2.1. The 20 mass% FP Echem waste stream is

designated in this report as XCl_{20} and was discussed in more detail in our previous publications (Crum et al., 2009; Riley et al., 2010).

Table 2.1. Calculated composition of spent electrochemical salt with 20 mass% FP (XCl_{20}) (Yoo, 2009).

Element	Mole Fraction	Mass Fraction
Y	0.0007	0.0020
La	0.0029	0.0127
Ce	0.0045	0.0195
Pr	0.0022	0.0095
Nd	0.0067	0.0301
Pm	0.0003	0.0011
Sm	0.0020	0.0092
Eu	0.0002	0.0011
Gd	0.0002	0.0011
Tb	0.0000	0.0001
Li	0.2219	0.0477
K	0.1603	0.1942
Na	0.0630	0.0449
Rb	0.0006	0.0017
Cs	0.0081	0.0332
Sr	0.0013	0.0036
Ba	0.0030	0.0129
Cl	0.5212	0.5725
Total	1.0000	1.0000
Simplified	Mole Fraction	Mass fraction
Alkali	0.4539	0.3217
Alkaline Earth	0.0044	0.0166
Lanthanide	0.0198	0.0863
Halide	0.5219	0.5754

This waste stream was simplified by combining minor components into major like components to allow for easier batching. This simplified waste stream along with some ionic radii from the literature are shown in Table 2.2 (Shannon, 1976). The changes included the following:

- Y, Tb, actinides (not shown due to low levels), and minor lanthanides (Pm, Gd, Eu) were grouped into the Nd component – the only lanthanides used in this study were La, Ce, Pr, Nd, and Sm
- The Rb component was grouped in with the Li component
- Sr was grouped in with Ba

Table 2.2. Elemental composition of proposed spent electrochemical salt containing 20 mass% fission products, denoted as XCl_{20}. Also presented are the ionic radii (in picometers) for the XCl_{20} components (as well as Te^{4+} and Pb^{2+} for the tellurite glasses) along with the coordination number (CN) of these ions (Shannon, 1976).

Salt Waste	XCl_{20}		Ionic radius, r_{ion}		
Component	Mole%	Mass%	Cation	r_{ion} (pm)	CN
LiCl	46.82	29.89	Li^+	59.0	IV
KCl	33.83	37.99	K^+	137	IV
NaCl	13.30	11.71	Na^+	99	IV
CsCl	1.54	3.91	Cs^+	167	VI
$NdCl_3$	1.42	5.36	Nd^{3+}	98.3	VI
$CeCl_3$	0.95	3.51	Ce^{3+}	101	VI
$BaCl_2$	0.64	2.01	Ba^{2+}	135	VI
$LaCl_3$	0.62	2.29	La^{3+}	103.2	VI
$PrCl_3$	0.46	1.72	Pr^{3+}	99	VI
$SmCl_3$	0.42	1.61	Sm^{3+}	95.8	VI
Total	100.00	100.00	Cl^-	181	VI
Simplified (by Group)			Te^{4+}	52	III
Alkali	45.39	32.17	Te^{4+}	66	IV
Alkaline earth	0.44	1.66	Pb^{2+}	98	IV
Lanthanide	1.98	8.63	Pb^{2+}	119	VI
Halide	52.19	57.54			

2.1 High-Halide Minerals: Background and Literature Survey

It is not as easy to incorporate radionuclides into a ceramic waste form as it is to incorporate them into a glass, a more forgiving host network. The incorporation of waste radionuclides in a ceramic waste form is limited to two options, in which (1) a radionuclide is actually incorporated into the structure of the ceramic material at a specific atomic position in the periodic structure or (2) a radionuclide is captured by the non-radioactive phase (Ewing et al., 1995). In order for option (1) to be possible, the radionuclide properties must be suitable for incorporation into the ceramic crystal structure imposed by the coordination polyhedra, which include specific size, charge, and bonding constraints. Clearly, the requirements on a target ceramic waste would have to include the ability to accommodate a variety of atomic substitutions of varying sizes and charges to allow for charge balance in the structure. Considering option (2), a common approach has been to immobilize individual grains of radioactive phases in a ceramic phase such as TiO_2 or Al_2O_3 that have high chemical durability.

To start this study, a literature survey was conducted to identify naturally occurring minerals that are high in halides and/or alkali oxides (see Table 2.3) (Crum et al., 2009). When comparing the candidate minerals listed in Table 2.3, pyrosmalite-(Mn) (formerly manganpyrosmalite) and brokenhillite both contain significant concentrations of Cl; however, the lack of alkali compromises their ability to be good candidates for the spent salt. Wadalite (sodalite group) is a closer compositional match to the spent salt, but again the lack of alkali in this mineral means it is not the most ideal candidate for immobilizing the cation fraction of the waste. According to the list in Table 2.3, the best candidate materials for both the Cl^- and the alkali are sodalite, apatite, and cancrinite (quadridavyne).

Table 2.3. Naturally occurring minerals investigated as potential waste forms (Mineralogy Database, 2011). The theoretical waste loading limits (in mass%) for each mineral type based on Cl or alkali (on Na basis) are listed in parentheses and are adjusted based on the fraction of the alkali in the waste versus the fraction coming from the reactants (e.g., $NaAlO_2$).

Mineral Name	Mineral Group	Chemical Formula	Cl	Alkali
Pyrosmalite-(Mn)	Pyrosmalite	$(Mn,Fe^{2+})_8Si_6O_{15}(OH,Cl)_{10}$	29.30 (51)	0.00 (0)
Wadalite	Sodalite	$Ca_6Al_5Si_2O_{16}Cl_3$	13.40 (23)	0.00 (0)
Brokenhillite	Pyrosmalite	$(Mn,Fe)_{32}(Si_{24}O_{60})OH_{29}Cl_{11}$	9.06 (16)	0.00 (0)
Quadridavyne	Cancrinite	$(Na,K)_6Ca_2Al_6Si_6O_{24}Cl_4$	13.20 (23)	12.84 (27)
Chorapatite	Apatite	$(Na,Ca)_5(PO_4)_3Cl$	8.14 (14)	26.41 (16)
Sodalite	Sodalite	$Na_8Al_6Si_6O_{24}Cl_2$	7.32 (13)	18.98 (15)

Apatites follow the composition of $R_5(YO_4)_3X$ where "R" can be any number of atoms, i.e., R^{1+}, R^{2+} or R^{3+}; "Y" (not yttrium) is P, Si, V, or Os; and "X" is F, Cl, I, OH, or O (Dong et al., 2002; Park et al., 2002). This suggests a wide range of compositional flexibility in which R could be anything from alkalis (R^{1+}) to alkaline earths (R^{2+}) to lanthanides (R^{3+}), all of which are components of the waste, although the alkaline earths are the most commonly found cations to occupy these sites in naturally occurring apatites. Typical apatites found in nuclear waste solids are lanthanide (Ln) silicate isomorphs of the natural apatite that have a composition of $Ca_{4-x}Ln_{6+x}(SiO_4)_6(PO_4)_yO_2$ where the actinides can readily substitute for the lanthanides. Also, iodide is expected to be present in small fractions in the waste stream and could also be incorporated into an iodoapatite structure. Apatites have a few drawbacks. One is the low waste loading by mass (see Table 2.3). Another is their ability to become amorphous after radioactive decay that induces microcracking from volume expansion (Weber et al., 1979). A detailed presentation of these radiation-induced changes can be found elsewhere (Ewing et al., 1995). Vance and coworkers (2012) investigated apatites as a waste form for a similar waste and had problems getting the apatite structure to accommodate all of the waste cations. Apatites have not yet been studied at PNNL for this waste stream but will likely be studied in the future.

All of the work at PNNL has focused on sodalite and cancrinite mineral structures. Based on the literature, sodalite is more likely to form when the only anion present is Cl⁻. If significant concentrations of CO_3^{2-}, NO_3^-, or OH⁻ are present, then cancrinite can become the preferred structure (Liu et al., 2007; Ocanto et al., 2008; Ocanto et al., 2009). In FY2010, we made changes to the solution chemistry in an attempt to form cancrinite in place of sodalite and we had limited success as presented in our previous work (Riley et al., 2010). The additions of NO_3^-, CO_3^{2-}, and OH⁻ were examined to determine which, if any, would form cancrinite instead of sodalite, since cancrinite has a higher theoretical waste loading (23 mass%) than sodalite (13 mass%). The targeted compositions for sodalite synthesis are given in Table 2.4. The XCl_{20} salt composition used in these experiments is presented in Table 2.5. Note: the method for cancrinite mineral synthesis is presented in our earlier work (Riley et al., 2010).

The FY2009 scoping studies showed that sodalite can be easily synthesized with a solution-based process (Crum et al., 2009). However, it is produced in the form of a fine powder with particle sizes on the order of a few microns; the small particle size produced by this technique makes it necessary to treat the powders to form a monolith. In this study, the powders were pressed into pellets (19–25 mm diameter, 5–10 mm thick) and fired to achieve the desired bulk density (>90% of theoretical density). Sodalite was the predominant structure that formed during the solution-based process during the scoping studies of FY2009. Cancrinite, while identified as the best candidate mineral in terms of maximum waste loading, was produced during the process but converted to sodalite upon firing.

Table 2.4. Target elemental compositions of sodalite formulations (in molar formula units), glass sintering aids, and waste loading (mass % addition to original composition). The "Label" is used to identify the samples in later sections. "Ln" denotes the addition of lanthanides. Here, "CS" is colloidal silica, "TEOS" is tetraethyl orthosilicate, and "Ge-EtO" is germanium(IV) ethoxide.

Label: Component/Property	Ideal Sodalite	S5A Series	S5C Series	S5D Series	S6 Series
Alkali	**8.0**	7.9	7.9	7.9	7.9
Al	**6.0**	6.0	6.0	6.0	6.0
Si/Ge	**6.0**	6.0	6.0	6.0	6.0
Si/Ge additive	-	CS	TEOS	Ge-EtO	CS
Alkaline earth + Ln	-	0.1	0.1	0.1	0.1
Cl^-, NO_3^-	**2.0**	2.0	2.0	2.0	2.0
O	**24.0**	24.0	24.0	24.0	24.0
Glass sintering aid, mass%	-	-	5[*]	-	1.0–7.0[†]
Total	**46.0**	46.0	46.0	46.0	46.0
Waste loading, mass%	-	13.7	13.7	10.7	12.7–13.5

*Sintering aids listed Table 3.2 (other than NBS-1) were used. [†]NBS-1 glass was used.

Table 2.5. Elemental composition of proposed spent electrochemical salt containing 20 mass% fission products.

Component	Mass Fraction	Conc. (g/L)	M (moles/L)
KCl	0.3799	68.4327	0.9179
LiCl	0.2985	53.7685	1.2683
NaCl	0.1171	21.0941	0.3609
$NdCl_3$	0.0537	9.6632	0.0386
CsCl	0.0395	7.1180	0.0423
$CeCl_3$	0.0352	6.3449	0.0257
$LaCl_3$	0.0229	4.1324	0.0168
$BaCl_2$	0.0202	3.6315	0.0174
$PrCl_3$	0.0169	3.0455	0.0123
$SmCl_3$	0.0160	2.8809	0.0112
Sum:	1.0000	180.11	2.7116

The FY2010 efforts focused on two areas that include 1) increasing the bulk density of the sodalite waste form and 2) synthesis of a cancrinite waste form (Riley et al., 2010). To increase bulk density of the sodalite, the firing temperature was varied to determine the maximum firing temperature above which the volatility of Cl became significant. First, the optimum firing temperature was determined based on bulk density, Cl loss, and PCT response. Second, a sintering aid (1–7 mass%) was added in the form of powdered borosilicate glass (NBS-1, see Table 3.2) (Vienna et al., 1998). The powdered glass was added during the process, directly after gel formation before the gel was dried.

Results in FY2010 showed that full density was achieved in Sodalite 5A at 950 °C. By adding the NBS-1 glass sintering aid, we showed that similar density could be achieved at 850 °C. However, the small crystallite grain sizes resulted in PCT responses that were higher than expected for the waste form. In

general, in terms of phase assemblages, we saw that as firing temperature was increased, the concentrations of unreacted salts and zeolite phases were reduced. In some cases, sodalite increased as the unreacted salt and zeolite disappeared; however in most cases, this resulted in the formation of sodium aluminosilicates, e.g., nepheline and carnegieite. The sodium aluminosilicates are higher temperature phases than zeolites or sodalites, and thus both of these phases can convert to sodium aluminosilicates with increased heat-treatment temperature.

In FY2012, three different solution-based approaches were employed to make the sodalite waste forms with the same simulated XCl_{20} salt. Several aspects were varied during the process including: the reactants, the amount of sintering aid added, the step in the process when the sintering aid was added, calcination, and the timing of the calcination step in the process. The three sodalite methods (*SM-#*) used in the current study are *SM-1*, *SM-2*, and *SM-3*, simplified in Equations (2)–(4), above.

Equations (2)–(4) are listed with the XCl_{20} denoted as "NaCl" but, in fact, the actual salt compositions contain R^{1+}, R^{2+}, and R^{3+} cations so the R:Cl ratio is not 1:1 (by mole). The reactants were added in the proper amounts to obtain the targeted value for Al:Cl (3:1) and Si:Cl (3:1) on a molar basis where the alkali fraction (R^{1+}) was intentionally below the target of 4:1 (R^{1+}:Cl) to help influence the incorporation of alkaline earth and Ln XCl_{20} components into the sodalite structure. In our previous work we speculated that the alkaline earth and/or lanthanide (Ln) fraction could theoretically be incorporated into the sodalite structure but subsequently we have not observed this to be the case (Riley et al., 2012a).

2.2 Tellurite Glasses: Background

Tellurite glass was selected as the glass candidate host family for the XCl_{20} waste components in FY2009 because these glasses showed promise for moderate-to-high mass% loadings of up to ~15 mass% XCl_{20} and had very high volumetric waste loading—or storage density, ρ_{sd}—due to the high density of normal tellurite glass, $\rho_{sd} > 5 \times 10^3$ kg/m^3 (Crum et al., 2009).

The tellurite glass compositions that we fabricated in FY2009 covered a broad compositional space, were not optimized, and did not have high chemical durability. Thus, to better evaluate these glasses as a potential waste form, a literature study was conducted in FY2010 to identify promising candidate formulations for further investigation (Riley et al., 2010). This was followed up with a scoping study in which glasses were fabricated on a small scale (~5 g) to evaluate the glass formation ability with and without the XCl_{20} simulant. The scoping study was designed to assess some basic properties of a wide variety of simple tellurite glass compositions; these glasses were designated "S-series" glasses.

From the scoping studies, five systems were identified for further investigation and included tellurite glasses with the following additives: PbO, Al_2O_3+B_2O_3, WO_3, P_2O_5, and ZnO. The successful formulations with these five systems were then made in 20-g batches and further characterized; these 20-g batches were designated "P-series" glasses. The P-series glasses were then characterized with assessments of a few of the properties including the following: volatility and pour viscosity during the melting process, density, microstructure, and chemical durability (assessed with the PCT). A summary of the characterization results from these 20-g glasses is presented in Table 2.6. As seen in Table 2.6, some of the properties for the P-series glasses varied widely, especially the volatility and the chemical durability. The lead-tellurite glasses performed the best and were further investigated in FY2011 and FY2012. The primary goals with this expanded study were to look at the glass structure and waste loading limits for the lead-tellurite system.

Table 2.6. Summary results for the P-series tellurite glasses that were analyzed with the PCT. The "Glass" column lists those glasses batched on a 20-g scale for the PCT. Batch composition of each glass is listed in mass% additive; the balance is TeO_2. The composition of XCl_{20} is found in Table 2.1. The melting temperature is denoted T_M. The "volatility" is ranked based on degree of "fuming" observed during the melt process, from none (0) to a lot (4). Viscosity (η) was estimated as compared to standards. The overall deviation associated with the density measurements is $\pm0.015\times10^{-3}$ kg/m^3 (Riley et al., 2010). Phase separation was determined based on visual ("Bulk") and microscopy ("Small") observations. The normalized sodium release during the PCT is given as (NL_{Na}).

Glass ID	Batch Composition (mass% additive)	T_M (°C)	Volatility (0–4)	η (cP)	$\rho_b\times10^{-3}$ (kg/m³)	Phase Separation Bulk	Phase Separation Small	NL_{Na} (g/m²)
P-8	22.0% PbO	705	0	50–100	6.12	-	✔	-
P-11	19.8% PbO, 10.0% XCl_{20}	705	1	10	5.16	-	-	0.478
P-7	8.8% Al_2O_3, 9.0% B_2O_3	720	0	200	4.44	-	✔	-
P-2	7.9% Al_2O_3, 8.1% B_2O_3, 10.0% XCl_{20}*	690	3	50	4.13	✔	✔	6.71
P-9	25.0% WO_3	725	0	100	5.92	✔	-	-
P-12	22.5% WO_3, 10.0 XCl_{20}	675	4	10	5.11	✔	-	10.3
P-5	8.9% P_2O_5	675	0	400	5.11	-	-	-
P-14	8.1% P_2O_5, 10.0% XCl_{20}	675	2	50–100	4.72	✔	✔	86.0
P-4	18.0% ZnO	730	0	100	5.49	-	-	-
P-13	16.2% ZnO, 10.0% XCl_{20}	730	1	10	4.67	-	-	88.9

*The composition of the Echem salts was batched with a different XCl_{20} (XCl_y) in glass P-2 (Riley et al., 2010).

3   METHODS

3.1   High-Halide Minerals

3.1.1   Solution-Based Fabrication Method for Halide Minerals in FY2010-FY2011

Unique identifiers were applied to the various sets of high-halide minerals that we studied in FY2011 and are presented in Table 3.1. A solution-based process was used to form the high-halide minerals, followed with cold pressing and firing to convert the dried gel into a monolithic waste form. Figure 3.1 shows a schematic of the experimental apparatus; these are the steps taken during the process:

1) Simulated spent salt (XCl$_{20}$, see Table 2.1) was dissolved in deionized water (DIW) – see Figure 3.1-(A).

2) Dissolved salt was heated to ~65±5 °C in the reaction beaker, which was heated by an oil bath (Figure 3.1). The solution was continuously stirred with a serpentine Pt wire throughout the formation process.

3) The silica (SiO$_2$) or germania (GeO$_2$) source was slowly added as a separate solution to the dissolved salt solution—see Figure 3.1-(B). The Si-O or Ge-O source is designated in Table 2.4 for each sample series.

4) The solution was then gelled by slow addition of sodium aluminate solution—see Figure 3.1-(C).

5) For some of the batches, a sintering aid (1–7 mass%) was added at this stage in the form of powder (not shown in Figure 3.1). See Table 3.2 for a list of the sintering aids studied along with the glass compositions and a few properties.

6) The gel was stirred and heated for 10–30 min to drive off excess water.

7) Lastly, the gel-containing beaker was heated at 105 °C overnight to complete the drying process.

The dried material was a moderately bound fine powder. The amounts of waste simulant, colloidal silica, and sodium aluminate added were determined by the target waste form composition.

Table 3.1. Labels for the various sets of high-halide minerals fabricated in FY2011. Here, CS, TEOS, and Ge-EtO denote that samples were made with colloidal silica, tetraethyl orthosilicate, and germanium(IV) ethoxide, respectively. See Table 2.4 for the S5A and S6A compositions.

Sample series	Description
S5A-CS	Samples were made with the 5A composition and CS as the 4-coordinated Group IV component
S5C-TEOS	Samples were made with the 5A composition and TEOS as the 4-coordinated Group IV component
S5D-GeEtO	Samples were made with the 5A composition and Ge-EtO as the 4-coordinated Group IV component
S6A-CS	Samples were made with the 5A composition and CS as the 4-coordianted Group IV component but the NBS-1 glass binder was added
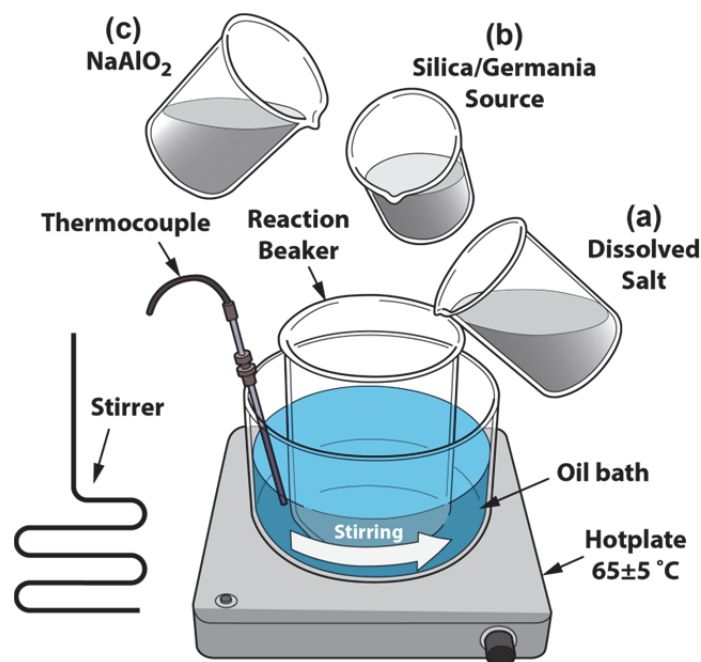
Figure 3.1. Schematic of the simplified solution-based process.

For the silica-based sodalites that were made with TEOS as the silica source, a representative process included the following:

1) Added 30.0 mL of salt solution (see Table 2.5) to a 250 mL beaker with a platinum stirring rod
2) Added 52.8 mL of TEOS to the beaker (99.0% purity, Sigma-Aldrich, St. Louis, MO)
3) Added 51.0 mL of NaAlO$_2$ (38% solution, USALCO, LLC, Baltimore, MD)
4) Added 13.8 mL of absolute ethanol
5) Added 2.05 g of glass (on a 5 mass% basis)
6) After the glass was added, the viscosity greatly increased to form a solid in an exothermic reaction (~30 seconds)
7) Beaker was placed in a special drying oven overnight.
8) The resulting product was powdered and pressed into pellets for analysis.

The glass sintering aids that we studied in FY2011 are presented in Table 3.2. The sodium borosilicate glass sintering aids, denoted as SA-###, were selected based on their lower melting temperatures and were labeled based on the predicted temperatures (~700, 750, 800, and 850 °C) at which the viscosity was predicted to be 100 Pa·s with SciGlass models (v 7.0, ITC, Inc., Newton, MA). The NaAlP-B4 is discussed in detail elsewhere (Donald et al., 2007) and P-8 is a tellurite glass discussed here as well as in our previous work (Riley et al., 2010). The NaAlP-B4 glass was selected based on past success as a sintering aid for an apatite mineral waste form (Donald et al., 2007). The P-8 glass is one of the tellurite glasses discussed here that was selected because it has a high affinity for the Echem salts and a good chemical durability (Riley et al., 2010). Each of these binders was fabricated with a melt-quench technique and then powdered for addition in Step 5, above.

Table 3.2. Compositions (in mass%) of glass sintering aid (SA) additions tested in FY2011. The NBS-1 (Vienna et al., 1998) glass from FY2010 studies is listed for comparison purposes (Riley et al., 2010). Also, some properties are listed and include the temperature at which the viscosity is 100 Pa·s, the melting temperature (T_M), and the bulk density measured with a helium pycnometer. Some of the data was not available for TePbO (TPb$_0$) or NaAlP-B4 for comparison, e.g., T_L represents the liquidus temperature, in place of the T_M for NaAlP-B4.

Components	NBS-1	SA-700	SA-750	SA-800	SA-850	NaAlP-B4	TePbO
SiO_2	60.00	28.57	40.83	42.5	48.31	-	-
Na_2O	15.00	38.32	37.49	32.88	34.89	40.0	-
B_2O_3	10.00	33.11	21.68	24.62	16.80	2.0	-
Li_2O	5.00	-	-	-	-	-	-
Al_2O_3	5.00	-	-	-	-	19.0	-
ZrO_2	5.00	-	-	-	-	-	-
P_2O_5	-	-	-	-	-	39.0	-
TeO_2	-	-	-	-	-	-	78.00
PbO	-	-	-	-	-	-	22.00
T @ 100 Pa·s	963	700	751	805	850	(b)	<600[a]
T_M, °C	1250[a]	850	900	950	1000	742 (T_L)	650[a]
ρ_b, ×10^3 kg/m^3	2.561	2.527	2.542	2.551	2.544	(b)	6.169

(a) These values are estimated
(b) These values are unknown

3.1.2 Solution-Based Fabrication Method for Halide Minerals in FY2012

This following section outlines the approach for making the SM-# sodalites in FY2012. Some of the precursor solutions were heated to assist dissolution of the solute in the solvents. However, the individual precursor solutions were not actively heated during the mixing process. Several different processing combinations were studied and included the following:

(1) The sample was made and dried
(2) The sample was dried and calcined at 600 °C
(3) The sample was dried, calcined at 600 °C, a sintering aid was added dry, and mixed
(4) A sintering aid was added to the solution-based process as a final step, mixed in, and the sample was dried

A sintering aid (SA-800, Table 3.2) was added to the solution-based process as a final step, mixed in, the sample was dried, and then calcined at 600 °C.

Table 3.3. Sample name designations for solution-derived sodalites in FY12.

Designation	Experimental Details
SM#-AM	As made and dried (no binder added during solution process)
SM#-AM-C	SM#-AM is dried and calcined at 600 °C for 3 h in air
SM#-5%	SM#-AM is prepared with 5% sintering aid added during solution process and dried
SM#-AM-5%	5% sintering aid is added to dried SM#-AM
SM#-5%-C	SM#-5% is calcined at 600 °C for 3 hours in air and milled
SM#-C-5%	5% sintering aid is added to dried SM#-AM-C
SM#-10%	SM#-AM is prepared with 10% sintering aid added during solution process and dried
SM#-AM-10%	10% sintering aid is added to dried SM#-AM
SM#-10%-C	SM#-10% is calcined at 600 °C for 3 hours in air and milled
SM#-C-10%	10% sintering aid is added to dried SM#-AM-C
SM#-VS	SM#-5%-C samples that were pressed at different pressures

*All samples were milled prior to pellets being pressed. In each case except SM#-VS, these samples were pressed at 3.5×10^8 Pa (5.0×10^4 PSI). All %'s are by mass.

3.1.2.1   Gibbsite Process (SM-1, Equation (2))

For this technique, 21.538 g of gibbsite powder, $Al(OH)_3$ (<8 µm, NOAH Technologies Corporation, San Antonio, TX), was mixed in a 150 mL beaker containing 50 mL of 5.52 M NaOH (Fisher Scientific, Pittsburgh, PA) at 70±5 °C for 1 h. Heating was applied to assist in $Al(OH)_3$ dissolution but the sample was not completely dissolved after this duration as was expected based on pH-temperature solubility limitations according to the literature (Li et al., 2005; Misra, 1970). In a separate 250 mL beaker, 30 mL of the $X\text{Cl}_{20}$ salt solution (Table 2.5) was added along with 39.72 mL of LUDOX® HS-40 colloidal silica (40 mass% solids, Sigma-Aldrich, St. Louis, MO) solution and stirred for 5 min. Next, the $Al(OH)_3$-NaOH solution was added to the salt-colloidal silica solution and mixed for 1 h without active heating. In some samples, a sintering aid was added during the last 5 minutes of mixing. The sample was then dried in an oven at 105 °C overnight. Once dry, the sample was ground in a tungsten carbide mill for 4 minutes to create a homogeneous product.

3.1.2.2   Sodium Aluminate Process (SM-2, Equation (3))

For this technique, 22.598 g of sodium aluminate powder, $NaAlO_2$ (Riedel-de Haën, Germany), was added to 75 mL of deionized water in a 150 mL beaker and stirred overnight at 70±5 °C covered with a watch glass to minimized evaporation of the water. In a separate 250 mL beaker, 30 mL of the $X\text{Cl}_{20}$ salt solution (Table 2.5) was added and 39.72 mL of LUDOX HS-40 colloidal silica solution was added to the $X\text{Cl}_{20}$ salt solution and stirred for 5 min. Next, the $NaAlO_2$ solution was added to the XCl-SiO_2 solution and mixed for 1 hour. In some samples, a sintering aid was added during the last 5 minutes of mixing. The sample was then dried overnight at 105 °C in an oven. Once dry, the sample was ground in a tungsten carbide mill for 4 minutes to create a homogeneous product.

3.1.2.3   Metakaolin Process (SM-3, Equation (4))

For this technique, kaolin clay (Sigma-Aldrich) was heat treated at ~850 °C for 17 h in air to convert to metakaolin ($Al_2Si_2O_7$) through the dehydroxylation process as described in Equation 5 (Konan et al., 2009). The $Al_2Si_2O_7$ was analyzed with XRD and found to be amorphous as is consistent with the literature (Konan et al., 2009). Once converted, 30.667 g of $Al_2Si_2O_7$ was added to 50 mL of 5.52 M NaOH while mixing and heating at 70±5 °C for one hour. Finally, 30 mL of the $X\text{Cl}_{20}$ salt solution (Table 2.5) was added and the solution was mixed for 1 h. In some samples, a sintering aid was added during the

last 5 minutes of mixing. The sample was then dried in an oven at 105 °C overnight then ground for 4 minutes in a tungsten carbide mill.

$$2 \ Al_2Si_2O_5(OH)_4 \xrightarrow{850 \ °C} 2 \ Al_2Si_2O_7 + 4 \ H_2O \tag{5}$$
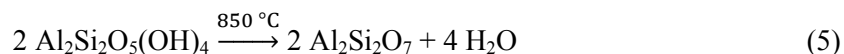
3.1.2.4 Measuring Solution pH

For each of these processes, the pH was monitored with a probe and digital readout that were calibrated with standards. Equilibration times were ~1–5 min. As a check, pH paper was also used to confirm.

3.1.3 Pellet Preparation

Once the samples were ground to a powder, in some cases, the sintering aid was added (dry) at this stage and the samples were homogenized again in the mill. Then, specimens were weighed, pressed into pellets with a combination of techniques. In order to keep the starting pellet dimensions similar and aid in post-processing comparisons, in all cases a total mass of ~2.5 g of powder were added (including sintering aid if added dry). The raw or mixed powders were loaded into a cylindrical die, placed in a uniaxial press (UAP) at room temperature, and pressed to the minimum pressure required to form and maintain a pellet shape of ~21.4 mm diameter and ~4–5 mm thick, i.e., 2.5×10^7 Pa (3.6×10^3 pounds per square inch or PSI). Higher applied pressures at this stage were attempted in our previous work and led to distortions in pellet dimensions after firing (Riley et al., 2010). Pellets were then isostatically pressed (ISP) at room temperature at 3.4×10^8 Pa (5.0×10^4 PSI).

3.1.4 Firing Pellets

The pellets were then placed on a dense alumina sintering plate and loaded into a Lindberg furnace (Thermal Product Solutions, Rochester, NY). Specimens were fired by ramp heating at 1 °C min^{-1} up to the maximum firing temperature of interest (i.e., 650, 750, 850, or 950 °C), held for 8 h, and then furnace cooled at ~10 °C min^{-1}. Some specimens were calcined at 600 °C for 3 hours, at different steps in the process before firing, in order to evaluate the effect of calcination on bulk density of the waste form.

3.1.5 Cold-Pressing Pressure Variation Study (PVS) and Evaluation of Method Accuracy

After the results from the SM-# pellets were analyzed, a set of conditions was selected for further tests to assess the accuracy of the sodalite and density measurements as well as the effect of pressing pressure on the properties of the pellets fired at different temperatures. Each selected specimen from the original batch for this sub-study was run in triplicate to assess the variability in the sodalite and density measurements. The specimens selected for this study were those from SM-1, SM-2, and SM-3 where 5% of SA800 sintering aid was added at the end of the solution-based process, the samples were then dried, calcined, and fired; these specimens were SM1-5%-C-850°C, SM2-5%-C-850°C, and SM3-5%-C-750°C, respectively. Four different pressures were used for making the pellets and included (1) 1.2×10^7 Pa UAP (1.8×10^3 PSI), (2) 2.5×10^7 Pa with UAP, (3) 2.5×10^7 Pa with UAP + 1.7×10^8 Pa with ISP (2.5×10^4 PSI), and (4) 2.5×10^7 Pa with UAP + 3.4×10^8 Pa with ISP.

3.1.6 Spark Plasma Sintering

Specimens of SM1-5%-C-850°C, SM2-5%-C-850°C, and SM3-5%-C-750°C were pressed at 2.5×10^7 Pa with UAP and then hot-pressed with spark plasma sintering at California Nanotechnologies (Cerritos, CA) using a SPS-515S (DR.SINTER LAB, Fuji Electronic Industrial Co., Japan). Specimens were heated in graphite dies at a heating rate of ~50–60°C/min with a hold at 200 °C for degasing and held there until the vacuum level equilibrated. Then, the specimens were heated manually until the displacement of the die push rod either plateaued or started to drop with increased heating. This occurred at ~554, ~526, and ~551 °C for the three specimens, respectively, at which point they were subjected to ~52 MPa. Each sample was heated at these temperatures for ~10 min and then cooled to room temperature.

3.2 Tellurite Glasses

All of the tellurite glasses discussed here were batched from oxides, boric acid, and chlorides of high purity (all > 99% pure). The XCl_{20} components that were added to the waste-loaded glasses were added in the ratios presented in Table 3.4. In all cases, the raw materials were mixed in a mortar and pestle, the powders were then placed in a Pt/10%Rh crucible with a Pt/10%Rh lid, melted for 30 minutes, and quenched by pouring on a stainless steel plate. The as-quenched glasses were subsequently prepared for various tests. The variables in the fabrication parameters included the batch mass and the melting temperature (T_M). The glasses discussed below are grouped into different sections based on the purpose of study and include the following: 1) compositional variation study glasses, 2) lead-tellurite variation study glasses, and 3) structural investigation study glasses. The specific values used for the compositional variation study glasses are presented in Table 2.6 and are listed separately in the text for each set of glasses.

Table 3.4. Composition of the XCl_{20} salt added to the tellurite glasses along with the melting temperatures for some of the components (in order of mass fraction from largest to smallest). The melting temperature (T_M) and bulk density (ρ_b) are also included for each (Haynes, 2011).

Component	Mass%	Mole%	T_M, °C	ρ_b, ×10^{-3} kg/m^3
KCl	37.99	33.83	771	1.99
LiCl	29.89	46.82	610	2.07
NaCl	11.71	13.30	801	2.17
NdCl$_3$	5.36	1.42	759	4.13
CsCl	3.91	1.54	646	3.99
CeCl$_3$	3.51	0.95	807	3.97
LaCl$_3$	2.29	0.62	858	3.84
BaCl$_2$	2.01	0.64	961	3.90
PrCl$_3$	1.72	0.46	786	4.00
SmCl$_3$	1.61	0.42	682	4.46

The naming convention of the glasses presented in the FY2010 report was changed in this report to make it easier to track the glass by composition as opposed to tracking the glasses by the sequential-numbering sample identification. However, both of these naming conventions are retained here for cross-referencing to our other work (see Table 3.5).

3.2.1.1 Compositional Variation Study Glasses

The glasses for the compositional variation study include ten "P-# series" glasses that were fabricated in FY2010 and were previously discussed in our FY2010 report, but were renamed here for easier cross-reference to the glass compositions (Table 3.5) (Riley et al., 2010). The structural characterizations of these glasses, i.e., XRD and Raman spectroscopy, will be discussed in section 4.3.1 in more detail. All of these glasses were fabricated on a 20 g scale and T_M values are listed in our FY2010 report.

Table 3.5. Compositions (in mole%) from tellurite glass compositional variation study batched with and without XCl_{20} additions.* These values are also presented in mass% in our earlier work (Riley et al., 2010), although they are presented here as mole% because that is more appropriate for the discussion of the glass structure. Each of the "+Cl" glasses were batched with a target of 10 mass% XCl_{20}-loading.

Composition Glass ID	Pb P-8	Pb+Cl P-11	Al/B P-7	Al/B+Cl P-2	W P-9	W+Cl P-12	P P-5	P+Cl P-14	Zn P-4	Zn+Cl P-13
TeO_2	83.2	64.8	70.5	59.4	81.3	63.1	90.0	71.2	69.9	56.9
PbO	16.8	13.1	-	-	-	-	-	-	-	-
Al_2O_3	-	-	11.8	10.0	-	-	-	-	-	-
B_2O_3	-	-	17.7	14.9	-	-	-	-	-	-
WO_3	-	-	-	-	18.7	14.5	-	-	-	-
P_2O_5	-	-	-	-	-	-	10.0	7.9	-	-
ZnO	-	-	-	-	-	-	-	-	30.1	24.5
$BaCl_2$	-	0.142	-	0.192	-	0.144	-	0.134	-	0.119
$CeCl_3$	-	0.210	-	0.245	-	0.212	-	0.198	-	0.175
CsCl	-	0.342	-	0.611	-	0.346	-	0.322	-	0.286
KCl	-	7.50	-	8.06	-	7.60	-	7.07	-	6.27
$LaCl_3$	-	0.138	-	0.160	-	0.139	-	0.130	-	0.115
LiCl	-	10.4	-	3.48	-	10.5	-	9.78	-	8.68
NaCl	-	2.95	-	2.38	-	2.99	-	2.78	-	2.47
$NdCl_3$	-	0.315	-	0.372	-	0.319	-	0.297	-	0.263
$PrCl_3$	-	0.102	-	0.119	-	0.104	-	0.0963	-	0.0855
$SmCl_3$	-	0.0925	-	0.111	-	0.0936	-	0.0871	-	0.0773

*A different XCl_{20} composition was used for the Al/B+Cl glass than for the other XCl_{20}-containing glasses (Riley et al., 2010).

3.2.1.2 Lead-Tellurite Waste-Loading Variation Study Glasses

The second set of tellurite glasses fabricated and studied in FY2011 was a series of lead-tellurite glasses with a fixed target TeO_2:PbO ratio (by mass) of 3.5455 and a fixed target ratio of Te:Pb (by mole) of 4.9583, both based on the P-8 and P-11 glasses. This glass system was chosen based on the chemical durability of these glasses according to the FY2010 results. The fraction of XCl_{20} added to the baseline lead-tellurite glass (TPb_0) was varied from 0 to 22.5 mass%. The compositions of these glasses are listed in Table 3.6, in which the ratios between the XCl_{20} components can be extrapolated from Table 3.5. All of these glasses were fabricated in 30-g batches and melted at 700 °C for 30 minutes. It is worth noting that the TPb_{14} glass was batched two times to verify the properties due to some anomalies in the data for this glass.

Table 3.6. Compositions of lead-tellurite variation study glasses in both mass% and mole%. The subscripts on the glass identification (ID) represent the XCl_{20}-loading in mass%. TPb_0 and TPb_{10} represent compositions similar to P-8 and P-11, respectively, from previous work (Riley et al., 2010) but these glasses were all melted at 700 °C and with a different target mass (30 g vs. 20 g). The sequential glass numbering identification, or "Alternate ID", is also provided for tracking purposes.

Glass ID	Alternate ID	Mass%			Mole%		
		TeO_2	PbO	XCl_{20}	TeO_2	PbO	XCl_{20}
TPb_0	T2G-21	78.0	22.0	0.0	83.2	16.8	0.0
TPb_5	T2G-22	74.1	20.9	5.0	73.3	14.8	11.9
TPb_{10}	T2G-23	70.2	19.8	10.0	64.8	13.1	22.1
$TPb_{12.5}$	T2G-24	68.3	19.2	12.5	60.9	12.3	26.8
TPb_{14}	T2G-31	67.1	18.9	14.0	58.7	11.8	29.5
TPb_{15}	T2G-26	66.3	18.7	15.0	57.3	11.5	31.2
$TPb_{17.5}$	T2G-25	64.4	18.1	17.5	53.9	10.9	35.2
$TPb_{22.5}$	T2G-30	60.5	17.0	22.5	47.7	9.6	42.7

3.2.1.3 Structural Variation Study Glasses

The last series of tellurite glasses, the structural variation study glasses, was designed to provide better insight into the effects of composition on the glass structure. Several different sets of glasses were fabricated in which various components were altered individually, in most cases. These different sets of glasses are presented and discussed below.

Set 1: TeO_2:PbO. The purpose of these glasses was to investigate the glass formation in lead-tellurite glasses with a lower mass fraction of PbO than that used for the lead-tellurite variation study glasses, i.e., 22 mass% PbO (with a TeO_2 balance) where TeO_2:PbO = 3.545 (by mass). The compositions of this set of glasses are presented in Table 3.7.

Table 3.7. Compositions for T2G-21, T2G-21b, T2G-21c, and T2G-21d (in mole%) in which the mass% of PbO was 22, 20, 18, and 16 mass%, respectively. The baseline glass for this series is T2G-21, listed in bold type.

Glass ID:	**T2G-21**	T2G-21b	T2G-21c	T2G-21d
TeO_2	**83.22**	84.83	86.43	88.01
PbO	**16.78**	15.17	13.57	11.99
$m(TeO_2:PbO)$	**3.55**	4.00	4.56	5.25
M(Pb:Te)	**0.202**	0.179	0.157	0.136

Set 2: PbO/$PbCl_2$. The purpose of this study was to look at the structural effect of the anion in the lead-tellurite glasses where lead was added as either PbO or $PbCl_2$ and the Te:Pb molar ratio was fixed at 0.202, to match that of T2G-21 (TPb_0), where "Pb" = total Pb. This variation method was chosen so the amount of Te and Pb atoms interacting in the glass would be equivalent between the glasses. These compositions are presented in Table 3.8.

Table 3.8. Composition of PbCl$_2$-PbO compositional variation glasses to study the structural effect of the anion in the lead-tellurite glasses. For all of the glasses in this series, the molar ratio, *M*, of Pb:Te was fixed at 0.202. The baseline glass, T2G-21, is listed in bold type for reference.

Glass ID:	**T2G-21**	T2G-32	T2G-33
		Mole%	
TeO$_2$	**83.22**	83.22	83.22
PbO	**16.78**	-	8.39
PbCl	**-**	16.78	8.39
		Mass%	
TeO$_2$	**78.00**	74.00	75.95
PbO	**22.00**	-	10.71
PbCl	**-**	26.00	13.34
M(Pb:Te)	**0.202**	0.202	0.202

Set 3: *X*O$_{20}$ versus *X*Cl$_{20}$. The purpose of this study was to look at the glass structural effect of the *X*Cl$_{20}$ anions. Thus, for T2G-34, all of the *X*Cl$_{20}$ components were replaced by the oxide versions where the cation ratios (by mole) were maintained from the 5 mass% *X*Cl$_{20}$-loaded glass, T2G-22, and the *X*O$_{20}$-loaded glass. Thus, ratios of Te and Pb to each of the waste component cations, (Cat.), remained fixed between the two glasses, i.e., Te:Cat. and Pb:Cat., respectively. The ratio of Te and Pb to the total moles of the waste component cations were fixed at 6.16 and 1.24, respectively, for both T2G-22 and T2G-34. The compositions, corresponding ratios, and the *X*O$_{20}$ composition are presented in Table 3.9.

Table 3.9. Summary of compositions for the waste-component-anion substitution glasses as well as the composition of *X*O$_{20}$ with values sorted by mole%. T2G-34 was fabricated from oxide versions of the chloride waste components in which the same total waste component cations (Cat.) were identical to the equivalent glass batched with the chloride components, T2G-22, thus T2G-22 serves as a reference for this study. Thus, the ratios of Te:Cat and Pb:Cat were fixed at 6.16 and 1.24, respectively. As with the other lead-tellurite glasses, the Pb:Te ratio for these glasses was fixed at 0.202.

Glass ID:	**T2G-22**	T2G-34	Component	Mole%	Mass%
	Mass%		Li$_2$O	46.5	19.09
TeO$_2$	**74.1**	74.6	K$_2$O	33.6	43.48
PbO	**20.9**	21.0	Na$_2$O	13.2	11.25
*X*Cl$_{20}$	**5.0**		Cs$_2$O	1.53	5.93
*X*O$_{20}$		4.4	Nd$_2$O$_3$	1.41	6.51
	Mole%		BaO	1.27	2.68
TeO$_2$	**73.3**	77.9	Ce$_2$O$_3$	0.940	4.24
PbO	**14.8**	15.7	La$_2$O$_3$	0.617	2.76
*X*Cl$_{20}$	**11.9**		Pr$_2$O$_3$	0.458	2.08
*X*O$_{20}$		6.4	Sm$_2$O$_3$	0.414	1.98
M(Pb:Te)	**0.202**	0.202			
M(Te:Cat.)	**6.16**	6.16			
M(Pb:Cat.)	**1.24**	1.24			

Set 4: PbO-KCl/K$_2$O and Set 5: ZnO-KCl/K$_2$O. The purpose of these studies was to compare the structural differences between PbO/ZnO glasses with additions of potassium as either a chloride or an oxide. The purpose of adding potassium as either KCl or K$_2$O was to determine the anion effect on the structure. For each of these sets (PbO or ZnO), the ratios between the metal additive and TeO$_2$ were kept constant from the original P-series glasses and the K:Te and K:M (where M = Pb,Zn) ratios were also kept constant for each system. The PbO (P-8 and P-11) and ZnO (P-4 and P-13) glasses performed very differently during the PCT and this study was designed to investigate the possibility of structural differences in these more simple glass formulations (Table 2.6). Compositions for the PbO and ZnO glasses are presented in Table 3.10 and Table 3.11, respectively.

Table 3.10. Compositions for T2G-27a, T2G-27b, T2G-29a, and T2G-29b anion variation glasses (in mole%) as well as the mass ratio of TeO$_2$:PbO. Here, m and M denote ratios by mass and moles, respectively. The baseline P-series glasses for this variation study, P-8 and P-4, are listed in bold type.

Glass ID:	**P-8**	T2G-27a	T2G-27b
TeO$_2$	**83.22**	76.47	70.73
PbO	**16.78**	15.42	14.27
K$_2$O	**-**	8.11	-
KCl	**-**	-	15.00
m(TeO$_2$:**PbO**)	**3.55**	3.55	3.55
M(**Pb**:Te)	**0.202**	0.202	0.202
M(K:Te)	**-**	0.212	0.212
M(K:**Pb**)	**-**	1.05	1.05

Table 3.11. Compositions for T2G-29a and T2G-29b anion variation glasses (in mole%) as well as the mass ratio of TeO$_2$:PbO. Here, m and M denote ratios by mass and moles, respectively. The baseline P-series glasses for this variation study, P-8 and P-4, are listed in bold type.

Glass ID:	**P-4**	T2G-29a	T2G-29b
TeO$_2$	**69.91**	66.23	62.92
ZnO	**30.09**	28.51	27.08
K$_2$O	**-**	5.26	-
KCl	**-**	-	10.00
m(TeO$_2$:ZnO)	**4.56**	4.56	4.56
M(Zn:Te)	**0.430**	0.430	0.430
M(K:Te)	**-**	0.159	0.159
M(K:Zn)	**-**	0.369	0.369

3.3 Tellurite Crystal Fabrication

We selected twelve tellurite crystals to fabricate from the list put forth by Sakida and coworkers (1999a), and they are listed in Table 3.12. The list we selected included a few of the crystals from each category (see Figure 1.1). We made a few assumptions regarding the methods for fabricating these crystals based on the methods proposed by Sakida et al. because of missing details in the published methods. The assumptions and comments are as follows:

- Sakida et al. did mention that they had melted (M) the reactants in Table 3.12 at a particular temperature but they did not report the dwell time for the melt at that temperature. Therefore, we assumed the dwell time of 1 h to be sufficient for this process. Further, they either cooled the

- melt to room temperature (**RT**) or quenched (**QU**) it but did not report the cooling rate. In this context, we assumed that a cooling rate of 5 °C/min should be sufficient.
- Sakida et al. did not list the crucible type that they used. We assumed that a platinum alloy crucible and lid would be sufficient.
- Sakida et al. added small quantities of Fe_2O_3 (0.3 mole%) to their batches to improve the NMR signal to noise ratio by shortening the relaxation times of Te nuclei with $I = \frac{1}{2}$. We also did this.

Table 3.12. Tellurite crystals selected for fabrication at PNNL from the list proposed by Sakida et al. (1999a). Multiple steps are numbered for some of the crystals. Crystals in **bold** and *italics* show similar amorphous structure for the TeO_3-isolated and α-TeO_2 units, respectively (see Figure 3.2). The methods listed here were those that proved successful by Sakida et al. "HT" stands for heat-treatment. *Note: All crystals listed here also have an additional 0.3 mol% Fe_2O_3 added to shorten the relaxation time for the Te nuclei with $I = \frac{1}{2}$ during NMR analysis.*

Type	Crystal	Starting Materials	Temp. (°C)/HT time (h)	Powder Diffraction File (PDF) Reference
TeO_3-isolated	**$PbTeO_3$**	TeO_2, PbO, Fe_2O_3	**(1)** 850(M)/1 → **RT** **(2)** 450(**10**) → **RT**	(Sciau et al., 1986)
	Li_2TeO_3	TeO_2, Li_2CO_3, Fe_2O_3	850(M)/1 → **RT**	(Folger, 1975a)
	$ZnTeO_3$	TeO_2, ZnO, Fe_2O_3	**(1)** 1200(M)/1 → **QU** **(2)** 650(**6**) → **RT**	(Hanke, 1967)
	$BaTeO_3$	TeO_2, $BaCO_3$, Fe_2O_3	1200(M)/1 → **RT**	(Folger, 1975b)
TeO_3-terminal	$Cs_2Te_2O_5$	TeO_2, Cs_2CO_3, Fe_2O_3	550(M) → **RT**	(Loopstra and Goubitz, 1986)
	$Te_2V_2O_9$	TeO_2, V_2O_5, Fe_2O_3	**(1)** 650(M)/1 → **RT** **(2)** 430(**12**) → **RT**	(Darriet and Galy, 1973)
TeO_{3+1}	$Zn_2Te_3O_8$	TeO_2, ZnO, Fe_2O_3	**(1)** 850(M)/1 → **QU** **(2)** 650(**7**) → **RT**	(Hanke, 1966)
	$Mg_2Te_3O_8$	TeO_2, MgO, Fe_2O_3	**(1)** 1200(M)/1 → **QU** **(2)** 650(**7**) → **RT**	(Tromel and Ziethen-Reichnach, 1970)
α-TeO_2	*$SnTe_3O_8$*	TeO_2, SnO_2, Fe_2O_3	650(**85**) → **RT**	(Meunier and Galy, 1971)
	$ZrTe_3O_8$	TeO_2, ZrO_2, Fe_2O_3	650(**65**) → **RT**	(Meunier and Galy, 1971)
	$TiTe_3O_8$	TeO_2, TiO_2, Fe_2O_3	650(**85**) → **RT**	(Meunier and Galy, 1971)
β-TeO_2	$NaVTeO_5$	TeO_2, Na_2CO_3, V_2O_5, Fe_2O_3	**(1)** 600(M)/1 → **RT** **(2)** 500(**4**) → **RT**	(Darriet et al., 1972)

M: melting (time = 1–2 h)
RT: room temperature with a cooling rate of 1 °C/min)
QU: quenched
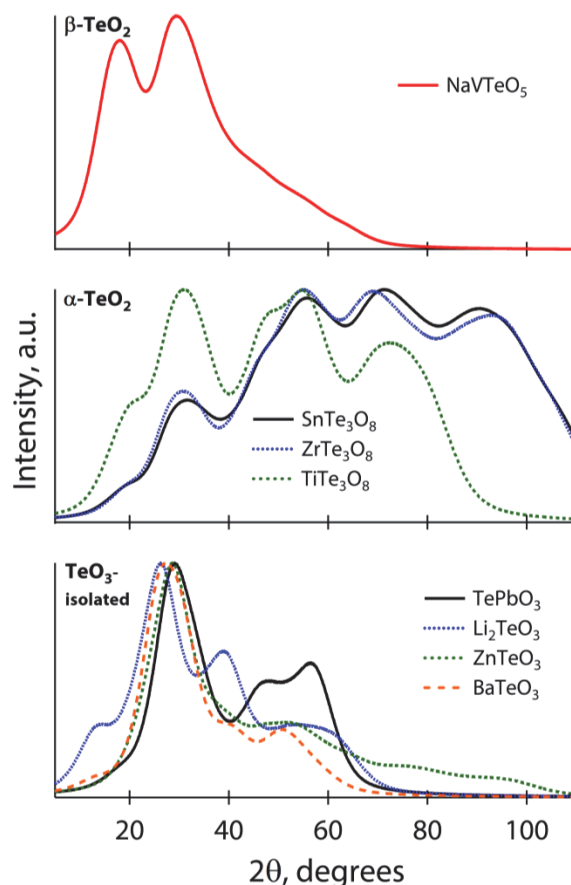
Figure 3.2. Simulated amorphous patterns of a few tellurite crystals. These patterns were generated in JADE by setting the crystallite size to 10 Å and putting 0% strain on the network. These were used to predict the amorphous structure of the crystalline compounds.

3.4 Waste Form Characterization

3.4.1 Optical Microscopy and Photo-Documentation

Specimen microstructure was analyzed with Olympus SZH10 and Olympus PMG-3 optical microscopes. In some cases, polished cross-section of the glasses were observed in reflected or transmitted light, depending on the opacity of the specimen, but most of the time, the glasses were observed as-quenched. Low-magnification optical micrographs and photographs (both in color) were collected of the bulk glasses, of the crucible, and of the pour plate surface for process comparisons between compositions, with a Canon T1i camera (Canon U.S.A., Inc., Lake Success, NY).

3.4.2 Helium Pycnometry – Density Measurements for Tellurite Glasses

The density of each tellurite glass for PCT measurements was measured with a Micromeritics AccuPyc II 1340 helium gas pycnometer. The pycnometer was configured to perform five purges and ten measurements during calibration and specimen analysis. The pycnometer was calibrated using a standard of known volume and the equilibrium rate was 0.0050 psig/min. Mass values were measured with an analytical balance (±0.0003 precision). For all of these measurements, the entire specimen was placed into the 10 cm^3 sample chamber—this allowed for a more representative measured density of the entire specimen.

3.4.3 Density and Porosity Measurements for High-Halide Minerals

Before firing, the green bulk density (ρ_g) was measured from the pellet weight (±0. 3 mg) and dimensions (±0.01 mm). After firing, the fired bulk density (ρ_b) was measured. Then, the specimens were broken into quadrants for characterization. Archimedes' method was used with ethanol to measure the density (ρ_a) with Equation (6) where m_{dry}, m_{sub}, and m_{sat}, are the masses (in g) of the specimen dry, submersed in ethanol, and saturated in ethanol, respectively, and the density of ethanol (ρ_e) was calculated according to Stratton (1924). Also, the open porosity (ϕ_o) was measured with Equation (7).

$$\rho_a = (m_{dry} * \rho_e) / (m_{sat} - m_{sub}) \tag{6}$$

$$\phi_o = 100 * (m_{sat} - m_{dry}) / (m_{sat} - m_{sub}) \tag{7}$$

The theoretical density, ρ_t, of the fired pellets without any porosity was calculated with Equation (8) where ρ_i is the density and m_i is the mass fraction (unitless) of the i-th component determined with X-ray diffraction (XRD). This corrects for phases of different densities when calculating the overall density. However, some error is associated with this approach considering that the ρ_i values used were provided from the crystallographic information file (CIF); the ρ_i values are calculated values and were not adjusted for compositional differences between the phases observed with XRD and those presented in the CIF. Then, the total porosity (ϕ_t) was calculated with Equation (9) where the term ''($\rho_a + \rho_b$)/2'' is the average measured density from the Archimedes (ρ_a) and bulk (ρ_b) techniques.

$$\rho_t = \sum_{i=1}^{n} p_i m_i \tag{8}$$

$$\phi_t = 100 * \left[1 - \left(\frac{\rho_a + \rho_b}{2 * \rho_t} \right) \right] \tag{9}$$

3.4.4 Storage density

Measured density was then combined with the waste loading for each specimen and the storage density, ρ_{sd}, calculated with Equation (10). Storage density (ρ_{sd}) is defined as the mass of waste per volume of waste package, where "waste package" denotes the glass with immobilized waste.

$$\rho_{sd} = \frac{\text{mass waste (kg)}}{\text{volume of waste package (m}^3)} \tag{10}$$

3.4.5 X-Ray Diffraction

Specimens of both the sodalites and glasses were analyzed with an XRD in powder form. These powders were prepared in a tungsten carbide milling chamber (minerals) or with a mortar and pestle (glasses). The XRD used for structure and phase analysis was a Bruker D8 Advanced equipped with a Cu Kα target set to a power level of 40 kV and 40 mA. The detector used was a position-sensitive detector with an angle collection range of 3° 2θ. Typical scan parameters used for specimen analysis were 5–110° 2θ for the tellurite compounds and 5–70° 2θ for the high-halide minerals with a step of 0.015° 2θ and a 0.3 second dwell at each step. JADE[TM] 6, Bruker AXS[©] EVA, and Topas 4.2 software were used to identify and quantify phase assemblages.

3.4.6 Raman Spectroscopy

Raman spectra were collected on *powdered* glasses with a SPEX 1877 Triplemate spectrometer (Horiba JY, Edison, NJ) equipped with a liquid nitrogen-cooled silicon charge-coupled device detector (Princeton Instruments, Trenton, NJ) and the 514.5 nm line of a Coherent (Santa Clara, CA) Innova 307 Ar ion laser for excitation. Data were collected in backscatter geometry with a 400 μm slit with approximately 5 mW of laser power at the specimen and a 100 s acquisition time. The estimated uncertainty of the peak frequencies was ±1 cm^{-1} for all of the Raman spectra.

Quantitative spectral analysis and curve fitting of the Raman data was performed using Thermo Fisher Scientific (Waltham, MA) Grams/32 AI software, which uses the Levenburg-Marquardt nonlinear peak

fitting method (Levenberg, 1944). Prior to curve fitting, a decaying exponential baseline correction was used to remove the background due to Rayleigh scattering. The remaining spectrum in the $300–1500$ cm^{-1} region was fitted, giving results with $R^2 \geq 0.998$.

Several protocols were considered for quantitative fitting of the Raman spectra. First, peak fitting was performed with no constraints and trends compared. This seemed to work satisfactorily with the compositional variation study glasses where a series of bands were identified and coordinated with literature values. However, for the lead-tellurite and structural variation study glasses, this method was deemed unsatisfactory, so a subsequent set of fits were performed with "fixed" wavenumber positions determined from the optimum positions for the TPb_0 glass for the main Raman bands in that glass. The frequencies, assignments, and literature references for these bands are shown in Table 3.13. The fixed frequency approach yielded R^2 fit values better than 0.999. For the purposes of analysis, ratios of peak areas were compared as a function of XCl_{20}-loading or Cl/O ratio.

For the P-series glasses, the Raman fitting was performed with no fixed parameters, and the peak frequencies of the bands were allowed to float as well as the widths as opposed to fixing the frequencies and just allowing the widths to float, as we did subsequently. As mentioned above, the latter method with fixed frequencies appeared to result in more consistent results when the $TPb_\#$ glasses were analyzed as a function of composition change. The fixed Raman frequency bands that we used for quantitative analysis of the $TPb_\#$ glasses are presented in Table 3.13 where the "**E1**/**E2**" bands were combined into "**E**" for the compositional variation study but were deconvolved into **E1** and **E2** for the rest of the glasses.

In order to determine the structural differences between the two phases present in the 15% XCl_{20}-loaded glass, both macro- and micro-Raman spectra were collected on each phase from this bulk piece. Raman spectra were obtained with the same spectrometer and laser (514.5 nm) as used in the macro measurements. However, the laser beam was coupled to a confocal Olympus BH2 microscope (Center Valley, PA) equipped with an 80× objective and numerical aperture equal to 0.75. Laser power at the specimen was approximately 10 mW. The slit width was 400 μm and the exposure time was 100 s for all specimens.

3.4.7 Chemical Durability with the Product Consistency Test (PCT)

The chemical durability test performed was the PCT, a seven-day static leaching test in deionized water at 90 °C. The PCT was performed on each of the glasses according to Test Method B (PCT-B) of the ASTM International Standard C 1285-02. The chemical durability is characterized quantitatively by the normalized sodium release (NL_{Na}, in g/m^2), being higher for less chemically durable glasses. Detailed methods and results were described in the FY2010 report (Riley et al., 2010).

For the sodalite samples, the specific surface areas of powders sieved to 75–152 μm were measured with the Brunauer-Emmett-Teller (BET) method (Brunauer et al., 1938) on $N_2(g)$ adsorption and desorption isotherms collected with an Autosorb-6B (Quantachrome Instruments, Boynton Beach, FL). The mass of specimen used was equivalent to the entire sieved fraction obtained for chemical durability tests with the product consistency test (ASTM C 1285-08, 2008). A helium pycnometer was used to measure specimen density with an AccuPyc II 1340 (Micromeritics Instrument Corporation, Norcross, GA).

3.4.8 Thermal Analysis (DTA, TGA, DSC)

The P-series lead-tellurite glasses were analyzed with a TA Instruments SDT Q600 (New Castle, DE) differential thermal-thermogravimetric analyzer (DTA-TGA). Here, specimens were run at various ramp rates (e.g., 10 °C, 15 °C) to determine the effect of ramp rate on the glass transition temperature (T_g), onset crystallization temperature (T_x), crystallization temperature (T_c), and T_M.

Differential scanning calorimetry (DSC) and TGA were performed on the powder of each glass from the lead tellurite series with a Jupiter® STA 449C (NETZSCH Instruments N.A. LLC, Burlington, MA). For the DSC/TGA experiments, specimens were loaded into alumina (Al_2O_3) pans, without lids, placed onto a

DSC/TG High RG4 sample carrier, and heated at 10 °C/min from room temperature (~25 °C) to 750 °C with air as the carrier gas at a flow rate of 50 mL/min. The spectra were analyzed with Proteus® software (v 5.3.0/24.05.2011, NETZSCH Instruments North America, LLC, Burlington, MA).

The DTA and DSC results were analyzed and the glass-formation ability (K_{gl}) was calculated according to the Hruby criterion—see Equation (11)—where T_c, T_g, and T_M are the crystallization, glass transition, and melting temperatures of the glass (Hruby, 1972).

$$K_{gl} = (T_c - T_g) / (T_M - T_g) \qquad (11)$$

Since the DSC data at temperatures above 500 °C did not appear reliable, the T_M could not be determined, accurately. Thus, we used a modified version of the Hruby criterion, presented by Wang et al., to compare the glass-formation ability with only the numerator from Equation (9), $T_c - T_g$ (Wang et al., 1994). This difference provides an estimate of how difficult it would be to quench from a melt and prevent crystallization before reaching the T_g.

Additionally, thermal diffusivity was measured for P-11 and Sodalite S5A with a NETZSCH Laser Flash Apparatus 457 (LFA). For the sodalites, powders of Sodalite 5A were pressed into a pellet, and fired at 850 °C. Then, two 12.5-mm diameter discs were core-drilled out of the pellets that were ~2-mm thick. The glass specimens for thermal diffusivity measurements were discs cut from cylinders made by pour-casting the glasses into fused silica molds at the T_M of the glass (Figure 3.3). Thus, the glasses were melted, poured into cylindrical quartz molds and annealed at 240 °C for 4 h, after which the annealing furnace was allowed to air-cool to room temperature. These cylinders were then cut into discs with a wire saw and polished to a thickness of ~2–3 mm.

The specimens were coated with Graphit® spray provided by NETZSCH, which was applied to help make sure that all of the LFA laser energy was absorbed at the front face of the specimen. Measurements for the sodalite specimens were collected at room temperature and then every 100 °C between 100 °C and 700 °C. The disc of the P-11 glass was measured at 20 °C and then in 50 °C increments from 50 to 250 °C, terminating near the T_g of the material. Five data points were collected at each temperature and averaged.
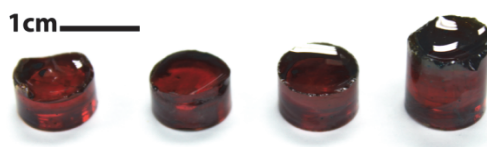
Figure 3.3. Cast cylinders of P-11 glass from which discs were cut for the thermal diffusivity measurements.

3.4.9 Scanning Electron Microscopy and Energy Dispersive Spectroscopy (SEM-EDS)

Specimens were observed in greater detail with scanning electron microscopy (SEM) and energy dispersive spectroscopy (EDS) using a JSM-5900 with a tungsten filament and a JSM-7001F with a field emission gun (JEOL, Ltd., Tokyo, Japan). For both of these systems, an EDAX Apollo II 30 mm² Si drift EDS detector (AMETEK, Berwyn, PA) was used for compositional analysis. Specimens were analyzed coated with palladium on the JSM-5900 and analyzed both coated and uncoated on the JSM-7001F. Both secondary electron (SEI) and backscattered electron (BSE) detectors were used for imaging.

3.4.10 Transmission Electron Microscopy and Energy Dispersive Spectroscopy (TEM)

Analytical transmission electron microscopy (ATEM) was performed on a JEOL 2010F field-emission gun microscope operated at 200 kV using both 20- and 50-µm diameter condenser apertures. Compositional analyses and elemental mapping were obtained with an Oxford INCA EDS (Oxford

Instruments, Concord, MA) with a fine-probe (0.7 nm diameter) in scanning TEM (STEM) mode. Powders of each glass studied were passed through a 325-μm mesh sieve, dispersed in isopropanol, and crushed in an agate mortar and pestle. Lacey carbon copper grids were then passed through the solution and allowed to dry. Regions of interest were identified at electron transparent edges of the crushed powders with a 20-μm condenser aperture so as to avoid inducing phase separation through beam damage. After analysis, regions of interest were further analyzed with the 50-μm aperture as to increase beam intensity on the specimen if allowable. Bright field (BF), selected area diffraction (SAD), and dark field (DF) imaging were used in normal TEM mode.

Table 3.13. Raman band assignments for tellurite glasses. Here, "*tbp*" denotes trigonal bipyramidal TeO_4 units, "*tp*" denotes trigonal pyramidal TeO_3 units, "NBO" denotes a non-bridging oxygen, LFE denotes the low-frequency ($\tilde{v}$) envelope, and HFE denotes the high-frequency envelope. The "Fitted" column denotes the peak locations for the fixed-frequency fitting technique that we used to fit the lead-tellurite and structural variations study glasses. The "**E1**" and "**E2**" bands were split from the "**E**" band for the lead tellurite and structural variation study glasses. The bands listed below "**E2**" are bands that were unique to a particular family of glasses and remain without a particular band name assignment due to their unique occurrences.

Band	Range ($\tilde{v}$), cm^{-1} Literature	Fitted	Group	Glasses present	Interpretation	References
A	770–780	769.7	HFE	All	Te-O$^-$ and Te=O stretch in TeO$_3$ and deformed TeO$_{3+1}$ *tp*	(Chowdari and Kumari, 1999; Mazzuca et al., 1995; Murugan et al., 2006)
B	700–760	710.9	HFE	TPb$_\#$ series, P-8 "Pb", P-11 "Pb+Cl"	Te-O$^-$ and Te=O stretch in TeO$_3$ and TeO$_{3+1}$ *tp*	(Chowdari and Kumari, 1999; Duverger et al., 1997; Mazzuca et al., 1995; Murugan et al., 2006)
C	645–670	648.0	HFE	All	Te-O asymmetric stretch in TeO$_4$ *tbp*, does not vary with type or amount of modifier; may have contribution from TeO$_{3+1}$	(Chowdari and Kumari, 1999; Murugan et al., 2006; Sekiya et al., 1992)
D	595–615	596.5	HFE	TPb$_\#$ series, P-5 "P", P-14 "P+Cl", P-8 "Pb", P-11 "Pb+Cl"	Te-O asymmetric stretch in TeO$_4$ *tbp*	(Chowdari and Kumari, 1999; Mazzuca et al., 1995; Murugan et al., 2006)
E1	400–500	432.7	LFE	All	Te-O-Te symmetric bend in vertex sharing polyhedral	(Chowdari and Kumari, 1999; Murugan et al., 2006; Sekiya et al., 1992)
E2	400–500	476.0	LFE	TPb$_\#$ series	Te-O-Te symmetric bend in vertex sharing polyhedral; Te-O-Te chains in 4-coordinated TeO$_4$ *tbp*	(Chowdari and Kumari, 1999; Murugan et al., 2006; Sekiya et al., 1992; Tatar et al., 2010)
-	355			P-9 "W", P-12 "W+Cl"	Deformation vibrations of WO$_6$	(Chowdari and Kumari, 1999; Sekiya et al., 1994a)
-	840–860			P-9 "W", P-12 "W+Cl"	Stretch of W-O associated with WO$_6$ with no W=O or asymmetric stretch of WO$_4$ having W=O	(Chowdari and Kumari, 1999; Sekiya et al., 1994a)
-	820–850			P-7 "Al/B", P-2 "Al/B+Cl"	B-O-B stretch, pyroborate; 2 NBO per B(III)	(Brow et al., 1997; Li et al., 2003)
-	925–940			P-9 "W",	Stretch of W=O or possibly W-O$^-$ located at	(Chowdari and Kumari, 1999;

Band	Range ($\tilde{v}$), cm^{-1} Literature	Fitted	Group	Glasses present	Interpretation	References
-	1040–1050			P-12 "W+Cl", P-5 "P", P-14 "P+Cl",	the edge of W clusters PO$_4$ tetrahedra with one bridging oxygen Q^1	Sekiya et al., 1994a) (Chowdari and Kumari, 1999; Murugan et al., 2006)
-	1200–1300			P-7 "Al/B"	Pyroborates [2 NBO per B(III)] or Al(IV) substituting for B(IV) in borate network	(Brow et al., 1997; Li et al., 2003)

3.4.11 Nuclear Magnetic Resonance (NMR)

Nuclear magnetic resonance was performed on select glasses for ^{23}Na, ^{125}Te, ^{207}Pb, and ^{35}Cl. Experiments for ^{23}Na were performed at 21.14 T (900 MHz for ^{1}H and 238.088 MHz for ^{23}Na) in a medium-bore (63 mm) Oxford magnet utilizing a Varian/Agilent NMR systems (VNMRS) console and an Agilent 3.2 mm MAS probe. The ^{23}Na direct polarization data were acquired utilizing a spinning speed of 15 kHz, a $\pi/20$ pulse of 0.30 μs, and a recycle delay of 1 s. The number of transients acquired varied from 964 to 9764, depending upon the amount of sodium in the specimen. Each individual time domain signal was apodized with 200 Hz of Lorentzian line broadening. Chemical shifts were referenced with respect to 0.5 M NaCl (aq) at 0 ppm.

The ^{125}Te, ^{207}Pb, and ^{35}Cl experiments were performed at 9.4 T (399.9 MHz for ^{1}H, 126.362 MHz for ^{125}Te, 83.664 MHz for ^{207}Pb, and 39.182 MHz for ^{35}Cl) in a wide-bore (89 mm) Oxford magnet utilizing a Varian/Agilent Inova console and a Doty 5 mm wideline probe. Direct polarization was utilized for the acquisition, with a $\pi/2$ pulse of 4 μs (^{125}Te), 4.5 μs (^{207}Pb), or 3.7 μs (^{35}Cl), a recycle delay of 30 s (^{35}Cl) or 120 s (^{125}Te and ^{207}Pb) with signal detection utilizing a quadrupole Carr-Purcell-Meiboom-Gill (QCPMG) echo train (Larsen et al., 1997; Larsen et al., 1999). Due to the width of the lineshapes, the entire dataset could not be acquired in a single experiment so the offset frequency was stepped every 20 kHz and then spectra from all of the offsets were combined in a sky projection to construct the final spectrum (Lipton et al.). Each individual time domain signal was apodized with a comb filter (Lipton et al.) (5 kHz for ^{125}Te and ^{207}Pb and 2.5 kHz for ^{35}Cl) matched to the echo time followed by 10 Hz (^{125}Te, ^{35}Cl) or 25 Hz (^{207}Pb) of Lorentzian line broadening. Chemical shifts were referenced with respect to 0.69 M Te(OH)$_6$ at 0 ppm (parts per million) for ^{125}Te, solid NaCl at 0 ppm for ^{35}Cl, and 0.5 M Pb(NO$_3$)$_{2(aq)}$ at -2941 ppm where Pb(CH$_3$)$_4$ is 0 ppm for ^{207}Pb, respectively.

Analysis of the complete ^{125}Te and ^{207}Pb lineshapes was accomplished with the SIMPSON software package (Bak et al., 2000) as well as other software developed at the Environmental Molecular Sciences Laboratory (EMSL, http://www.emsl.pnl.gov/emslweb/). Simulations of the NMR spectra were performed on a Beowulf cluster at the Pacific Northwest National Laboratory. The fitting procedure utilized for the experimental lineshape was a standard SIMPLEX algorithm within the SIMPSON program. Optimizations of the complete NMR lineshapes were performed with ideal radio frequency pulses, stepped offsets were not simulated in this case. We define the shielding anisotropy as $\Delta\sigma = \delta_{33} - \frac{1}{2}(\delta_{11} + \delta_{22})$, where the elements of the shielding tensor are ordered as $|\delta_{33} - \delta_{iso}| \geq |\delta_{11} - \delta_{iso}| \geq |\delta_{22} - \delta_{iso}|$. Incorporating a Gaussian disorder to the isotropic chemical shift on the order of 100 ppm mimicked the amorphous nature of the material. Simulations were calculated between $\pm 2\sigma$ (200 ppm) in 20 ppm steps and scaled appropriately before summing into the final lineshape.

4   RESULTS & DISCUSSION

4.1   Halide Mineral Processing in FY2011

4.1.1   X-Ray Diffraction

The sodalite pellets that we made in FY2010 without sintering aids showed moderate sodalite concentrations of ~ 60 mass%, mostly independent of the firing temperature (Figure 4.1). However, we were able to increase these values with some modifications to the process that included the addition of NBS-1, a glass sintering aid, and alternative Group IV component substitutions for the CS.
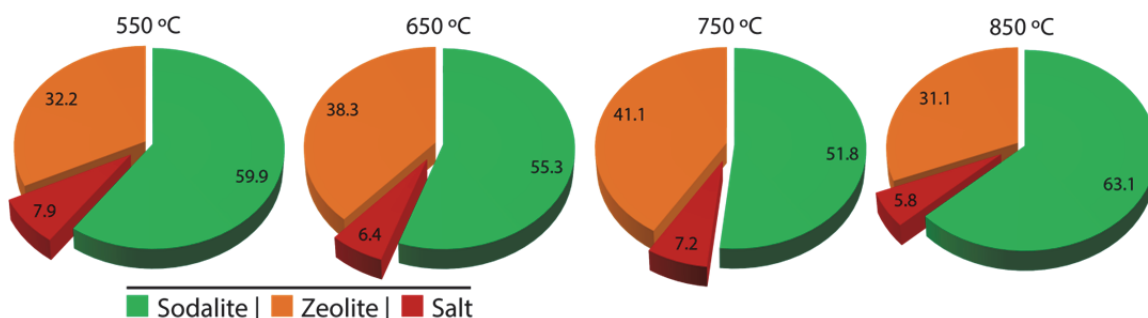
Figure 4.1. Summary of phase distribution in S5A specimens at different firing temperatures (mass %).

Figure 4.2 provides a comparison between the as-made, unfired, and dried gel of the S5A series specimens made with CS in FY2010, S5C made with TEOS in FY2011, and S5D made with Ge-EtO in FY2011. Here, it is obvious that these slight modifications to the process resulted in widely different phase distributions. The unfired S5A specimen had a very small fraction of sodalite at 24% but was increased to 76 mass% in a separate specimen that was dried at 90 °C for 5 days. The S5C specimen had a very large sodalite fraction (96%) with the S5D specimen not much lower (82%). This suggests that an organic form of the Group IV component may be the preferred precursor to achieve a large sodalite fraction in the as-made gel. Also, with the organic precursors, the fraction of unreacted salt was reduced.
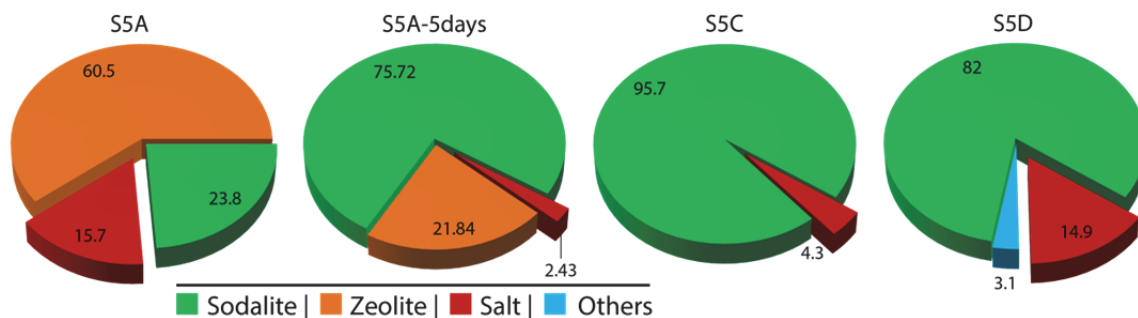
Figure 4.2. Summary of phase distribution in the S5A, S5A after drying for 5-days at 90 °C, S5C, and S5D formulations as-made (unfired) (mass %).

Figure 4.3 provides a comparison summary of the phase distribution in pellets made with different sintering aids and fired at different temperatures. All of the SA-### sintering aids behaved similarly with a maximum sodalite concentration at the lower sintering temperatures (550–600 °C) and an inverse correlation between the sodalite and Na-Al-Si-O phase concentrations with increasing firing temperatures. This is likely due to chloride volatility with increased firing temperatures. This inverse relationship was similarly observed with S5C-TePbO and S5C-NBS1 but was highly exaggerated with S5C-NaAlP.
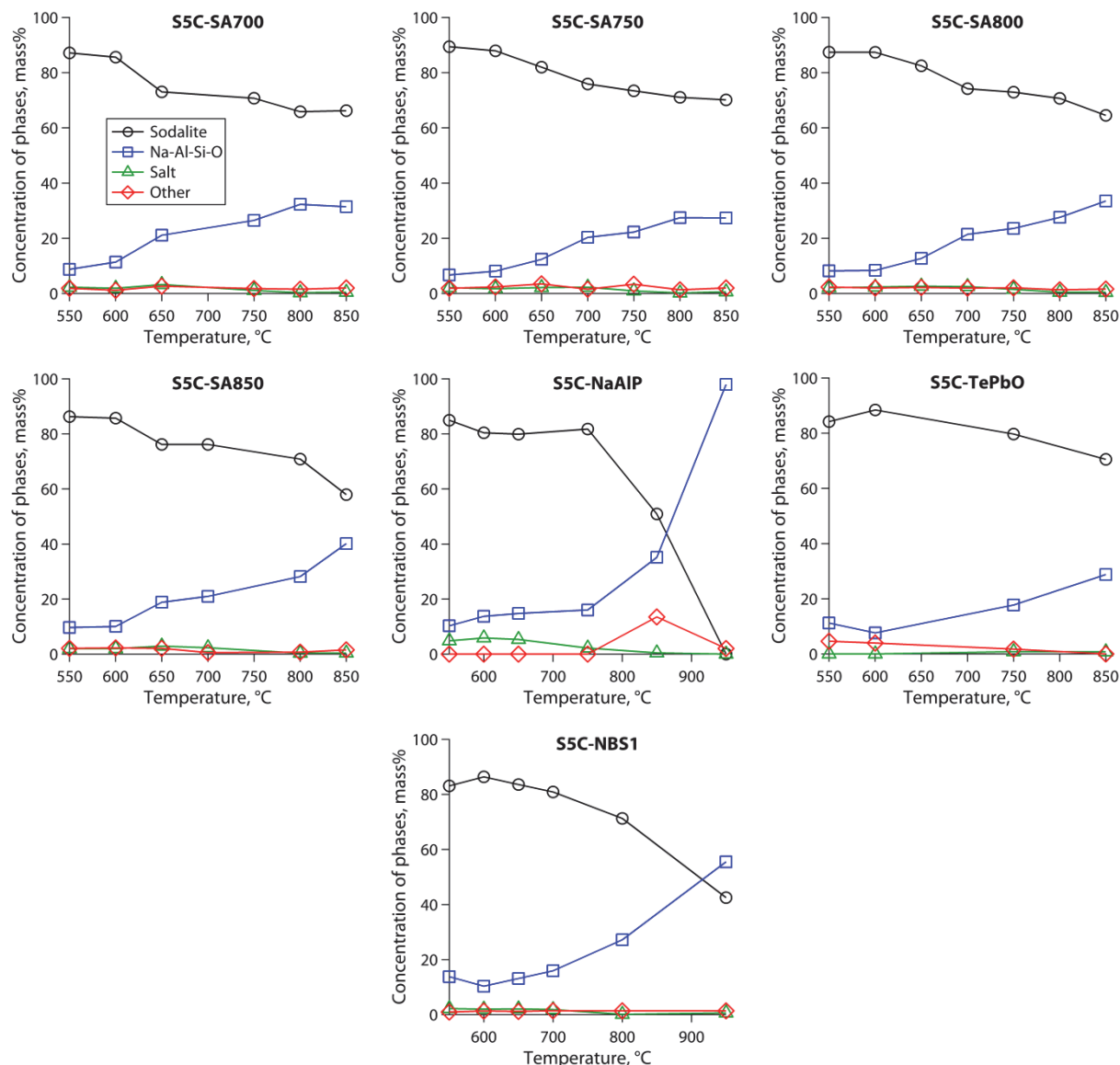
Figure 4.3. Phase distribution for the various S5C formulations at fired at different temperatures. The legend presented in the upper left figure is valid for all figure parts.

All of the crystalline phases used for the Rietveld refinement of the sodalite specimens are summarized in Table 4.1. These phases are similar to those found with the CS-based sodalites we made in FY2010, although in some cases, alternative phases were found for the sodalite and Na-Al-Si-O structural fits. More information on the exact phases found for each specimen and the actual Rietveld refinement patterns were presented in our earlier work (Riley et al., 2011).

Table 4.1. Summary of phases identified in the halide minerals. The table shows powder diffraction file (PDF) and International Crystal Structure Database (ICSD) identifications, the space group (SG), the space group number (SG#), and references for the patterns. More details can be found in our earlier work (Riley et al., 2011).

Phase ID	Category	PDF#	ICSD#	SG (SG#)	Reference
Cancrinite	Cancrinite	83-1183	80298	$P3$ (143)	(Lindner et al., 1995)
$Na_8(AlSiO_4)_6Cl_2$	Sodalite	37-0476	41188	$P\bar{4}3n$ (218)	(Beagley et al., 1982)
Hydrosodalite	Sodalite	75-5343	413502	$P\bar{4}3n$ (218)	(Kendrick and Dann, 2004)
$Na_8(AlGeO_4)_6Cl_2$	Sodalite	79-0711	65664	$P\bar{4}3n$ (218)	(Fleet, 1989)
Carnegieite low	NaAlSiO	44-1496	73511	$Pb21a$ (29)	(Withers and Thompson, 1993)
Nepheline	NaAlSiO	76-2465	37354	$P63$ (173)	(Foreman and Peacor, 1970)
$Na_{1.55}Al_{1.55}Si_{0.45}O_4$	NaAlSiO	49-0006	280473	$Pbca$ (61)	(Thompson et al., 1998a)
Analcime 1Q	NaAlSiO	73-6448	34058	$I41/ACD$ (142)	(Meier, 1973)
Sylvite (KCl)	Salt	41-1476	28938	$Fm3m$ (225)	(Barrett and Wallace, 1954)
LiCl	Salt	74-1972	27981	$Fm3m$ (225)	(Ott, 1923)
Halite (NaCl)	Salt	05-0628	28948	$Fm3m$ (225)	(Barrett and Wallace, 1954)
Li_2SiO_3	Other	83-1517	100402	Cmc (21)	(Seemann, 1956); (Hesse, 1977)
$Y_6Cl_{10}(Si_4O_{12})$	Other	70-8429	94464	$C2/m$ (12)	(Hartenbach and Schleid, 2001)

The sodalite fraction in S5D, the as-made germania-based sample, was high at 82 mass% as shown in Figure 4.4. The as-made material was pressed and fired at 750 °C and the open porosity was high (>40%) so this option was abandoned without further investigation. However, this approach of including germania-based precursors or sintering aids could be considered in the future since the results were far superior to thermal methods.
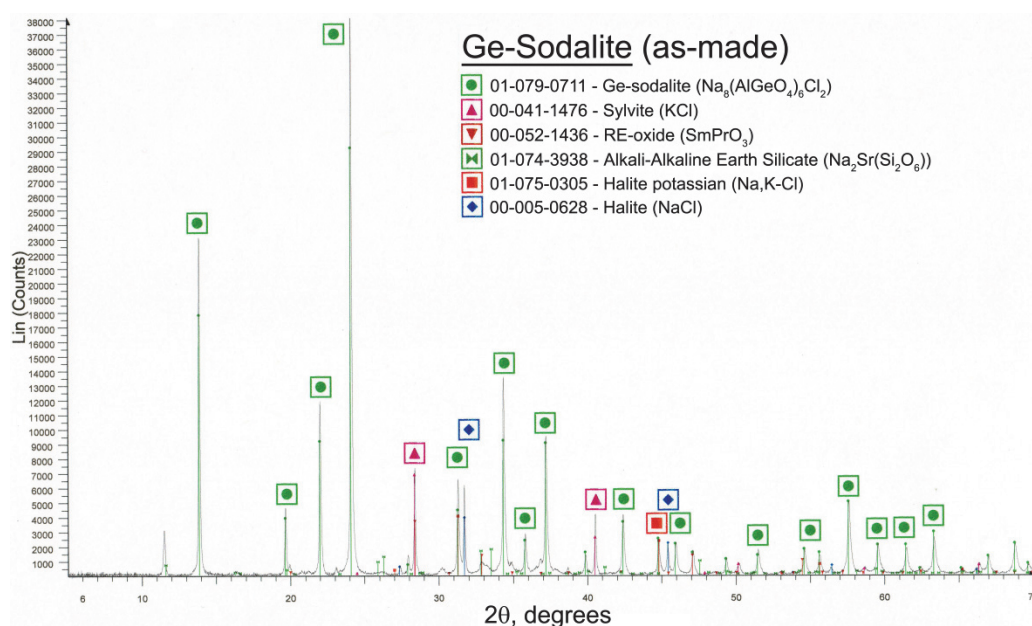
Figure 4.4. Summary of phase analysis for the as-made S5D material.

4.1.2 Pellet Densities and Porosity

The data set for the alternative sintering aids is presented in Table 4.2, with a partial graphical representation in Figure 4.5. It should be noted that the S5C-NBS1 sample is a S5C sample made in FY2011 with TEOS. Here, we see that the maximum % of ρ_t with the NBS-1 glass sintering aid was observed around 950 °C at 87%, although it had not plateaued at that point [see Equation (8)]. With the new sintering aids, densities of up to 92% of ρ_t were achieved. The optimum heat-treatment temperature to achieve maximum density was 750 °C for SA-700, SA-800, and SA-850 while it was 850 °C for SA-750 (Figure 4.5a). The NaAlP-B4 and TePbO and sintering aids did not help densify the pellets; even at 850 °C firing temperatures the densities were still < 60% of ρ_t. This suggests that these sintering aid compositions were not as reactive with the mineral components as the SA-### and NBS-1 sintering aids.

Figure 4.5b provides a comparison of the density and sodalite mass% for each sintering aid at the 750 °C firing temperature. From this plot, it is evident that the SA-### sintering aids were effective at closing the pores and allowing a good amount of sodalite to form during firing. However, at this temperature, the SA-### sintering aids are not much more efficient than the NBS-1 glass. Also, the effect of increased viscosity for NBS-1 over the SA-### sintering aids is evident by the high porosity for S5C-NBS1 at temperatures ≤ 750 °C.
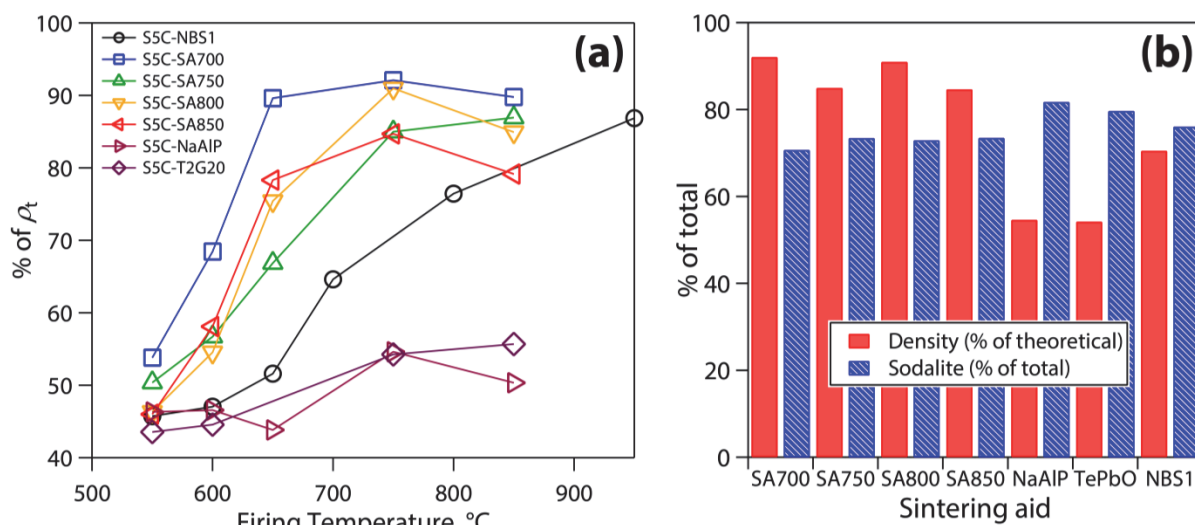
Figure 4.5. (a) Summary of % of ρ_t as a function of firing temperature for S5C series specimens made with an additional 5 mass% of various sintering aids (see Table 3.2 for more details). (b) Column chart comparing the mass% of sodalite in each specimen with the % of ρ_t for all S5C specimens fired at 750 °C.

Table 4.2. Summary of sodalite mass%, % porosity, calculated ρ_t, and % of ρ_t for specimens containing 5 mass% additions of various sintering aids and fired at different temperatures. The maxima for sodalite and % of ρ_t are shown in bold type.

Specimen ID	Firing Temperature, °C	Sodalite (mass%)	% Porosity	ρ_t	% of ρ_t
S5C-NBS1	550	83.1	56%	2.32	46%
	600	**86.4**	55%	2.32	47%
	650	83.6	51%	2.32	52%
	700	80.9	39%	2.33	65%
	800	71.3	26%	2.38	76%
	950	42.5	15%	2.43	**87%**
S5C-SA700	550	**87.2**	49%	2.32	54%
	600	85.6	34%	2.31	68%
	650	73.0	13%	2.35	90%
	750	70.7	11%	2.37	**92%**
	850	66.2	14%	2.37	90%
S5C-SA750	550	**89.4**	51%	2.31	50%
	600	87.9	45%	2.32	57%
	650	82.0	35%	2.34	67%
	700	75.9	28%	2.34	74%
	750	73.4	18%	2.38	85%
	800	71.1	20%	2.36	84%
	850	70.1	16%	2.37	**87%**
S5C-SA800	550	**87.5**	56%	2.32	46%
	600	87.4	48%	2.32	55%
	650	82.5	27%	2.33	75%
	700	74.2	15%	2.35	87%
	750	72.9	12%	2.36	**91%**
	800	70.7	15%	2.36	89%
	850	64.5	18%	2.39	85%
S5C-SA850	550	**86.3**	56%	2.32	46%
	600	85.7	44%	2.32	58%
	650	76.2	24%	2.34	78%
	700	76.2	19%	2.33	83%
	800	70.8	18%	2.36	**86%**
	850	57.9	23%	2.41	79%
S5C-TePbO	550	84.2	59%	2.33	44%
	600	**88.4**	58%	2.32	45%
	750	79.7	52%	2.27	54%
	850	70.5	51%	2.33	**56%**
S5C-NaAlP	550	**84.9**	55%	2.29	46%
	600	80.4	55%	2.30	47%
	650	79.7	58%	2.29	44%
	750	81.8	48%	2.30	**55%**
	850	50.9	50%	2.48	50%
	950	0.0	54%	2.54	50%

An effective way of comparing the data was to graph the % of ρ_t and the sodalite (mass%) on the same plot, since the goal primary goal of this work was to maximize both of these parameters. Figure 4.6 provides a comparison of density versus sodalite where the most promising candidates are in the upper right corner of the plot (S6 specimens).
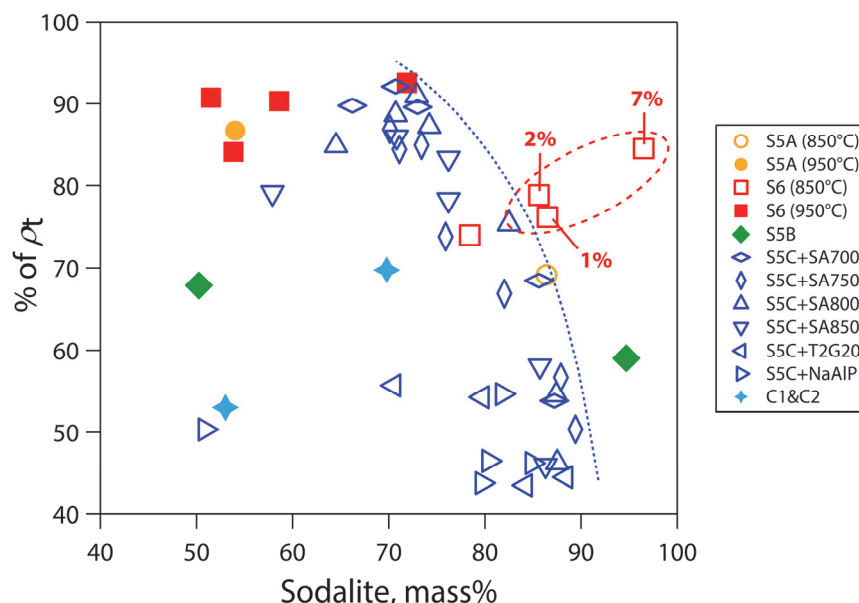
Figure 4.6.   Comparison of ρ_t and mass% sodalite for the S5A, S5B, S5C, S6, and C1/C2 series specimens (at mixed firing temperatures). The dotted blue line outlines the maxima boundary for TEOS-based pellets.

4.1.3 Scanning electron microscopy

Backscattered SEM micrographs and EDS dot mapping provided high contrast visual comparisons of the phase distribution in these specimens. A clear distinction was found between the sodalite (with chloride) and nepheline phases in the S6-7%750°C (Figure 4.7) and S5C-850°C (Figure 4.8) pellets. Figure 4.7 clearly shows the Ln separation from the bulk material as well as a distinct difference in the Si, K, and Al content between the nepheline and sodalite phases. Figure 4.8 provides some SEM comparisons between solution-based materials made with colloidal silica and TEOS as the silica source where the TEOS-based product has ~10 times smaller grain size. Additionally, Figure 4.8 shows something similar to Figure 4.7 where the nepheline and sodalite are separate phases. Also, the particle sizes of S5C-850°C are much smaller than those in S6-7%750°C. However, for the most part, S6-7%750°C (colloidal silica) and S5C-850°C (TEOS) pellets are more similar than expected based on fabrication methods and the chemical reactants used. The presence of free lanthanides is denoted by the La map.
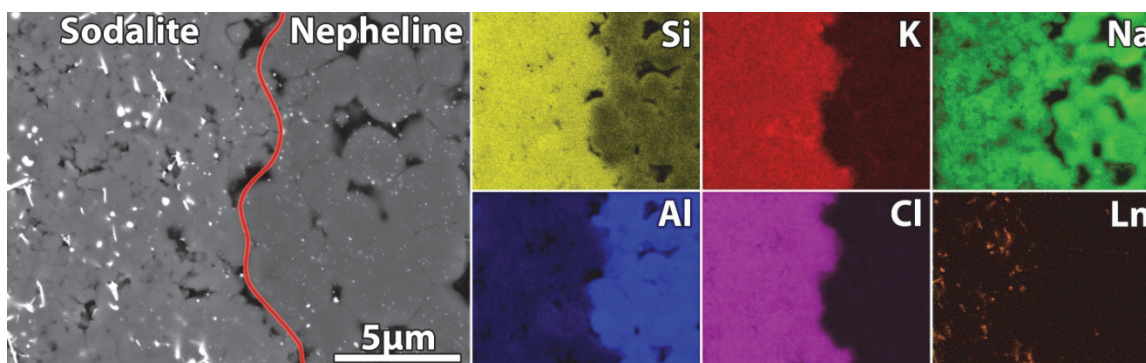
Figure 4.7. SEM micrograph and EDS dot map of S6 pellet with 7% NBS-1 glass (S6-7%750°C).
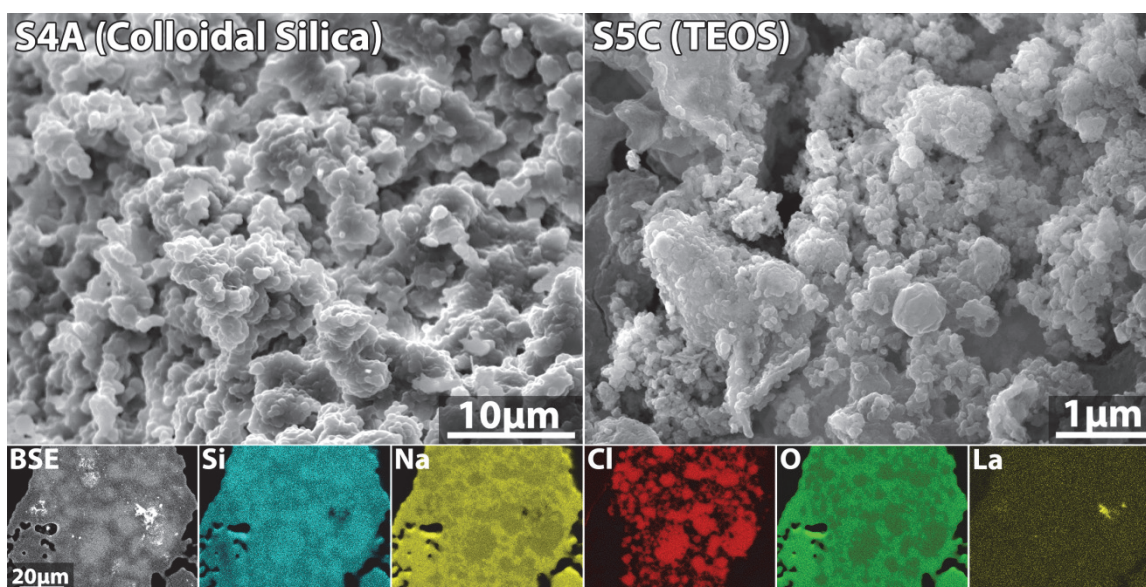
Figure 4.8. SEM micrographs of S4A, S5C, and a dot map on S5C (TEOS-based) showing elemental distribution and a clear distinction between the chloride-containing phase (sodalite), the phase without chloride (nepheline), and the lanthanide phase (shown as La).

4.1.4 Thermal Properties

The thermal diffusivity of the Sodalite 5A pellets was quantified with the NETZSCH LFA 457 using pellets (see Table 2.4 for the composition). The results from these measurements are presented in Figure 4.9. These results show that the thermal diffusivity of the S5A specimens ranged from $0.17–0.40 \times 10^{-6}$ m^2/s with a maximum value at the lower temperature and a steady decrease with increasing temperature.
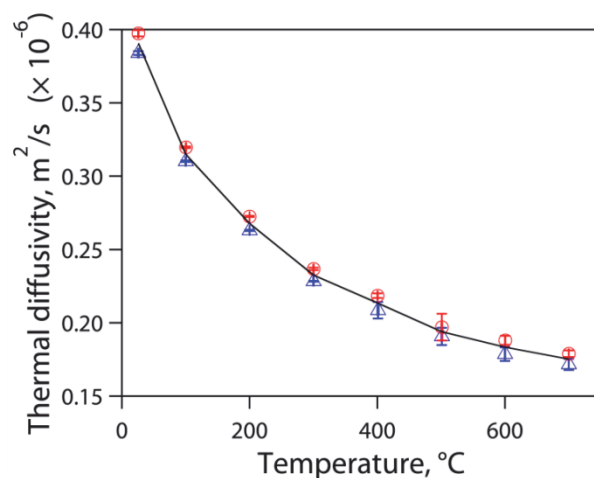
Figure 4.9. Thermal diffusivity of Sodalite 5A pellets. Error bars for the measured thermal diffusivity are included on the data points.

4.2 Halide Mineral Processing in FY2012

The pH values of the different solutions are presented in Table 4.3. The pH of the salt is slightly acidic (4.78) and the addition of the colloidal silica raises is to near-normal pH (~6.6). The addition of the NaOH or $NaAlO_2$ brings the pH to a very basic solution (~13). Even though the contents of these solutions were different, the final pH ranges were surprisingly similar (12.99–13.10).

Table 4.3. Summary of solution pH results during sample preparation. Each value is listed as an additive value where the solution contains all of the contents listed above that additive.

Solution pH after component addition	SM-1	SM-2	SM-3
Salt (XCl_{20})	4.78	4.78	–
Colloidal silica	6.60	6.56	–
NaOH + Al(OH)$_3$	12.99	–	–
$NaAlO_2$ powder + 75 mL DIW	–	13.02	–
Metakaolin + NaOH	–	–	13.14
Metakaolin + NaOH + Salt	–	–	13.10

The dried powders showed low sodalite production and some undissolved salts, even after calcination for 2–4 h at 600 °C. However, when fired at 650 °C for 8 h, some specimens showed a high sodalite fraction suggesting that the limiting factors to producing sodalite at lower temperatures might be heat-treatment time and the close contact of the powders that is achieved when they are pressed together before firing. Some of the SM-2 formulations actually showed up to 100 mass% sodalite at the 650 °C firing temperature (but with reduced densities), e.g., SM1-10%-C-650°C (92% sodalite), SM2-C-5%-650°C (100% sodalite), and SM3-AM-5%-650°C (96% sodalite). After considering all of the options, the most effective results were obtained with the sintering aid additions. For the 5% SA800 specimens, the best all-around conditions were the SM#-5%-C specimens.

A summary of all the data points collected is presented in Figure 4.10. The values used for density are an average of the measurements obtained with the two different methods and the ρ_t was calculated with Equation (8), taking into account the individual densities of all the phases present in the samples. The density of chloride-based sodalites varies by composition at 2.27–2.33×10^3 kg/m^3 (Barth, 1932b; Cressey, 2004; Frank et al., 2005; McMullan et al., 1996) and the density of the alkali aluminosilicates are elevated when compared to sodalite at ~2.54–2.67×10^3 kg/m^3, depending on the composition of the phase composition (Dollase and Thomas, 1978b; Thompson et al., 1998b). These calculations do not consider the increased density of the SA800 sintering aid (2.55×10^3 kg/m^3).

For the SM-1 specimens, 75% had a sodalite fraction exceeding 75 mass%, >50% had a sodalite fraction ≥87 mass%, and only one showed 100% sodalite (SM1-10%-C-950°C). For the SM-2 specimens, 75% had >90 mass% sodalite regardless of the processing method while 45% had 100 mass% sodalite. The SM-3 specimens produced the widest range of sodalite content of 2.8–96 mass%. These variations are attributed to the different reactivities and starting particle sizes of the precursors used in each formulation.

In general, the calcination process seemed to improve overall pellet density and sodalite production. This is likely due to the fact that calcination removes any physisorbed or chemisorbed water from the powder. If this water is not removed before the pellets are pressed, it will evolve during the firing process and result in voids within the pellet. This is supported by increased mass losses after firing the pellets for uncalcined specimens. The most satisfactory results were obtained with the calcined specimens that contained the sintering aid, e.g., SM#-5%-C. The XRD results for each specimen processed under these particular conditions at the most effective firing temperatures showed a high sodalite fraction (Figure 4.11). Minor phases found for SM3-5%-C-750°C were $KAlO_2$ (Sokolowski and Kotarba, 2000) and $K_{1.6}Na_6Al_{7.49}Si_{8.51}O_{32}$ (nepheline) (Tait et al., 2003a); NaCl was also found in SM-1 (not shown).
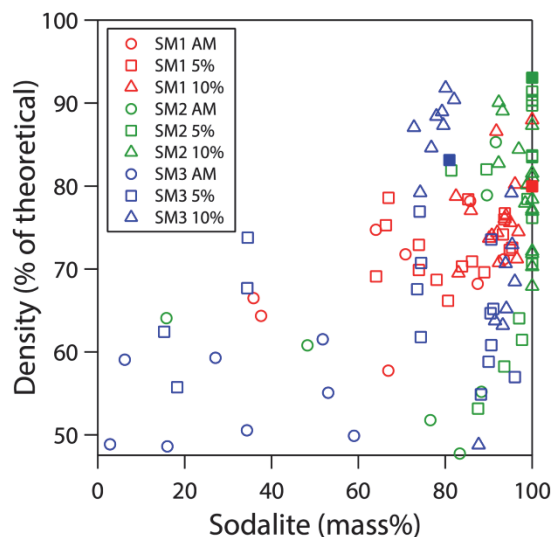
Figure 4.10. Summary of density (% of theoretical) as a function of sodalite concentration (mass%) for all data. The filled squares are the PVS specimens with 5% SA800 that were isostatically pressed at 3.4×10^8 Pa (5.0×10^4 PSI).
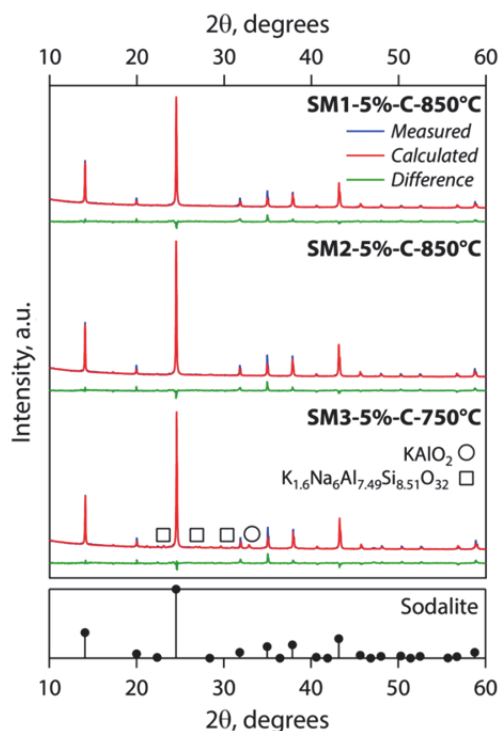
Figure 4.11. XRD summary figure showing sodalite (space group = $P\bar{4}3n$) as the primary phase for these three specimens SM1-5%-C-850°C, SM2-5%-C-850°C, and SM3-5%-C-750°C with a unit cell of a = 0.882 nm, 0.889 nm, and 0.887 nm, respectively (Barth, 1932a). The minor phases were $KAlO_2$ (Sokolowski and Kotarba, 2000) and $K_{1.6}Na_6Al_{7.49}Si_{8.51}O_{32}$ (nepheline) (Tait et al., 2003a) for SM3-5%-C-750°C. This plot shows the raw measured data (blue), fitted/calculated spectra (red), and difference patterns (green) for each spectra.

4.2.1 SM-1 (Gibbsite) Overview

Without a sintering aid, the SM-1 pellets with the lowest porosity were found at the lower firing temperatures. The mass% of sodalite in the SM1-AM-850°C and SM1-AM-C-850°C specimens were high at 94% and 88% but with reduced densities at 71% and 68% of ρ_t, respectively. When 5 or 10 mass% SA800 was added, firing at 950 °C produced the highest densities (74–88% of ρ_t). The addition of 10 mass% SA800 improved all SM-1 specimens with noticeably higher sodalite fractions and densities. The best specimen for the SM-1 method was SM1-10%-C at 950 °C at 100 mass% sodalite and 88% of ρ_t. For these pellets, higher firing temperatures such as 850–950 °C and 5–10 mass% of this sintering aid would be required to achieve high sodalite and low porosity in pellets made with this synthesis method.

4.2.2 SM-2 (NaAlO$_2$) Overview

The SM-2 formulations proved the most effective at forming sodalite and were a noticeable improvement over our previous work with increased densification at lower temperatures and very high sodalite fractions. This is likely because this method provided the most effective mixing of the precursors; the NaAlO$_2$ was completely dissolved in solution when it was added to the mixture during the synthesis process.

Without a sintering aid, the SM-2 specimens showed the highest sodalite at the 750 °C firing temperature (SM2-AM-750°C, 83%), although the density was very low at 48% of ρ_t. The SM2-AM-C specimens showed a consistent increase in sodalite between 750 and 950 °C at 88–92 mass% with a steady increase in density from 55% to 85% of ρ_t, respectively. With the addition of 5 mass% SA800, specimens fired at 850 °C showed the highest sodalite fractions.

The best specimen for the SM-2 formulation was SM2-5%-C-850°C at 100% sodalite and 91% of ρ_t. Further analysis of this specimen with SEM-EDS showed that two distinct compositions were present (Figure 4.12). Cluster phase analysis on this map with the Genesis software showed two distinctly different sodalite phases with similar, yet not identical compositions. The Na:K ratios were identified (80.8:1 for red and 33.6:1 for blue) while analyses on the rest of the components were shown to be congruent (Figure 4.13). This indicates that the chemical segregation identified could have a few different causes including: (1) a difference in Li content between these phases (cannot measure with EDS) causing a difference in contrast with SEM, (2) a solid-solution of sodalite with varying chemistries does not form in this system where phases with differing chemistries form and do not mix, or perhaps (3) an unknown heterogeneous interaction with the glass binder results in compositional variation in the sodalite.

For specimens with 10 mass% SA800 fired at 650 °C, the highest density was observed for SM2-AM-10%-650°C (84% of ρ_t) and this specimen had high sodalite at 97 mass%. The highest densities for most were observed at the 750 C firing temperature at 83–90% of ρ_t and the fractions of sodalite in these pellets were high (92–100 mass%). Both the 850 and 950 °C firing temperatures worked equally well for sodalite production where all specimens had 100 mass% sodalite. However, it remains unclear why the densities of these pellets are all low (68–84% of ρ_t).
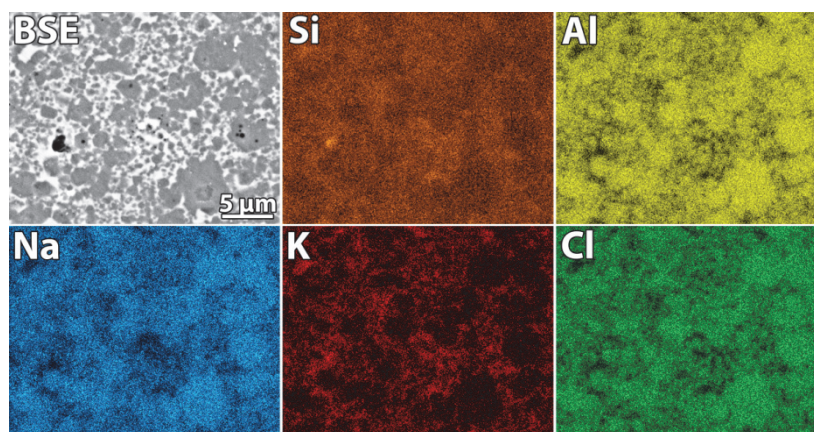
Figure 4.12. SEM-EDS dot map on SM2-5-C-850°C showing compositional variations in the sodalite.
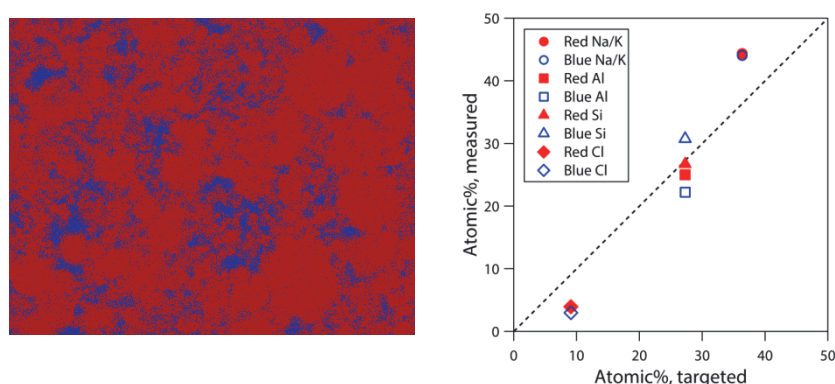
Figure 4.13. (left) Cluster phase analysis of the dot map seen in Figure 4.12 and (right) a comparison of the measured normalized compositions for the red and blue phase compared to the target values based on the target sodalite composition (oxygen is normalized out).

4.2.3 SM-3 (Metakaolin) Overview

The sodalite production in the SM3-AM and SM3-AM-C specimens was very low (3–59%). However, even with only 5 mass% SA800, the sodalite production was increased by up to 72% in comparable formulations, e.g., SM3-5%-650°C (88%) vs. SM3-AM-650°C (16%). All SM-3 formulations with the sintering aid showed unexpected highs for sodalite at the 650 and 750 °C firing temperatures, with most maxima at 750 °C. One of the more anomalous data points was SM3-AM-5% with 96 mass% sodalite at 650 °C.

All specimens with 5 mass% SA800 showed the same trend where the sodalite fraction decreased consistently between the 750–950 °C firing temperatures with very low sodalite fractions at the 950 °C firing temperatures (15–35%); this was attributed to chloride volatility during firing. All of the sodalite fractions in the specimens with 10 mass% SA800 were moderate to high (73–96%). Even small quantities of sintering aid dramatically improved the sodalite production for SM-3 formulations.

The densities of specimens without sintering aids (SM3-AM and SM3-AM-C) were 52–69% of ρ_t where the calcined specimens had a universally higher density than uncalcined specimens (10–22%). On average, specimens with 5 mass% SA800 showed a noticeable improvement in density from those without the sintering aid (10%) and the specimens with 10 mass% SA800 showed a significant increase in density (23%).

For specimens with 5 mass% SA800, those fired at 850 and 950 °C generally had the highest densities and for specimens with 10 mass% SA800, the highest densities were achieved at the 950 °C firing

temperature in all cases. For SM-3 specimens, an inverse relationship was observed between sodalite production and density at increased firing temperatures where low firing temperatures (650–750 °C) produced pellets with high sodalite and high open porosity whereas high firing temperatures (850–950 °C) produced pellets with low sodalite and low open porosity.

4.2.4 Comparisons

The as-made specimens looked very similar with SEM (Figure 4.14). The particle sizes appeared to be somewhat consistent between samples with a mixture of both smaller and larger grains.
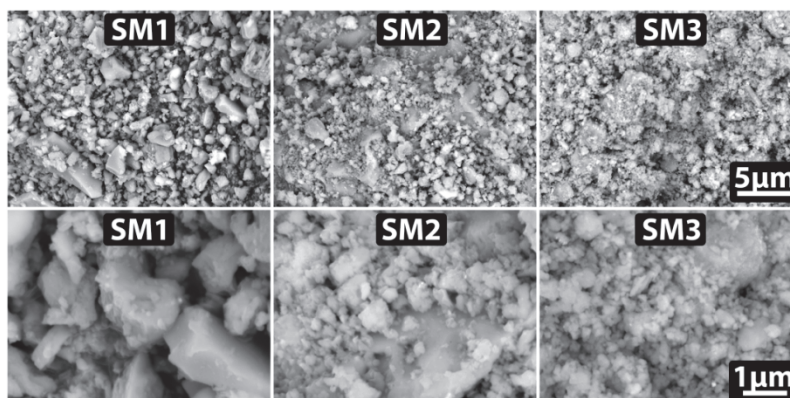
Figure 4.14. SEM micrographs showing a particle size comparison between the as-made powders for SM-1, SM-2, and SM-3 formulations.

Due to the large number of specimens generated during this study, the results were divided and compared in Figure 4.15–Figure **4.19**. Figure 4.15 shows the differences in sodalite and density by both method and firing temperature and provides an overview of the variability seen between the three synthesis methods. For the SM1 and SM3 specimens, the highest densities were achieved at the 10 mass% loading of the sintering aid, while the sintering aid additions proved less important for maximizing the density of SM2 specimens.
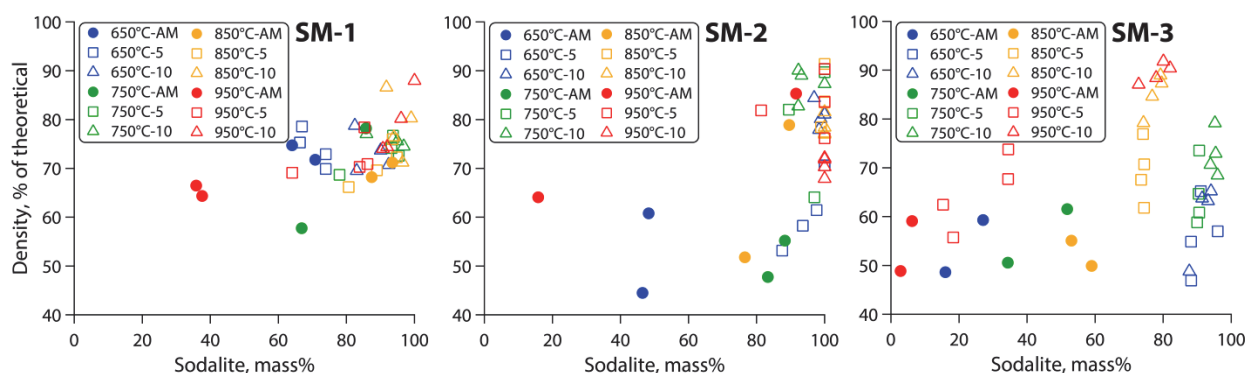
Figure 4.15. Comparison plots for density (% of theoretical density) and the mass% sodalite of specimens sorted by method and heat-treatment temperature.

Figure 4.16 provides several comparisons between specimens of similar, but slightly different, preparations. For example, when considering the SM#-5 and SM#-AM-5 specimens (*Comp. 1*), where the only distinction between the two data sets is the time in the procedure at which the sintering aid is added (during the process or after drying, respectively), the sodalite fraction slightly improved when the sintering aid was added after drying. However, an overwhelming improvement to the density was observed when the sintering aid was added after drying. *Comp. 2* provides a comparison for specimens

where the timing of the calcination step varied and specimens were either calcined before (SM#-C-5) or after (SM#-5-C) the addition of the sintering aid. *Comp. 2* shows that the sodalite fraction does not change much between these two different preparations but that the density varies widely. *Comp. 3* and *Comp. 4* are the same comparisons as *Comp. 1* and *Comp. 2* but with 10% sintering aid instead of 5% (by mass). *Comp. 3* shows slightly the opposite trend as *Comp. 1* where the sodalite fraction was higher in the SM#-10 specimens versus the SM#-AM-10 specimens. A similar trend was observed in *Comp. 3* for the density. *Comp. 4* shows that the sodalite fractions and densities are slightly higher for the SM#-10-C specimens over the SM#-C-10 specimens.
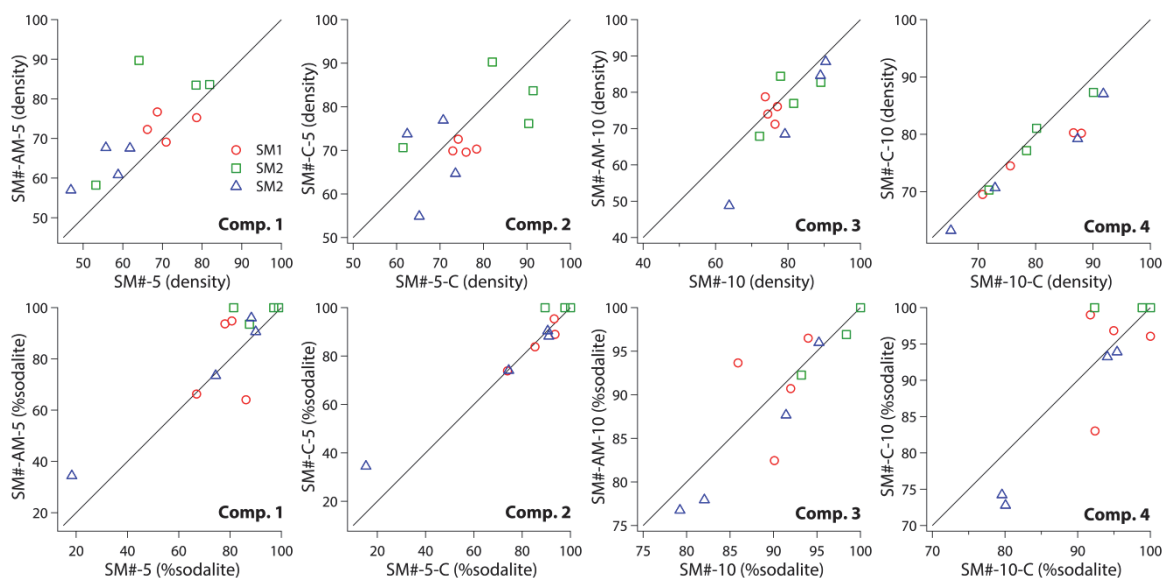
Figure 4.16. Comparison plots between like procedures for the density (% of theoretical maximum for sodalite) and the mass% sodalite of pellets fired at all temperatures for specimens with 5 and 10 mass% additions of sintering aid (SA800).

Figure 4.17–Figure 4.19 provide comparisons between the calcined and uncalcined specimens. Figure **4.17** shows that all calcined specimens exhibited a significantly lower mass loss during firing than uncalcined specimens (up to 46× for SM1-C-950°C vs. SM1-950°C). In some cases, more mass loss was observed than would be expected, especially with most of the data points for the SM3 specimens where up to 17.2% mass loss was observed in calcined pellets (SM3-C-950°C).

Figure 4.18 shows the difference in density and sodalite between the as-made (SM#-AM) and as-made and calcined (SM#-AM-C) specimens. From this comparison it is easy to see that calcination improved both the density and sodalite fractions with minor exceptions. Figure 4.19 shows that calcination provides a marked increase in both sodalite and density, with a few exceptions. These results show the importance in calcination and are attributed to the release of bound hydrates from the sodalite structure during the calcination process. By allowing these hydrates to evolve from the sodalite prior to firing the pellets in pressed form, this should result in fewer voids than if the hydrates were allowed to evolve from pressed pellets.
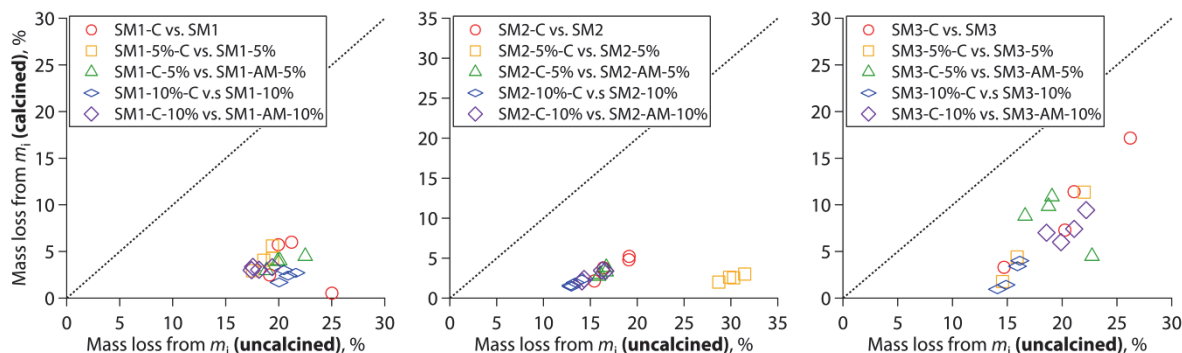
Figure 4.17. Comparison of mass loss during firing for calcined versus uncalcined specimens. Here, mass loss is determined by $100 \cdot (m_i - m_f)/m_i$ (to get %) where m_i is the initial mass and m_f is the final mass as measured on an analytical balance. Dotted lines are a guide for unity.
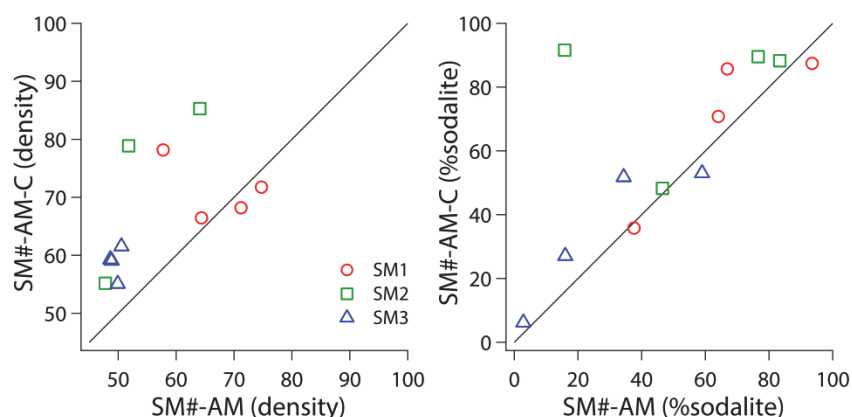
Figure 4.18. Comparison plots between like procedures for the density (% of theoretical maximum for sodalite) and the mass% sodalite of as-made pellets without sintering aids fired at all temperatures (i.e., SM#-AM and SM#-AM-C). The 45° lines are a guide for unity.
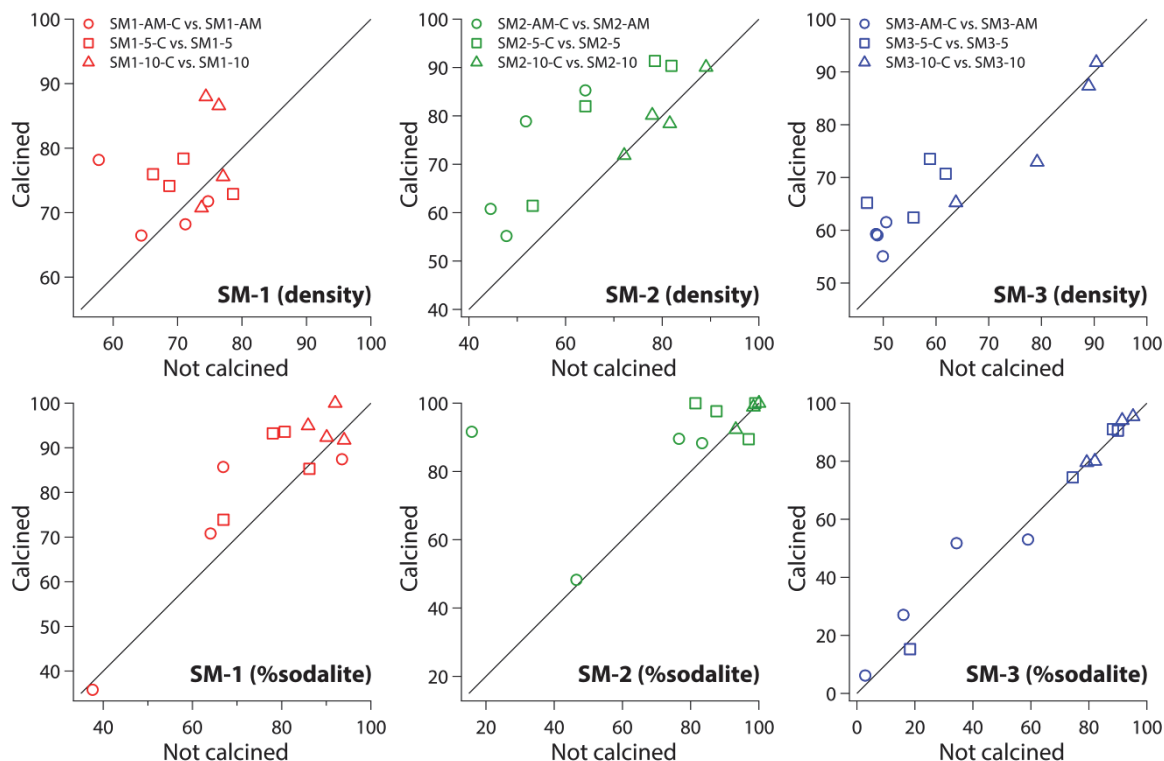
Figure 4.19. Comparison plots for the density (% of theoretical density) and the mass% sodalite of specimens that were and were not calcined prior to being pressed into pellets (for all temperatures). Legends in the top row of figures are the same for the bottom row.

The results from the pressure variation study show that the pressure at which pellets were pressed had a slight effect on the SM-1 and SM-2 pellets but proved to be important for SM-3 pellets as seen in Figure 4.20 and Figure 4.21. For SM-2 and SM-3 pellets, the pellet density increased with pressure but with the SM-1 pellets, the trend was nearly decreasing. The sodalite fractions in all SM-1 and SM-2 pellets were 100% whereas the trend showed an increase for SM-3 pellets. These data show that high density and high sodalite pellets can be produced with the SM-2 method by simply pressing the SM2-5%-C pellets uniaxially at moderate pressures. This result was not expected. Also, the data spread for all densities is low as with the sodalite fraction for SM-1 and SM-2 pellets, but not for sodalite for SM-3 pellets. Since these pellets are all pressed from the same batch that was homogenized prior to pressing pellets, this suggests heterogeneities in the SM-3 pellets.
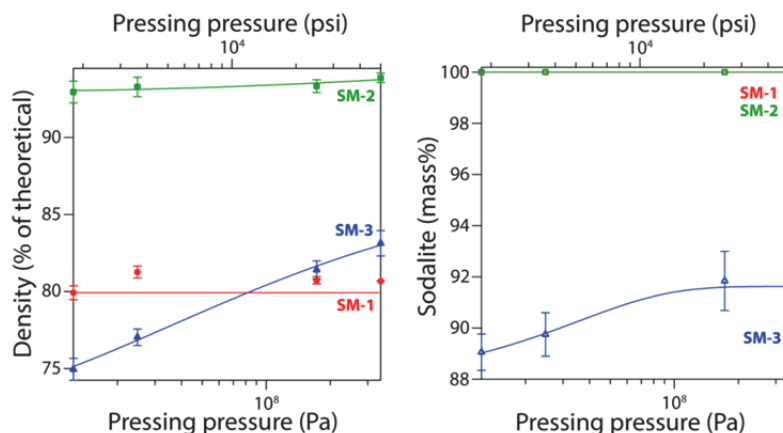
Figure 4.20.   Comparisons from the pressure variation study showing the density and sodalite as a function of pressing pressure.
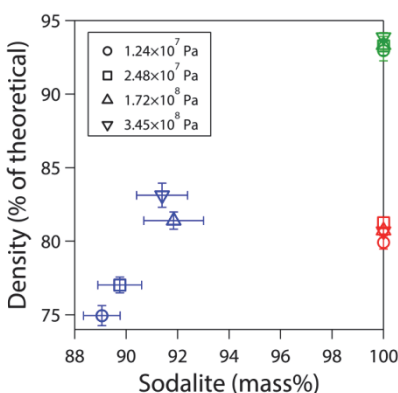
Figure 4.21. Density versus sodalite for the PVS samples. SM-1, SM-2, and SM-3 specimens are in red, green, and blue, respectively.

4.2.5 Spark Plasma Sintering Results

It is likely that hot isostatic pressing would further increase pellet densities from those seen in the pellet tests discussed above but that was not evaluated in the current work. Spark plasma sintering was evaluated but proved to be unsuccessful because the temperatures of the experiments (526–554 °C) were not sufficient to convert the calcined product into pellets with high sodalite fractions. In the regularly fired specimens, the maximum sodalite fractions were observed in specimens fired at or above 750 °C. The main limitation with this technique is that a dynamic force is applied during heating and if the heat-treatment temperature is taken too high, the specimen could melt and be extruded from the die. We plan to further evaluate this technique with the TEOS-based sodalites that showed high sodalite fractions in the as-made, unfired products.

Figure 4.22 shows the temperature and die displacement as a function of time for each specimen. The values of displacement vary widely between specimens where the smallest displacement observed was in the SM-2 specimen which supports the data in Table 4.4 where this specimen showed the lowest increase in density between the fired and unfired measurements. The density of the fired SM-1 pellet was slightly higher than the calculated ρ_t, suggesting no open porosity (Table 4.4), which is attributed to the large fraction of nepheline that has a higher density than sodalite at 2.5445×10^3 kg/m^3 (Table 4.5) (Dollase and Thomas, 1978a). This large fraction of nepheline is likely due to the loss of chloride during heating.

It is possible that all of these have a fraction of unreacted, amorphous content as well since they were not doped with a standard prior to XRD. This is evidenced by the large fraction of unreacted salts in the SM-1 and SM-2 pellets. Surprisingly, the phase distributions in the fired pellets varied widely with the SM-3 pellet showing the highest sodalite fraction (96%) without any unreacted salts whereas the SM-1 pellet only had 28% sodalite; SM-2 was in between with 79% sodalite. It should be noted that the NaCl fractions reported for SM-1 and SM-2 are much higher than the amount of NaCl added to the batch and when considering that some sodalite formed in both cases, the true value of unreacted salt is actually much lower. The cause of this anomaly is currently not understood.
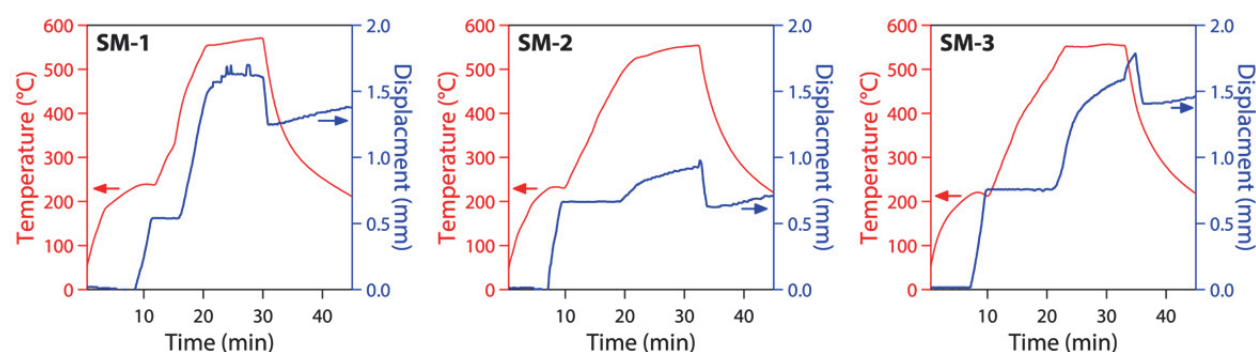
Figure 4.22. Spark plasma sintering results. These show the displacement and temperature as a function of time for each pellet.

Table 4.4. Density measurements for the specimens that were heated with spark plasma sintering. The data in parenthesis shows the percent of theoretical density for sodalite (2.27×10^3 kg/m^3).

Pellet	Green Density, $\times 10^3$ kg/m^3 (Bulk)	Fired Density, $\times 10^3$ kg/m^3 (Archimedes)	Fired Density, $\times 10^3$ kg/m^3 (Bulk)	Increase in Fired Density over Green Density
SM-1	1.70 (75%)	2.49 (102%)	2.49 (102%)	46.5%
SM-2	1.49 (66%)	1.75 (77%)	1.73 (76%)	16.9%
SM-3	1.34 (59%)	1.82 (79%)	1.77 (77%)	34.0%

Table 4.5. Phase distribution from XRD measurements.

Pellet	Phase distribution (mass%)
SM-1	51.35% nepheline, 28.01% sodalite, 20.64% NaCl
SM-2	78.78% sodalite, 15.70% NaCl, 5.49% nepheline
SM-3	95.97% sodalite, 4.03% KAlO$_2$

4.2.6 Chemical Durability Tests

The specimens chosen for the PCT were SM1-5%-C-850°C, SM2-5%-C-850°C, and SM3-5%-C-750°C. The ρ_b, % of ρ_t, and phase distribution of these specimens are listed in Table 4.6. The normalized release rates (NL_is) for the PCT leachates are summarized in Table 4.7. The release for a given element was consistent in some cases (Al, Na, Si) but was inconsistent for others (B, Cl, K, Li, and lanthanides). Some of these discrepancies are due to the non-sodalite phases present in the as-fired specimens (see Table 4.6). For example, the Cl-release was highest for SM-1 but that specimen had some free NaCl.

Table 4.6. Summary of characterizations for PCT specimens prior to the PCT.

Specimen	ρ_b ($\times 10^3$ kg/m^3)	ρ_t (%)	Phase distribution (mass%)			
			Sodalite (Tamazyan et al., 1988)	NaCl (Srinivasa and Sanyal, 1990)	Neph.* (Tait et al., 2003b)	KAlO$_2$ (Sokolowski and Kotarba, 1998)
SM1-5%-C-850°C	1.83	75.98	93.60	6.40	-	-
SM2-5%-C-850°C	2.06	91.39	100.00	-	-	-
SM3-5%-C-750°C	1.86	73.54	90.58	-	5.05	4.37

*"Neph." is off-stoichiometric nepheline with composition $K_{1.6}Na_6Al_{7.49}Si_{8.51}O_{32}$

Table 4.7. Averaged NL_i (g/m^2) in leachates from PCT-B with standard deviations listed in parenthesis. *Ln denotes total lanthanides analyzed and includes Ce, La, Nd, Pr, and Sm. Note that the release values for Ba were below detection limits for SM-1 and SM-2.

Element	SM-1	SM-2	SM-3
Al	0.0906 (0.0006)	0.0821 (0.0043)	0.0918 (0.0023)
B	0.248 (0.004)	0.345 (0.024)	7.47 (0.49)
Ba	- -	- -	0.050 (0.003)
Cl	0.158 (0.002)	0.0562 (0.0024)	0.0681 (0.0033)
K	0.300 (0.006)	0.581 (0.027)	2.15 (0.14)
Li	0.583 (0.007)	1.53 (0.11)	8.26 (0.62)
Ln*	0.0244 (0.0016)	0.355 (0.035)	0.0398 (0.0008)
Na	0.182 (0.002)	0.201 (0.013)	0.162 (0.010)
Si	0.0675 (0.0008)	0.134 (0.002)	0.0842 (0.0018)

Each of these synthesis routes has advantages and disadvantages from a chemical durability standpoint. First, although SM2-5%-C-850°C showed high density and sodalite, some NL_is were higher for this specimen than for SM1-5%-C-850°C including: lanthanides (14×), Li (1.6×), Si (0.99×), K (0.93×), B (0.39×), and Na (0.10×). Some NL_is were noticeably higher for SM3-5%-C-750°C than SM2-5%-C-850°C including B (22×), Li (4.4×), and K (2.7×). This higher leaching with SM3-5%-C-750°C is thought to be due to ineffective mixing of the metakaolin during the synthesis process. Additionally, the incongruent release of the elements from the sintering aid component could be due to selective leaching of this phase around the sodalite grain boundaries. This selective leaching could likely be reduced by adding an equally low-viscosity sintering aid with higher chemical durability.

The summary NL_i values for the rinsates are presented in Table 4.8. These results show that some soluble species were removed during the rinsing step. The specific surface areas measured with BET for SM1-5%-C-850°C, SM2-5%-C-850°C, and SM3-5%-C-750°C were 79, 9, and 104 m^2/g, which equates to 33.2×, 3.8×, and 45.9× the assumed values based on the procedure (ASTM C 1285-08, 2008), respectively. The NL_is adjusted for these measured specific surface areas are presented in Table 4.9; due

to the low porosity measured with BET for SM2-5%-C-850°C, the adjusted NL_is are higher than for SM1-5%-C-850°C and SM3-5%-C-750°C.

Table 4.8. Summary NL_i (m^2/g) values of rinsate analysis.

Element	SM-1	SM-2	SM-3
Al	1.02	0.856	2.77
B	0.798	0.450	3.06
Cl	1.70	0.549	0.138
K	1.38	0.984	3.20
Li	1.20	1.09	5.18
Ln	0.809	0.710	1.03
Na	1.53	1.19	2.71
Si	0.975	0.879	2.42

Table 4.9. NL_i values ($\times 10^{-3}$ g/m^2) adjusted for measured specific surface areas (standard deviations are below the average values).

Element	SM1	SM2	SM3
Al	2.733	21.77	1.998
	(0.019)	(1.15)	(0.049)
B	7.490	91.43	162.5
	(0.120)	(6.37)	(10.8)
Cl	4.776	14.92	1.481
	(0.056)	(0.65)	(0.071)
K	9.061	154.0	46.81
	(0.192)	(7.1)	(2.95)
Li	17.60	406.8	179.8
	(0.21)	(27.9)	(13.5)
Ln	17.60	406.8	179.8
	(0.21)	(27.9)	(13.5)
Na	5.489	53.19	3.523
	(0.061)	(3.30)	(0.207)
Si	2.036	35.45	1.833
	(0.025)	(0.63)	(0.039)

4.3 Tellurite Glasses

4.3.1 Tellurite Glasses: Compositional Variation Study

4.3.1.1 X-Ray Diffraction

To reiterate from the FY2010 report, before the PCT, all ten "P-series" tellurite glasses were determined by XRD to be bulk amorphous; in other words, if crystals were present in some of the glasses it was

below the detection limit of the instrument (Riley et al., 2010). Figure 4.23 provides fitted backgrounds for the amorphous pre-PCT XRD spectra, which help reveal the subtle differences in peak location and intensity. The PbO glasses had the tallest and narrowest amorphous humps, suggesting that they were the most "structured" of this glass set.

Simulated amorphous diffraction patterns were generated for the different α-TeO$_2$ and β-TeO$_2$ PDF patterns in the ICSD that matched diffraction peaks for the various glasses with Jade 6 software with a set crystallite size of 10 nm and 0% strain (see Table 4.10). The three simulated patterns differed in amorphous hump location and intensity as seen in the bottom portion of Figure 4.23. When observing Figure 4.23 (primarily the low-2θ hump) with the vertical guides as a reference, it is apparent that some of the glasses seem to fit the simulated orthorhombic β-TeO$_2$ phase (PDF# 74-1131, Table 4.10), such as the Al$_2$O$_3$/B$_2$O$_3$-containing glasses (P-7 "Al/B" and P-2 "Al/B+Cl"), while the other glasses seemed to fit with the tetragonal α-TeO$_2$ phases (PDF#s 42-1365 and 78-1713, Table 4.10).

A summary of the XRD results for the ten glasses after the PCT is shown in Figure 4.23b with the best-fit structures presented in Table 4.10. Diffraction peaks matching Pb$_2$Te$_3$O$_7$ crystals were observed in P-8 "Pb" and P-11 "Pb+Cl" glasses after the PCT, although quantities were close to the detection limit for P-11. For the tungstate glasses, only P-12 "W+Cl" crystallized (to Ba$_3$WO$_6$) after the PCT. The other three families, the Al$_2$O$_3$/B$_2$O$_3$ (P-7 and P-2), ZnO (P-4 and P-13)-, and P$_2$O$_5$ (P-14 and P-5)-containing glasses all had characteristically different behavior with and without added XCl$_{20}$. Without XCl$_{20}$, all formed some α-TeO$_2$ (tetragonal paratellurite), while the Zn glass (P-4) also formed some Zn$_2$Te$_3$O$_8$. After adding XCl$_{20}$, all formed some β-TeO$_2$ (orthorhombic tellurite), while Al/B+Cl (P-2) also formed Na$_2$Te$_2$O$_7$, and Zn+Cl (P-13) formed Zn$_2$Te$_3$O$_8$.

It should be noted that of the glasses that showed crystalline TeO$_2$ phases after the PCT (i.e., P-7 "Al/B," P-2 "Al/B+Cl", P-5 "P", P-14 "P+Cl", P-4 "Zn", and P-13 "Zn+Cl"), those containing XCl$_{20}$ always formed β-TeO$_2$, whereas those without XCl$_{20}$ were shown to form α-TeO$_2$. This demonstrates that mixed-chloride additions to the tellurite glass network have a consistent effect on the network structure. In these systems, it appears that XCl$_{20}$ additions, or perhaps the alkali and lanthanide elements in the presence of chlorine, favor the formation of β-TeO$_2$ structures.
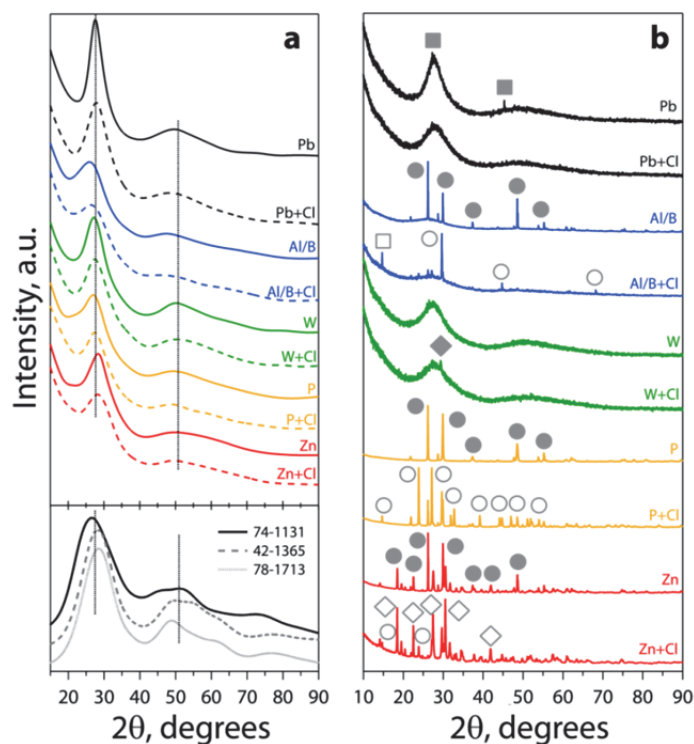
Figure 4.23. (a) XRD summary plot showing the amorphous background fits for all glasses before PCT for comparison with three amorphous simulated patterns for TeO_2 PDF structures (74-1131, 42-1365, and 78-1713; see Table 4.10). Vertical lines are added as a visual guide for the location of the primary amorphous humps. The spectra are vertically offset (intensities retained) to accentuate the differences so the vertical scale is listed in arbitrary units (a.u.). (b) XRD spectra for all 10 glasses after PCT. Best-fit diffraction peaks were identified and are denoted by symbols near the most intense of the diffraction peaks for each phase observed for each glass.   Here, ● denotes tetragonal α-TeO_2, ○ denotes orthorhombic β-TeO_2, ■ denotes $Pb_2Te_3O_7$, □ denotes $Na_2Te_2O_7$, ◆ denotes Ba_3WO_6, and ◇ denotes $Zn_2Te_3O_8$. This figure was recreated from our previous work (Riley et al., 2010).

Table 4.10. Summary of phases identified in the tellurite glasses for the composition-variation study.

Phase ID	PDF#	ICSD#	SG (SG#)	Reference	Glasses
α-TeO$_2$	78-1713	62897	$P4_32_12$ (96)	(Kondratyuk et al., 1987)	P-4 "Zn", P-7 "Al/B"
α-TeO$_2$	42-1365	27515	$P4_12_12$ (92)	[a]	P-5 "P (phosphorus)"
β-TeO$_2$	74-1131	26844	$Pbca$ (61)	(Beyer, 1967)	P-2 "Al/B+Cl", P-14 "P+Cl", P-13 "Zn+Cl"
Pb$_2$Te$_3$O$_7$	43-0549	N/A	Fm-3m (225)	(Kulcu, 1987)	P-8 "Pb", P-11 "Pb+Cl"
Na$_2$Te$_2$O$_7$	35-1263	N/A	Imm2 (44)	(Knop and Demazeau, 1981)	P-2 "Al/B+Cl"
Ba$_3$WO$_6$	33-0182	N/A	Fm-3m (225)	[b]	W-12 "W+Cl"
Zn$_2$Te$_3$O$_8$	89-4454	50705	$C2/c$ (15)	(Feger et al., 1999)	P-13 "Zn+Cl"

[a] Blanchard, F., Department of Geology, University of Florida, Gainesville (1990).

[b] National Bureau of Standards (U.S.) Monogr. 25, **19**, p 21 (1982).

N/A: not applicable

4.3.1.2 *Raman Spectroscopy*

Raman spectroscopy was performed to approach the tellurite glass structure from a different angle than other possible techniques such as XRD. Raman addresses the length scale that is below XRD and will ID short range symmetrical structures at the nearest and next nearest neighbor level.

Figure 4.24 shows example results for the Raman curve fitting for the lead-tellurite "P-series" glasses. Assignments for tellurite bands **A** through **E** have been made according to Table 3.13 with structural representations of these units derived from the literature and presented in Figure A.1 (Appendix A). Raman spectra for the specimens with and without XCl$_{20}$ are shown in Figure 4.25. Peak wavenumbers ($\tilde{v}$) and areal intensity determined from the fitting are shown in Table 4.11. In all cases except the PbO-containing glasses (P-8 "Pb" and P-11 "Pb+Cl"), **A** and **B** bands assigned to TeO$_3$ and TeO$_{3+1}$ *tp* groups could not be distinguished, so they were assigned to **A**, the higher frequency band. In only two cases, P$_2$O$_5$-containing and PbO-containing glasses, could a **D** band, assigned to Te-O asymmetric stretch in TeO$_2$, be distinguished. A summary of peak fitting for the different glass systems is presented below.

- **PbO-glasses** (P-8 "Pb" and P-11 "Pb+Cl"). Fitting all of the tellurite bands **A** (*tp*), **B** (*tp*), **C** (*tbp*), **D** (*tbp*), and **E** (Te-O-Te) was required.

- **Al$_2$O$_3$/B$_2$O$_3$-glasses** (P-7 "Al/B" and P-2 "Al/B+Cl"). Spectra were fitted with **A** (*tp*), **C** (*tbp*), and **E** (Te-O-Te) tellurite bands. Additional bands were observed at ~840 cm^{-1} and, in the case without chlorides, at ~1300 cm^{-1}. Both of the aforementioned bands were assigned to B-O-B(III) in pyroborate structures, though the latter band has been also applied to Al(IV) substituting for B(IV) in the borate network (Brow et al., 1997; Li et al., 2003).

- **WO$_3$-glasses** (P-9 "W" and P-12 "W+Cl"). The fit of current data incorporated tellurite bands **A** (*tp*), **C** (*tbp*), and **E** (Te-O-Te). In addition, another band was observed in the **E** envelope (408–412 cm^{-1}) distinct from the ~360 cm^{-1} band, which is also visible in the spectra (Figure 4.25c) and previously assigned to deformation vibrations of WO$_6$ (Chowdari and Kumari, 1999; Sekiya et al., 1994a). In the fitting procedure, the three apparent bands in the 300–600 cm^{-1} region were fit with only two bands as shown in Table 4.11. Bands ~860 and ~930 cm^{-1} were assigned to W-O stretches internal and external to the clusters, respectively (see Table 3.13).

- **P$_2$O$_5$-glasses** (P-5 "P" and P-14 "P+Cl"). Glasses in the current study were fit with six Raman bands, including four of the tellurite bands: **A** (*tp*), **C** (*tbp*), **D** (*tbp*), and **E**. Raman fitting required two peaks in the envelope of the **E** peak assigned to the Te-O-Te bending vibrations (see Table 3.13). Normally the P-O-P bending vibrations are at lower wavenumbers, i.e., $\tilde{v} < 300$ cm^{-1}, but it is possible

that some band mixing occurred to cause the asymmetry in this first peak. One or two weak peaks around 1000 cm^{-1} can be ascribed to PO$_4$ groups with one or two non-bridging oxygens.

- **ZnO-glasses** (P-4 "Zn" and P-13 "Zn+Cl"). Spectra in the current study were adequately fit with only three tellurite bands: **A** (*tp*), **C** (*tbp*), and **E** (Te-O-Te bending).
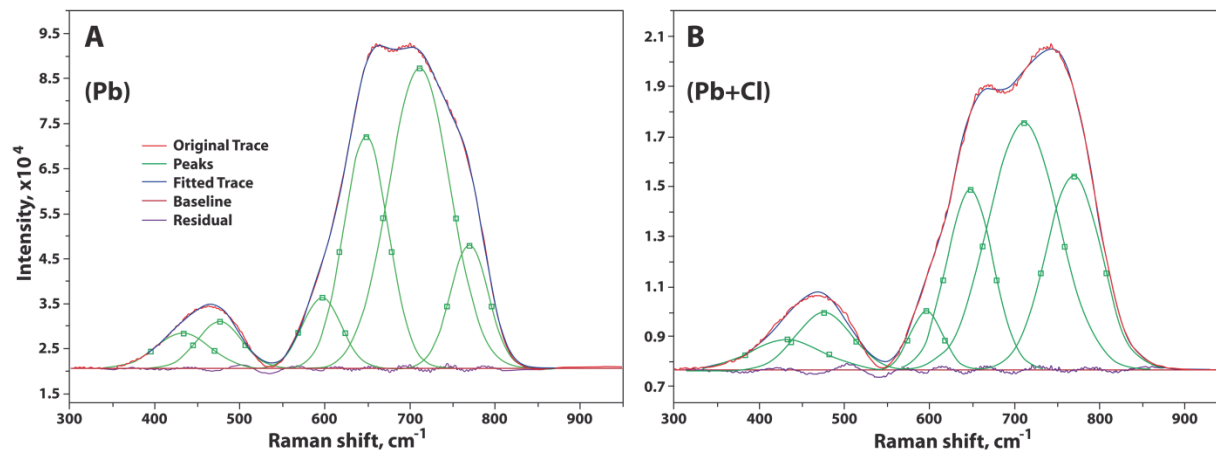
Figure 4.24. Examples of curve fitting for (A) Pb (P-8) and (B) Pb+Cl (P-11) glasses.
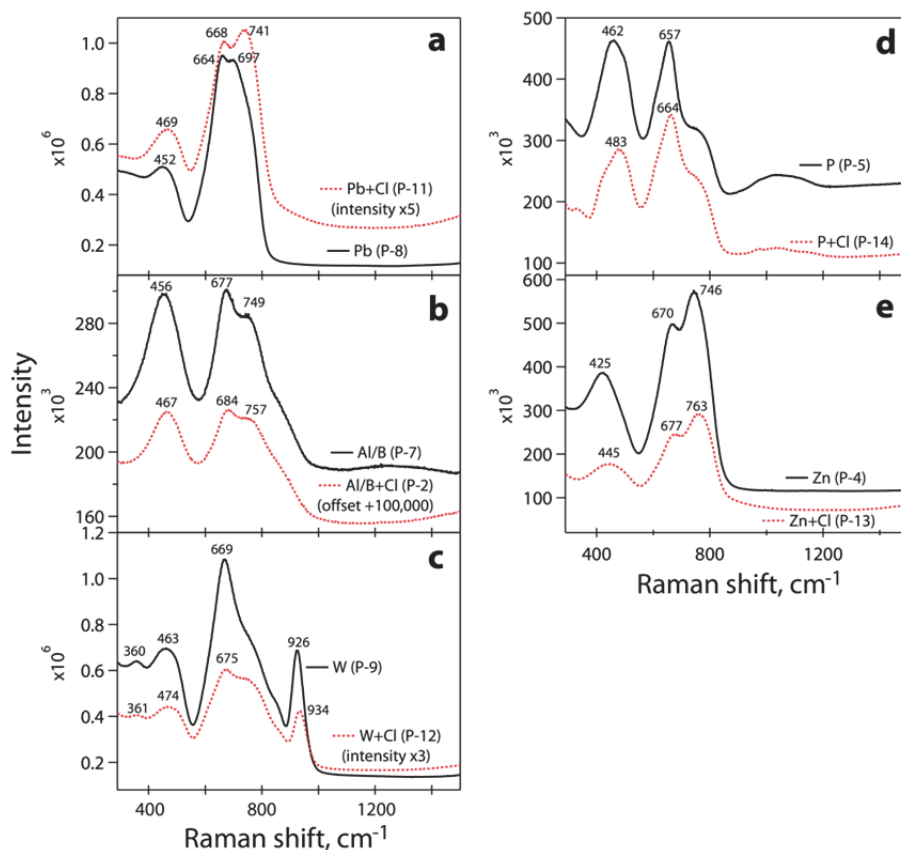
Figure 4.25. Raw Raman spectra without backgrounds removed for glasses with and without XCl$_{20}$ (listed as "Cl"). Spectra are not offset but are shown as collected unless otherwise noted. (a) PbO-glasses P-8 (bottom, black) and P-11 (top, red, intensity 5× from measured); (b) Al$_2$O$_3$/B$_2$O$_3$-glasses P-7 (top, black) and P-2 (bottom, red, offset +100,000 counts); (c) WO$_3$-glasses P-9 (top, black) and P-12 (bottom, red, intensity 3× from measured); (d) P$_2$O$_5$-glasses P-5 (top, black) and P-14 (bottom, red); and (e) ZnO-glasses P-4 (top, black) and P-13 (bottom, red).

Table 4.11. Results of quantitative fitting of Raman bands on P-series glasses. This table consists of peak location in wavenumber ($\tilde{v}$, ±1 cm^{-1}) and integrated intensity, I. Note that these glasses were fitted with peak frequencies allowed to float (not fixed).

Glass ID	Composition	R^2 of fit	A		B		C		D		E		other	
			$\tilde{v}$	I	$\tilde{v}$	I	$\tilde{v}$	I	$\tilde{v}$	I	$\tilde{v}$	I	$\tilde{v}$	I
P-8	Pb	0.9998	770	1.55E+07	711	6.03E+07	648	3.40E+07	597	9.10E+06	476	6.21E+06	433	6.27E+06
P-11	Pb+Cl	0.9996	770	6.36E+06	711	1.01E+07	648	4.87E+06	597	1.15E+06	476	1.90E+06	433	1.33E+06
P-7	Al/B	0.9990	764	4.53E+06	-	-	676	9.72E+06	-	-	457	1.10E+07	843	4.78E+06
													1295	1.38E+06
P-2	Al/B+Cl	0.9993	774	1.83E+06	-	-	686	6.99E+06	-	-	468	5.24E+06	846	3.74E+06
P-9	W	0.9974	765	6.06E+07	-	-	662	6.66E+07	-	-	481	1.73E+07	412	1.24E+07
													856	5.50E+06
													927	2.65E+07
P-12	W+Cl	0.9984	762	1.55E+07	-	-	657	8.29E+06	-	-	483	2.89E+06	408	1.52E+06
													868	5.47E+05
													935	4.02E+06
P-5	P	0.9984	756	9.83E+06	-	-	655	1.50E+07	559	3.23E+06	447	1.50E+07	505	7.14E+06
													1046	5.58E+06
P-14	P+Cl	0.9993	756	1.20E+07	-	-	661	1.81E+07	598	3.57E+06	418	2.38E+06	484	1.44E+07
													1042	4.53E+06
P-4	Zn	0.9987	757	4.27E+07	-	-	659	2.88E+07	-	-	430	1.70E+07	-	-
P-13	Zn+Cl	0.9987	770	1.89E+07	-	-	669	1.28E+07	-	-	447	5.42E+06	-	-

As a rough estimate of the fraction of *tp* units as compared to *tbp* units (TeO_3/TeO_4) in the glass, areal intensity ratios were taken from the fitted spectra of the intensity of the **A** band to that of the **C** band, i.e., $I(\textbf{A}$ band$)/I(\textbf{C}$ band$)$ (Chowdari and Kumari, 1999; Himei et al., 1994). These corresponding ratios are shown in Table 4.12. It should be noted that these ratios seem to imply similar Raman cross-sections between the various bands, which might not necessarily be the case. Because it was not always clear whether the bands in the region (i.e., 720–780 cm^{-1}) should be assigned to **A** or **B**, the intensity ratio of **A** + **B** to the **C** band, i.e., $I(\textbf{A} + \textbf{B}$ bands$)/I(\textbf{C}$ band$)$, was also analyzed. Only the data for the PbO-containing glasses P-8 (Pb) and P-11 (Pb+Cl) were influenced by this approach.

Table 4.12. Ratios of key tellurite peaks from the Raman data. Since "**B**" was only observed in the Pb-containing glasses, the ratio $I(\textbf{A} + \textbf{B})/I(\textbf{C})$ is only different from $I(\textbf{A})/I(\textbf{C})$ for these glasses.

Glass ID	Composition	$I(\textbf{A})/I(\textbf{C})$	$I(\textbf{A} + \textbf{B})/I(\textbf{C})$	Mole% oxide additive	Crystalline phases after PCT
P-8	Pb	0.46	2.23	16.8	$PbTe_3O_7$
P-11	Pb+Cl	1.31	3.38	13.1	$PbTe_3O_7$
P-7	Al/B	0.47	0.47	29.5	α-TeO_2
P-2	Al/B+Cl	0.26	0.26	24.9	β-TeO_2, $Na_2Te_2O_7$
P-9	W	0.91	0.91	18.7	None
P-12	W+Cl	1.87	1.87	14.5	Ba_3WO_6
P-5	P	0.66	0.66	10.0	α-TeO_2
P-14	P+Cl	0.66	0.66	7.9	β-TeO_2
P-4	Zn	1.48	1.48	30.1	α-TeO_2, $Zn_2Te_3O_8$
P-13	Zn+Cl	1.48	1.48	24.5	β-TeO_2, $Zn_2Te_3O_8$

As stated by Himei et al., all of these band ratios should be properly corrected by a *y*-intercept when against O/Te on a molar basis (Himei et al., 1994). However, we elected not to follow this approach because we were more interested in comparing the influence of primary dopants and the presence of mixed chlorides on the structural variation(s) between glasses in each binary/ternary system. Glasses with $I(\textbf{A}) < I(\textbf{C})$ should have more TeO_4 units, and those with ratios > 1 should have more TeO_3 units. Ratios that decrease in the XCl$_{20}$-containing glass should indicate presence of more TeO_4 than glasses without XCl$_{20}$, while ratios that increase should indicate more TeO_3. Glasses with ratios < 1 include almost all of the glasses: P-8 (Pb), P-11 (Pb+Cl), P-7(Al/B), P-2 (Al/B+Cl), P-9 (W), P-5 (P), and P-14 (P+Cl). Glasses predicted to have primarily TeO_3 units include P-12 (W+Cl), P-4 (Zn), and P-13 (Zn+Cl). It is likely that results for P-9 (W) and P-12 (W+Cl) are influenced by peaks from the W network because, according to Sekiya et al., bands **A**, **B**, and **C** all have contributions from the W-network modes while **E** contains only contributions from the Te network (Sekiya et al., 1994a). Therefore, it is difficult to comment on the P-9 (W) and P-12 (W+Cl) with only the Raman spectra.

It was instructive to compare the ratios for the Zn glasses with those of the Al/B glasses. These four glasses had nearly identical molar additions of oxides to the TeO_2. However, the Zn glasses (P-4 and P-13) were highly depolymerized (i.e., the TeO_4 *tbp* units have been changed to mostly TeO_3 *tp* units), as observed in other studies. This is because the ZnO breaks the Te-O chains and only secondarily acts as a glass former. In Al/B glasses (P-7 and P-2), however, only TeO_4 units are expected from TeO_2-B_2O_3 systems (Rong et al., 1992). This leaves 8–9 mole% Al_2O_3, which creates ~15% *tp* groups based on NMR of TeO_2-Al_2O_3 (Sakida et al., 2001). Ignoring the role of B_2O_3, for 8–9 mole% Al_2O_3, one would estimate ~45% Al in AlO_6, ~20% in AlO_5, and ~34% in AlO_4, though it is unknown how the simultaneous presence of B_2O_3 would affect the Al speciation (Sakida et al., 2001). When adding XCl$_{20}$ to these glasses, the spectra for the P-13 (Zn+Cl) glass did not noticeably change while the ratios decreased for P-2 (Al/B+Cl), indicating that even more TeO_4 formed. These differences are important when considering the radically different behavior of the Zn glasses (P-5 and P-14) and Al/B glasses (P-7

and P-2) in chemical durability tests. As shown Table 4.13, in P-4 (Zn) P-13 (Zn+Cl) glasses were very soluble, whereas the P-7 (Al/B) and P-2 (Al/B+Cl) glasses were only slightly soluble, i.e., P-13 (Zn+Cl) showed very high NL_{Na} at 88.9 g/m^2 and P-2 (Al/B+Cl) showed low NL_{Na} at 6.71 g/m^2.

For the Pb glasses, P-8 and P-11, the estimated fraction of *tp* from NMR data in the literature is ~33% for the ~17 mole% PbO-TeO$_2$ glass, which is similar to our glass without chlorides (Sakida et al., 2001). This suggests that the ratio $I(\mathbf{A})/I(\mathbf{C})$ is more reliable than NMR. The value of this ratio is < 1 (*tbp* > *tp)*, while $I(\mathbf{A} + \mathbf{B})/I(\mathbf{C})$ is > 1 (*tbp* < *tp)*. The fraction of *tp* for P-8 (Pb) glass estimated from NMR (~33%) is significantly greater than that estimated for the P-7 (Al/B) glass (~15% *tp*) but the amount of *tp* clearly decreased in P-11 (Pb+Cl) glass when chlorides were added.

Though P-5 (P) and P-14 (P+Cl) glasses showed predominantly *tbp* structures, their chemical durability was very poor. The P+Cl glass was phase-separated, the leachate from this glass was highly enriched in P, and the residual solids were composed primarily of crystalline β-TeO$_2$ (Riley et al., 2010). Kozhukharov et al. (1978) investigated the TeO$_2$-P$_2$O$_5$ binary system for regions of miscibility/immiscibility and found that uniform glass was formed at 3–15 mole% P$_2$O$_5$. However, many complex immiscible phases also occurred at various temperatures within this region. These results could explain the incongruent leaching observed during the PCT as well as the phase separation.

4.3.1.3 *Chemical Durability Analysis*

The chemical durability of the glasses studied here did not appear to fit an obvious trend and varied widely from NL_{Na} = 0.478 to 88.9 g/m^2 release over the course of the seven-day PCT (see Table 4.13). The variation was attributed to phase separation in some of the glasses and the ratio of *tp:tbp* structural units. The Pb+Cl (P-11) glass showed the highest chemical durability, W+Cl (P-12) and Al/B+Cl (P-2) were only somewhat durable, and P+Cl (P-14) and Zn+Cl (P-13) showed poor chemical durability. The reduced chemical durability in the Al/B+Cl (P-2) and P+Cl (P-14) glasses was likely due to phase separation, which was clearly visible in these glasses with the naked eye (Riley et al., 2010).

Table 4.13. Summary of normalized release results from seven-day PCT-B for P-series tellurite glasses with XCl$_{20}$. More details are provided in our earlier work such as ranges/deviations (Riley et al., 2010).

Glass ID	Composition	NL_{Li} (g/m^2)	NL_{Na} (g/m^2)	NL_K (g/m^2)	NL_{Cl} (g/m^2)
P-11	Pb+Cl	1.00	0.478	0.298	0.528
P-2	Al/B+Cl	5.50	6.72	3.45	3.85
P-12	W+Cl	7.25	10.3	2.85	4.62
P-14	P+Cl	82.7	86.0	88.4	30.3
P-13	Zn+Cl	85.3	88.9	89.1	84.7

Although the Pb+Cl glass, P-11, performed very well in the PCT, it had a $I(\mathbf{A})/I(\mathbf{C})$ ratio similar to that of the Zn+Cl glass (P-13), which performed the worst of all the glasses studied (NL_{Na} = 88.9 g/m^2), implying similar *tp:tbp* fractions in these two glasses (see Table 4.12). However, since the Pb glasses, P-8 and P-11, also had a **B** band present adding to the *tp* signal (>60%), the fraction of *tp* units in the Pb+Cl glass was the highest of the glasses studied, i.e., $I(\mathbf{A} + \mathbf{B})/I(\mathbf{C})$. This suggests that perhaps the *tp* structure is necessary to increase chemical durability, although more work is needed to verify the difference between the **A** and **B** bands since the **B** band did not appear in any of the glasses other than the Pb glasses and seem to contribute significantly to the *tp* unit signal.

The Al/B+Cl glass, P-2, was the second-best-performing XCl$_{20}$-loaded glass, with NL_{Na} = 6.72 g/m^2. However, the Al/B+Cl and Pb+Cl (P-11) glasses were an order of magnitude apart in NL_{Na} and the leaching appeared very different in each glass. The leaching in the Al/B-glasses, P-7 and P-2, appeared incongruent, likely due to the fact that the Al/B+Cl glass was visibly phase-separated before the PCT; also, the PCT leachate was enriched in B and Cl. Interestingly, the total dissolved Al species measured in

the PCT leachates from both the Al/B-glasses was very low (Riley et al., 2010). Also, the dissolved B species measured in the PCT leachates for the Al/B glass was nearly double (1.855×) that in the Al/B+Cl glass, whereas the amount of B_2O_3 present in the Al/B+Cl glass was not very different from that in the Al/B glass (P-7, 8.1 versus 9.0 mass%) (Riley et al., 2010).

4.3.1.4 Thermal analysis

The P-8 (Pb) and P-11 (Pb+Cl) P-series lead-tellurite glasses were studied with the TA Instruments SDT Q600 DTA-TGA and the results are presented in Table 4.14 and Figure 4.26. The T_g of P-8 (~291 °C) is comparable to a typical tellurite glass and when 10 mass% of XCl_{20} was added to P-8 to produce the P-11 glass, the T_g was reduced to ~254 °C for the 10 °C/min ramp rate. The temperature stability of these glasses can be increased by incorporating additional components into the glass, such as GeO_2 and Al_2O_3; these options are currently under investigation (Hocdé et al., 2004).

Table 4.14. Summary of DTA-TGA results for P-8 and P-11 run at both 10 and 15 °C/min ramp heating rates.

Glass ID	Rate, °C/min	Mass, mg	T_g, °C	Peak ID	T_x (onset), °C	T_c (max), °C	T_M, °C
P-8	10	75.549	290.53	(1)	321.37	334.42	524.22
				(2)	371.98	387.26	620.10
	15	67.482	288.68	(1)	321.00	334.15	522.09
				(2)	374.79	390.59	619.90
P-11	10	34.805	253.90	(1)	392.36	417.02	536.38
				(2)	-	-	-
	15	33.378	264.00	(1)	326.79	340.06	542.38
				(2)	366.59	395.03	
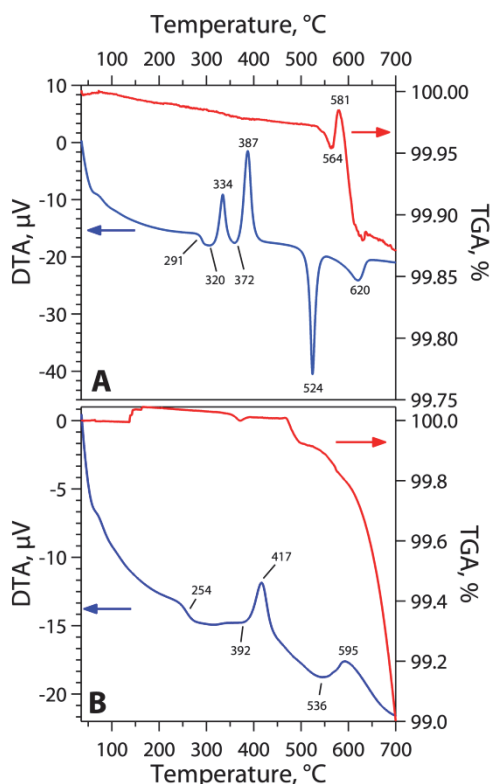
Figure 4.26. DTA/TGA results for (A) P-8 and (B) P-11 collected during heating.

In addition, the thermal diffusivity was measured for P-11 with a NETZSCH LFA-457. In order to perform these measurements, discs of the specimens were prepared from cylinders cast in fused quartz molds (see Figure 3.3). The thermal diffusivity for P-11 was measured at $0.23–0.28\times10^{-6}$ m^2/s and these results are presented in Figure 4.27a. We did prepare a disc of P-8 for thermal diffusivity measurements, although the glass tends to crystallize when we try to pour and anneal cylinders that can be cut into discs (see Figure 4.27b). These crystals would make it difficult to accurately measure the thermal diffusivity for the glassy phase.
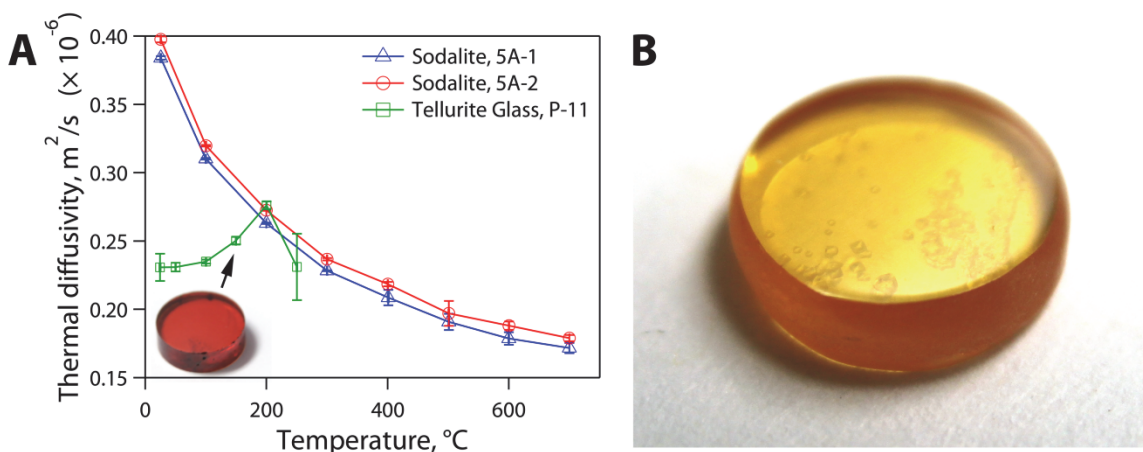
Figure 4.27. (A) Thermal diffusivity, α, for tellurite glass, P-11, as well as PNNL Sodalite, 5A, as a function of temperature. (B) A P-8 specimen prepared for LFA measurements (~1 cm in diameter); it is slightly crystallized (see small, clear $Pb_2Te_3O_7$ crystals throughout the bulk).

4.3.2 Tellurite Glasses: Lead-Tellurite and Structural Variation Glasses Study

4.3.2.1 Visual Appearance

The lead-tellurite glasses appeared very different from one another; TPb_0 was a transparent yellow-orange glass; TPb_5, TPb_{10}, $TPb_{12.5}$, and TPb_{14} were transparent red glasses; TPb_{15} was phase-separated; and $TPb_{17.5}$, $TPb_{22.5}$, and TPb_{30} were dark yellow-white and opaque ceramic-like in appearance (Figure 4.28). Phase separation was observed at 15% XCl$_{20}$-loading, although not at 14%. Thus, the XCl$_{20}$-loading limit was determined to be between 14% and 15% in this lead tellurite system (TeO$_2$:PbO = 3.545, by mass).
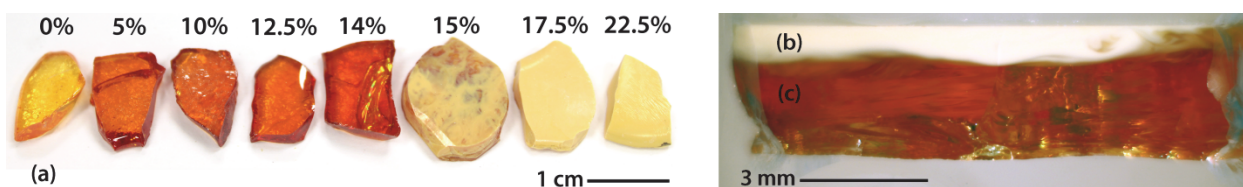
Figure 4.28. (a) Pictures of lead-tellurite glasses at different waste loadings. (b,c) A polished cross-section of the two phases present in the phase-separated T2G-1-PbO specimen (Riley et al., 2010). Note that TPb_{30} is not shown but looks identical to $TPb_{22.5}$.

The structural variation set of glasses are presented in Figure 4.29. While these glasses were quite different in color, the crystalline/amorphous nature varied only slightly; some made very nice glasses (e.g., T2G-33 and T2G-34) while others were highly crystalline (e.g., T2G-21b–d). All of these glasses had very low viscosities during melting/pouring. For all of the lead-tellurite glasses, a temperature of 700 °C was sufficient for melting. For the ZnO-based glasses, T2G-29a and T2G-29b, a higher temperature of 730 °C was required for melting. Some volatilization was observed for T2G-29a, T2G-32, and T2G-33 whereas no volatilization was observed for T2G-27a, T2G-27b, or T2G-34.
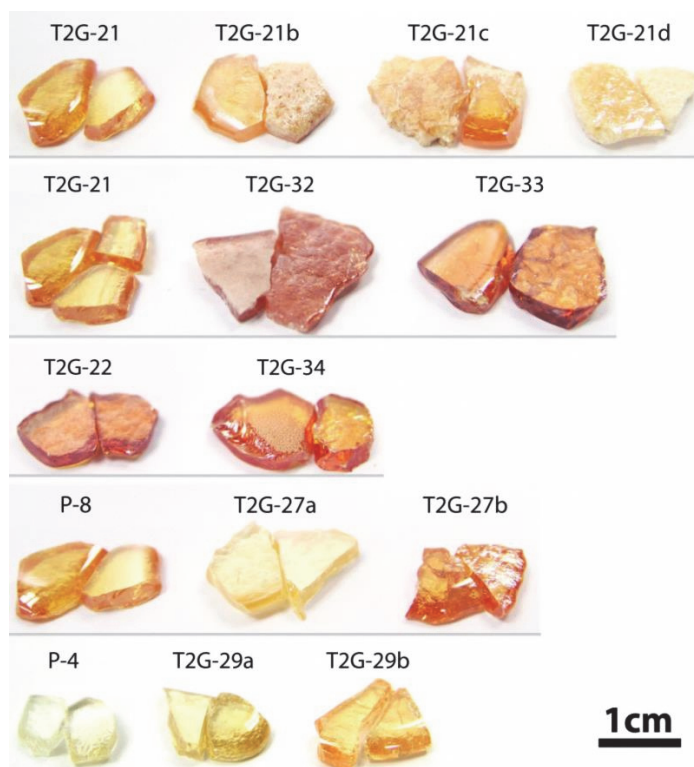
Figure 4.29. Summary figure providing visual comparisons between the structural variation glasses. Here, T2G-21 was used as a placeholder for P-8 since they have identical compositions and appearances.

4.3.2.2 Density Analysis

Adding XCl_{20} to the baseline lead-tellurite glasses decreased the density, as one would expect considering that the density of the waste components, ρ_{salt}, is lower than that of the glass, ρ_b, at $< 3\times10^3$ kg/m^3 vs. $> 6\times10^3$ kg/m^3, respectively (see Table 3.4 and Figure 4.30a). This does not account for a density difference between the individual phases present in the phase-separated glasses. Figure 4.30b shows the storage densities (ρ_{sd}) of the different glasses as functions of waste loading. The concept of ρ_{sd} is presented here to show the large difference between the volumetric waste loading of the tellurite glasses compared to that of the baseline glass-bonded sodalite (163 kg/m^3). A waste form with a high ρ_{sd} is preferred because it will require a smaller volume to store an equivalent mass of waste. For comparison, the final glass-bonded sodalite baseline waste form for the Echem waste is ~90% of its theoretical density with $\rho_b = 2170$ kg/m^3, ~7.5 mass% waste loading, giving $\rho_{sd} = 163$ kg/m^3.
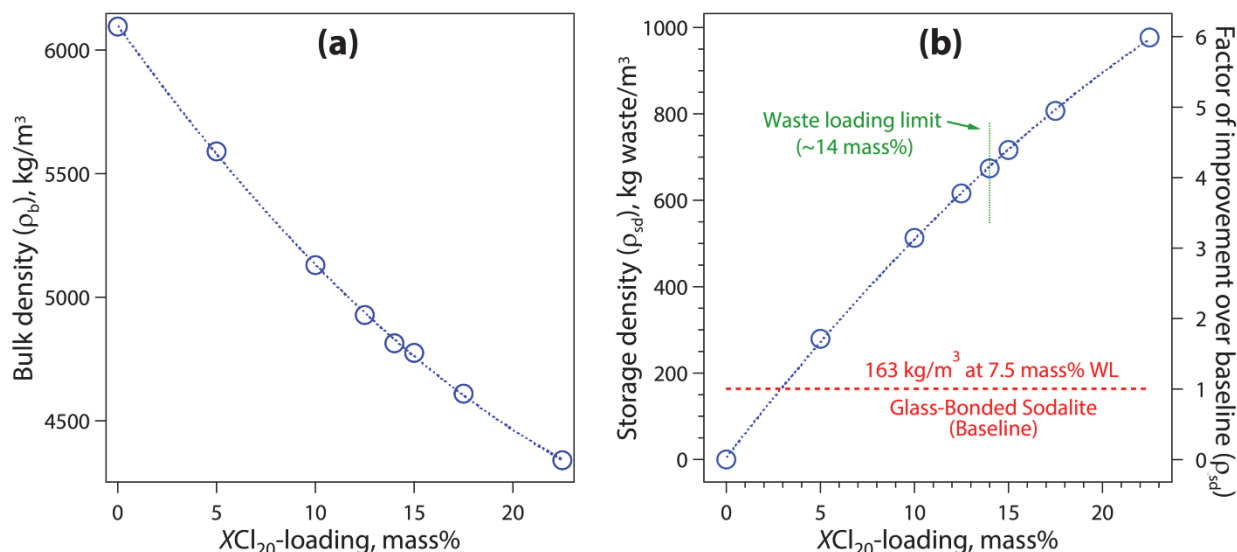
Figure 4.30. (a) Bulk density (ρ_b) and (b) storage density (ρ_{sd}) of the lead-tellurite glasses as a function of XCl_{20}-loading. In (b) a comparison is given to the baseline glass-bonded sodalite.

4.3.2.3 Raman Analysis

Micro-Raman analysis of the two phases in T2G-1-PbO (Figure 4.28) revealed that, qualitatively, the **B** (*tp*) band was substantially larger than the **C** (*tbp*) band in phase (a) when compared to phase (b), as seen in Figure 4.31—see Table 3.13 for band assignments. This implies that the *tbp* units are more prevalent in phase (b), suggesting that alkali and/or chlorine enrichment in phase (a) leads to more depolymerization of the tellurite network (i.e., more *tp* TeO$_3$ or TeO$_{3+1}$ units). The strongest, cleanest micro-Raman signal of the white phase was analyzed quantitatively as well. Microscopy and XRD did not indicate that the white phase was crystalline, but it could have been phase-separated on a very small scale.
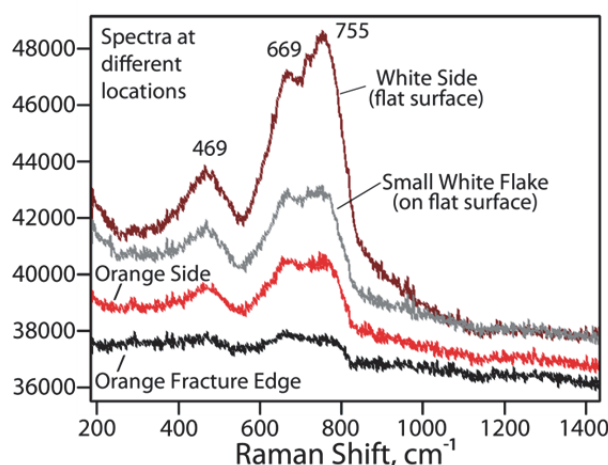
Figure 4.31. Micro-Raman spectroscopy of separated phases in T2G-1-PbO (same composition as TPb$_{15}$).

The glass structure in the lead-tellurite and some of the structural variation glasses was further assessed by investigating the Raman spectra. Some representative Raman spectra are shown in Figure 4.32. From both parts of Figure 4.32 it can clearly be observed that adding XCl$_{20}$ to these glasses reduces the overall Raman intensity. Spectra were fitted as previously described, and the resultant area deconvolution is shown in Table 4.15 according to the bands assigned in Table 3.13.
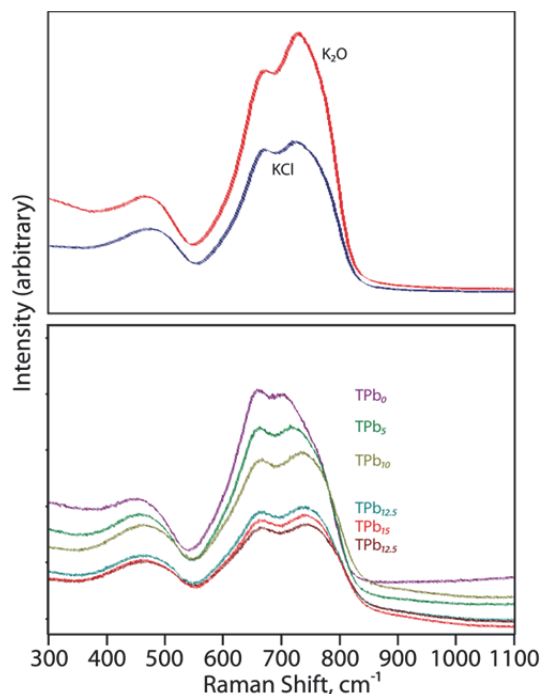
Figure 4.32. Raman spectra of K$_2$O and KCl glasses (top) and some of the lead-tellurite glasses (bottom).

Table 4.15. Fitted Raman data for lead-tellurite and some of the structural variation study glasses. The band names are listed in **bold** type. Note that the frequencies were fixed during the fitting and are shown at the top of each column of integrated intensities.

Name	Alternate Name	$\tilde{\nu}$ (cm^{-1}): 432.7 **E1**	476 **E2**	596.5 **D**	648 **C**	710.9 **B**	769.7 **A**
TPb$_0$	T2G-21	3.84E+05	2.40E+05	3.73E+05	1.48E+06	2.49E+06	6.82E+05
P-8	-	6.27E+06	6.21E+06	9.10E+06	3.40E+07	6.03E+07	1.55E+07
TPb$_5$	T2G-22	3.49E+05	3.53E+05	3.27E+05	1.22E+06	2.14E+06	1.04E+06
TPb$_{10}$	T2G-23	2.50E+05	4.60E+05	2.78E+05	8.59E+05	1.77E+06	1.06E+06
P-11	-	1.33E+06	1.90E+06	1.15E+06	4.87E+06	1.01E+07	6.36E+06
TPb$_{12.5}$	T2G-24	1.99E+05	4.02E+05	1.98E+05	5.86E+05	1.43E+06	7.83E+05
TPb$_{14}$	T2G-30	3.07E+05	9.46E+05	5.80E+05	1.46E+06	3.41E+06	2.11E+06
TPb$_{14-repeat}$	T2G-30b	4.35E+04	9.69E+04	2.45E+04	1.57E+05	4.56E+05	2.56E+05
TPb$_{15-powder}$	T2G-1	1.39E+05	4.46E+05	1.32E+05	4.56E+05	1.32E+06	6.58E+05
TPb$_{15-white}$	T2G-1	8.03E+04	1.11E+05	3.01E+04	2.60E+05	4.84E+05	4.45E+05
TPb$_{17.5}$	T2G-25	2.16E+05	4.47E+05	1.80E+05	5.02E+05	1.52E+06	7.30E+05
TPb$_{22.5}$	T2G-30	9.58E+04	2.91E+05	1.15E+05	4.53E+05	1.20E+06	6.84E+05
K$_2$O	T2G-27a	6.17E+05	6.85E+05	1.00E+06	2.67E+06	7.70E+06	2.89E+06
KCl	T2G-27b	6.35E+05	6.42E+05	4.85E+05	1.93E+06	4.57E+06	1.74E+06
XO$_{20}$	T2G-34	5.71E+04	7.92E+04	1.09E+05	3.08E+05	7.55E+05	3.02E+05

A progression of the *tbp*/*tp* relative ratio, which indicates polymerization of the tellurite network, as determined from the area ratio (**C** + **D**)/(**A** + **B**) in the high frequency envelope, is shown in Figure 4.33a. The trend is a smooth decrease until about 15 mass%, after which it remains nearly unchanged. Waste loadings 0, 10, 14, and 15 mass% have two data points each, and the line is an average ratio of the two (Figure 4.33a). Noting that the 14 mass% points are considerably different, it may be that the 14 mass% glass is on the verge of major structural change associated with devitrification, and slightly different cooling profiles produce different glass structures. It should be remembered that 15 mass% XCl$_{20}$ represented the point at which phase separation began to be visibly apparent. One of the data points at 15 mass% represents the Raman spectra taken on a powdered glass containing both phases, and the other is a fit of the white phase micro-Raman data. In contrast with the 14 mass% data, these 15 mass% ratios are remarkably similar to each other. At loadings higher than that inducing phase separation, it appears that the relative depolymerization of the tellurite network (as measured by *tbp*/*tp*) proceeds no further. From the micro-Raman and EDS on the phase-separated 15 mass% XCl$_{20}$, the orange-red glassy phase is enriched in Te and has more *tbp* groups than the cloudy-whitish phase that is enriched in alkali, Cl, and slightly in Pb, and has more *tp* groups.

Figure 4.33b shows a plot of the peak width as a function of waste loading for several of the Raman bands fitted with fixed frequencies. It is apparent that at least up to 15 mass% XCl loading and probably higher, the band width for **A** + **B** bands assigned to *tp* units increases, indicating increased local site disorder. By contrast, the band width of the **C** + **D** bands assigned to *tbp* units do not change much with mixed chloride loading. This implies that the disorder with increasing additions of alkali, alkaline earth, lanthanide, and chloride ions manifests in the *tp* structural units, which makes sense since it is these

depolymerized tellurite units that accommodate these ions in the glass structure. Since there are so many different waste ions to be incorporated, it seems reasonable that as the loading is increased, the number of different local *tp* units would increase (i.e., the disorder increases). This effect seems to saturate near 15 mass% as also was seen with the area ratios in Figure 4.33a, and data in Figure 4.33b for the *tp* peaks (**A + B**) are also not inconsistent with a change in mechanism near 15 mass%, but data are more scattered for the peak width.
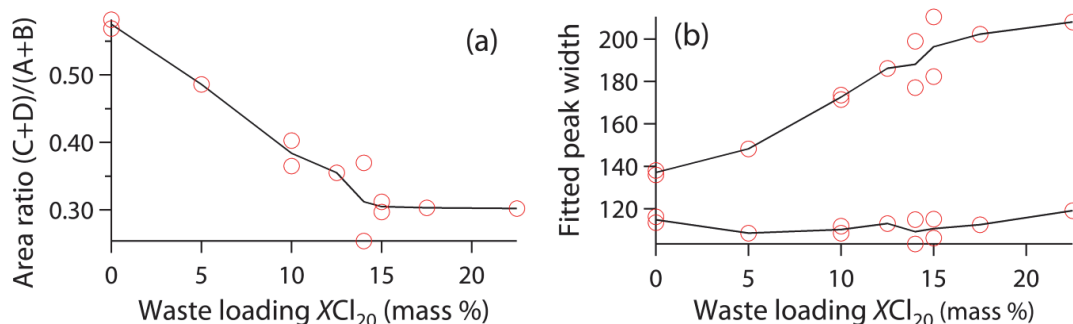
Figure 4.33. Quantitative Raman analysis for the lead-tellurite glasses. (a) *tbp/tp* area ratio from Raman spectra as a function of waste loading. **A** lower (**C+D**)/(**A+B**) ratio represents a more depolymerized network. (b) Fitted peak width as a function of loading, indicating site disorder in the *tp* part of the glass structure with increasing waste loading. In both figures, lines indicate averages where more than one data point (circle) is shown.

An examination of the effect of Cl/O ratio for the structural variation glasses is shown in Table 4.16. From this data we can examine the effects of both Cl and cations. Comparing the TPb_0 and TPb_5 specimens, the addition of 5 mass% XCl_{20} results in a depolymerization of the network (lower area ratio), but it is not entirely clear whether this is due to the Cl or the cations in the waste or both. Comparing TeO_2-PbO-XO_{20} (T2G-34) and TeO_2-PbO-XCl_{20} (TPb_5) gives an idea of the separate effects of the cations and chloride, since the amounts of Te and Pb relative to the waste cations is the same for both the oxide and the chloride waste. The data indicate that the chloride in XCl_{20} actually *repolymerizes* the tellurite network compared to the XO_{20} glass with the same modifier cations, presumably by scavenging some of the alkali (or possibly alkaline earths and/or lanthanides), reducing the amount available for network breaking and formation of *tp* units. Finally, comparison of the K_2O and KCl glasses having the same relative amount of K compared to Te and Pb (see Table 3.10), indicates the same trend, i.e., that the chloride-containing glass is slightly more polymerized than the one without chloride when both contain the same relative amount of alkali to the main glass formers. This is in agreement with Tanaka et al., who observe a suppression of formation of the *tp* units when Cl is substituted for O in Li-Te-O-Cl glasses due to the strengthening of the Te-O_{ax} bond since a smaller electronic charge is donated from Te-Cl_{eq} than from Te-O_{eq} (Tanaka et al., 1988a)—see Figure A.1.

Table 4.16. Quantitative Raman analysis of some of the lead-tellurite and structural variation glasses.

Sample ID	Glass System	Cl/O	(C+D)/(A+B)
T2G-21 (TPb_0)	TeO_2-PbO (TPb_0)	0.000	0.58
T2G-22 (TPb_5)	TeO_2-PbO-XCl (TPb_5)	0.080	0.49
T2G-34 (XO_{20})	TeO_2-PbO-XO	0.000	0.39
T2G-29a	TeO_2-PbO-K_2O	0.000	0.35
T2G-29b	TeO_2-PbO-KCl	0.096	0.38

4.3.2.4 X-Ray Diffraction (XRD) Analysis

The XRD results for the lead-tellurite glasses are presented in Figure 4.34 where the best-fitting phases were identified as those presented in Table 4.17. XRD analysis showed a small fraction of octahedral

lead tellurite ($Pb_2Te_3O_7$) crystals in TPb_0 observed with optical microscopy (Kulcu, 1987). TPb_5, TPb_{10}, $TPb_{12.5}$, and TPb_{14} were determined to be amorphous whereas TPb_{15}, $TPb_{17.5}$, and $TPb_{22.5}$ showed small degrees of crystallization. The glasses with XCl_{20}-loadings at ≥15 mass% looked highly crystalline, so the small degree of crystallization was surprising considering their visual appearance. Later, with SEM, we verified that the observed color change was the result of nano-phase-separation of alkali chloride inclusions in the yellow-white phase (see Figure 4.36). At 15 mass% loading, a small fraction of PbO was observed in the diffraction pattern. This PbO was not observed as a crystalline product in any of the other glasses. At XCl_{20}-loadings >15 mass%, chloride phases were observed. At an XCl_{20}-loading of 17.5 mass% ($TPb_{17.5}$), $NaClO_3$, Ba_4OCl_6, and $BaPrO_3$ were the best-fitting patterns and at an XCl_{20}-loading of 22.5 mass% ($TPb_{22.5}$), KCl, NaCl, $CsPbCl_3$, and K_2PrCl_5 were the best-fitting patterns. Since $CsPbCl_3$ is the only one of these seven phases that contains the glass-forming components, this suggests that the waste-loading limit was achieved because the waste components were no longer stable in the glass network.
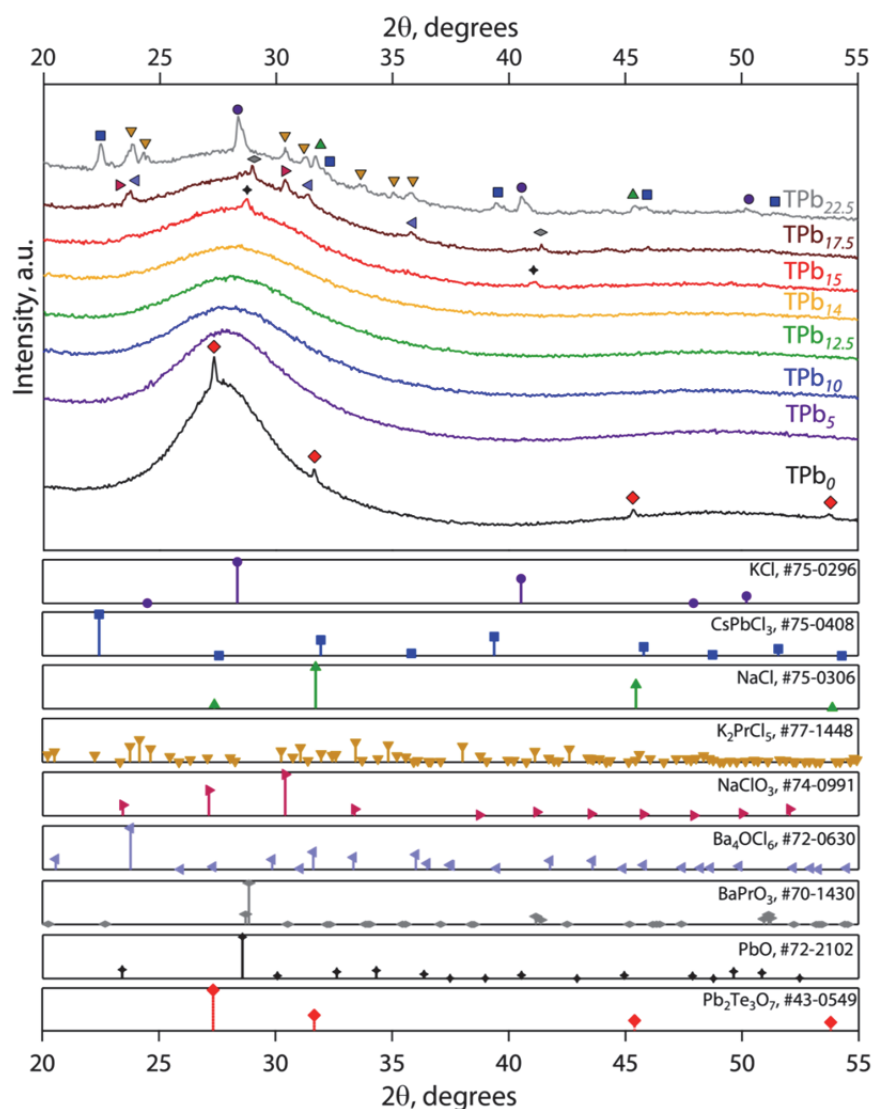
Figure 4.34. Summary of XRD results for lead-tellurite variation study glasses. The details of these phases can be found in Table 4.17.

Table 4.17. Summary of crystalline compounds identified in lead-tellurite glasses with XRD.

Compound	PDF#	ICSD#	SG (SG#)	Reference
KCl	75-0296	28938	*Fm*-3*m* (225)	(Barrett and Wallace, 1954)
NaCl	75-0306	28948	*Fm*-3*m* (225)	(Barrett and Wallace, 1954)
$CsPbCl_3$	75-0408	29067	*Pm*-3*m* (221)	(Moller, 1957)
K_2PrCl_5	77-1448	48190	*Pnma* (62)	(Meyer et al., 1985)
$NaClO_3$	74-0991	26684	*P*213 (198)	(Zachariasen, 1929)
Ba_4OCl_6	72-0630	16026	*P*63*mc* (186)	(Frit et al., 1970)
$BaPrO_3$	70-1430	2753	*Pbnm* (62)	(Jacobson et al., 1972)
PbO	72-2102	20362	*Pbcn* (60)	(Zaslavsky et al., 1950)
$Pb_2Te_3O_7$	43-0549	N/A	*Fm*-3*m* (225)	(Kulcu, 1987)

Background curves were fit to the XRD spectra in order to better distinguish fluctuations in the amorphous background and help with determining amorphous hump maxima. The fitted backgrounds from the XRD spectra are plotted in Figure 4.35a to accentuate minor differences in amorphous structure. From this plot, it is apparent that the amorphous structure of the XCl_{20}-loaded glasses is fairly consistent, although different from TPb_0 without the XCl_{20} addition. As seen in Figure 4.35b, the locations of the first and second broad amorphous hump maxima shift consistently with increasing XCl_{20} loading, revealing a systematic shift in the amorphous structure as the waste components modify the glass network.
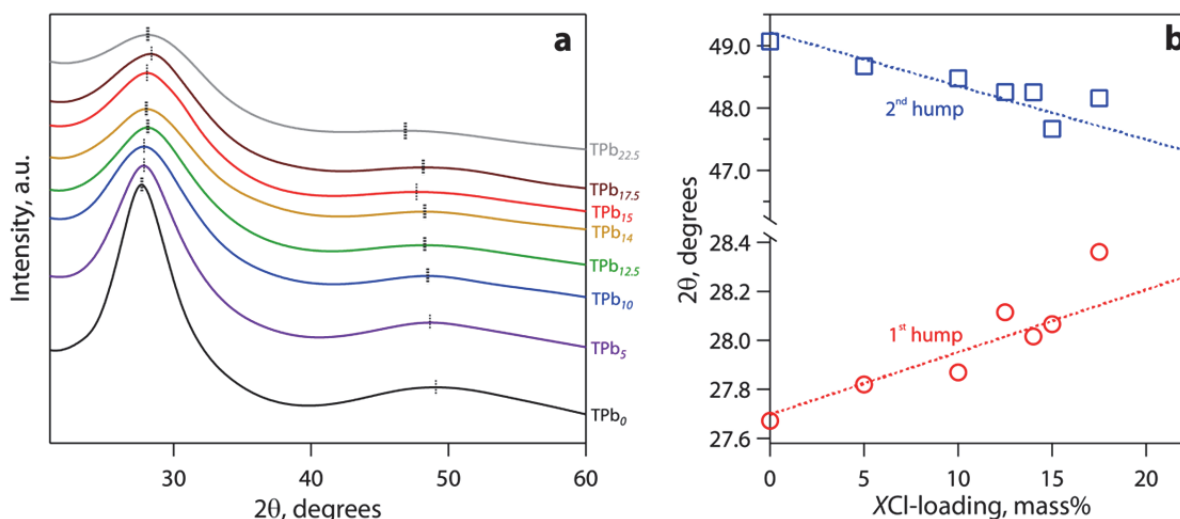
Figure 4.35. (a) Background fits on raw XRD data from the lead-tellurite glasses presented in Figure 4.34. (b) Amorphous hump maxima locations in 2θ—locations denoted by vertical lines in (a)—along with linear data fits for informational purposes only.

4.3.2.5 *Scanning Electron Microscopy and Energy Dispersive Spectroscopy*

After observing the T2G-1-PbO glass in the SEM, it was apparent that the yellow-white phase was actually phase-separated from the bulk glass. This phase-separation was only observed in the top, yellow-white portion of the glass (which cooled slowest during quenching) as dark spherical inclusions—see Figure 4.36. These dark inclusions had a much lower average atomic number than the surrounding matrix as evidenced by the backscattered imaging technique used to collect the micrographs where elements with a higher atomic number appear brighter than elements with a lower average atomic number.

In the yellow-white phase, these inclusions ranged in size from 288±38 nm in diameter towards the top of the yellow-white phase to smaller droplets at 61±10 nm towards the bottom of the yellow-white phase, next to the glassy phase. Very few droplets were observed in the top 5 µm of the yellow-white phase at the very top of the specimen and we believe that this is due to the fact that this surface was cooled by the air during quenching more rapidly than the glass just below the surface. Also the droplets that were found at the top of the specimen were very small (< 60 nm).
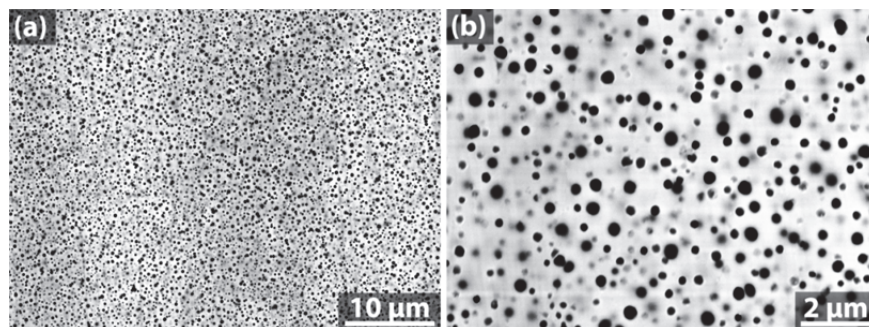
Figure 4.36. Scanning electron microscopy of yellow-white region in T2G-1-PbO showing nano-droplet phase-separation.

EDS area analysis was performed on several of these inclusions in different regions and the compositional results were compared with the results from a series of area scans of the surrounding matrix—see Figure 4.37. From Figure 4.37, it is apparent that the droplets show a higher concentration of the alkali chloride mixture, a higher tellurium concentration, and a lower lanthanum concentration than the surrounding matrix. These results suggest the following:

1) As the XCl_{20}-loading was increased in these glasses, some of the XCl_{20} components were incorporated into the glass (e.g., Ln) while others (e.g., Na, K, and Cl) were excluded from the glassy phase in regions where the cooling rate was not sufficiently high.
2) As the XCl_{20}-loading was increased, the alkali chlorides were not incorporated into the glass as well as the fraction of lanthanide salts.
3) The Ln fractions observed in both the glassy and inclusion phase were significantly higher in the phase-separated fraction of the specimen (>20 mass%) than in the as-batched glass (~8.3 mass%)—see Figure 4.37b. This suggests that the Ln fraction from the lower, glassy region of the specimen was pushed up into the upper phase-separated portion.
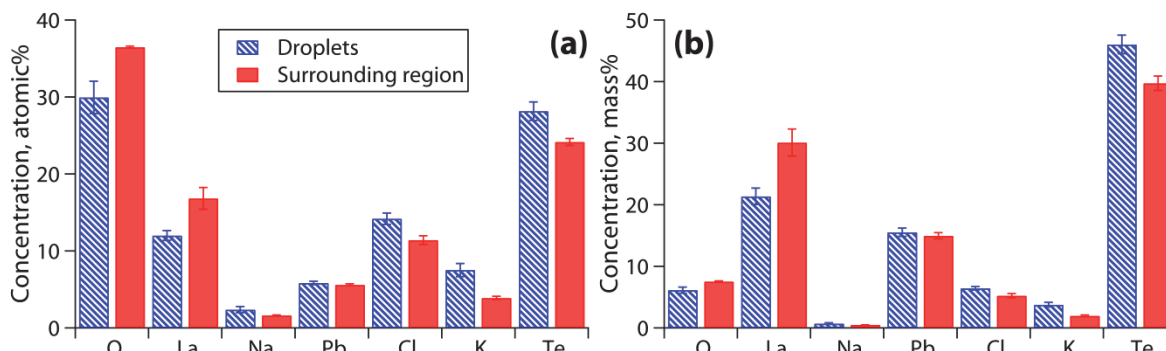
Figure 4.37. Energy dispersive spectroscopy on phase-separated region of T2G-1-PbO where the average composition of the dark droplets in Figure 4.36 is compared to that of the surrounding lighter matrix. The data is presented in both (a) atomic% and (b) mass%. It should be noted that that Li cannot be detected with this technique and is likely present in the droplets along with the other alkali cations. We expect that that the compositional values for the droplets are slightly skewed by the bulk matrix just below the droplets due to electron beam penetration into and interaction with the subsurface matrix.

These results reveal the real reason why the yellow-white phase on the top of T2G-1-PbO is opaque, which is that these phase-separated droplets of alkali halide salt are so small that they cause light-scattering centers, preventing the light to transmit through the specimen in these regions. It is interesting that the alkali chloride phase(s) did not show up on the XRD spectrum for this glass (Figure 4.34), even though they were present in such large quantities considering that these inclusions were found on the top ~40% of the glass in a fairly high density (>15% by volume). We presume that this implies that the alkali halide droplets are amorphous in structure although this has not yet been confirmed.

Figure 4.38 shows the salt phase separation in the higher salt loaded glasses. In the 22.5% glass, large regions were found where salt droplets (perimeter of 22.5% micrograph) coalesced into large pools of molten salt (middle of 22.5% micrograph). The surrounding region can be seen as devoid of droplets but then the droplets appear very small before growing larger in diameter further away from the pool. This phenomenon is typical of crystal growth on cooling depleting the surrounding area of the elements needed for crystal growth. The 30% glass did not have these pools but rather a very high density of droplets all throughout the glass, with varying compositions. The droplets appeared both darker and lighter than the bulk glass. The bright droplets had a higher concentration of Pb, La, and Cl where the darker phase was richer in K and Cl (compared to the surrounding glass).
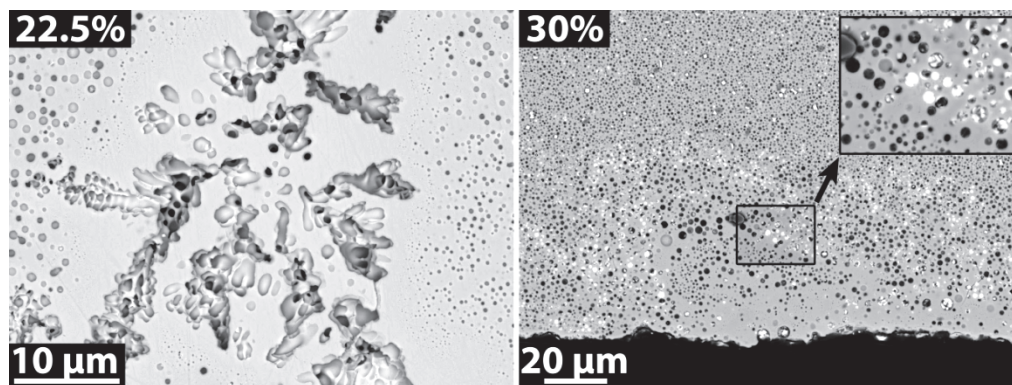
Figure 4.38. SEM micrographs of TPb$_{22.5}$ (left) showing semi-continuous salt phase formation and TPb$_{30}$ (right) showing high density droplets.

4.3.2.6 Transmission Electron Microscopy

Conventional TEM and analytical STEM techniques were performed on the glasses seemingly devoid of phase separation (10 and 14 mass%) to assess whether phase separation was nucleating at lower salt concentrations. At 10 mass% XCl$_{20}$, the glass was observed to be amorphous (diffraction/BF) with no appearance of phase separation (Figure 4.39). Holding the beam on the specimen for extended periods of time induced only slight melting near the edges. At 14 mass% XCl$_{20}$, 10–20 nm rounded contrast features were observed in the glass. Diffraction of these regions suggested that the second phase was not crystalline, but the decreased intensity resulting from use of the 20-µm diameter aperture (to inhibit beam induced phase separation) made it difficult to collect large areas with any appreciable intensity. If the phase-separated regions were indeed poorly crystalline, a larger concentration would be needed to observe diffraction in TEM. When a 50-µm diameter condenser aperture was inserted, beam-induced phase separation was observed as the particles grew slightly (from ~10 to ~18 nm) and increased in concentration. High resolution imaging and diffraction suggested that there was some crystallinity in these phase-separated regions induced by beam damage. Thus it was found that nano-scale phase separation had, in fact, begun with 14 mass% XCl$_{20}$, despite the uniform appearance in visible light and with SEM.
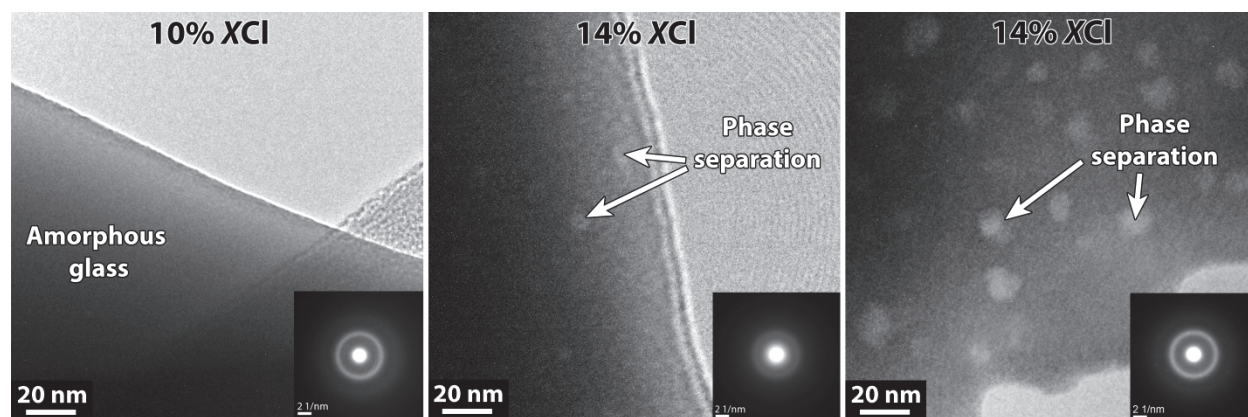
Figure 4.39. TEM micrographs illustrating the evolution of beam-induced phase separation in TeO_2-PbO- XCl_{20} glasses (10%, 14%). The 10 mass% XCl_{20} specimen is completely amorphous. The 14 mass% XCl_{20} has phase separated regions ~10 nm in diameter. Using a larger condenser aperture to image the specimen, beam-induced phase separation occurs (higher density of phase-separated regions which are slightly larger, ~18 nm).

When the XCl_{20} loading increased above the phase separation region, crystalline phases became evident (Figure 4.40). At 17.5% XCl_{20}-loading, a high concentration of large (30–60 nm) diameter phase separation was observed as crystalline material. At higher XCl_{20}-loading (22.5%), the phase separation was observed as 300–400 nm diameter pockets with a lower concentration than the 17.5% loading. With EDS analysis, the composition of the amorphous regions and the phase separated regions with varying contrast were examined. The darker of the four particles were observed to be high in Pb and contained Cs. The lighter of the four phase separated regions contained no Cs and had lower Pb but higher Cl content than the darker regions. Due to charging and the shape of the glass particles, selected area diffraction was not attempted on these regions.
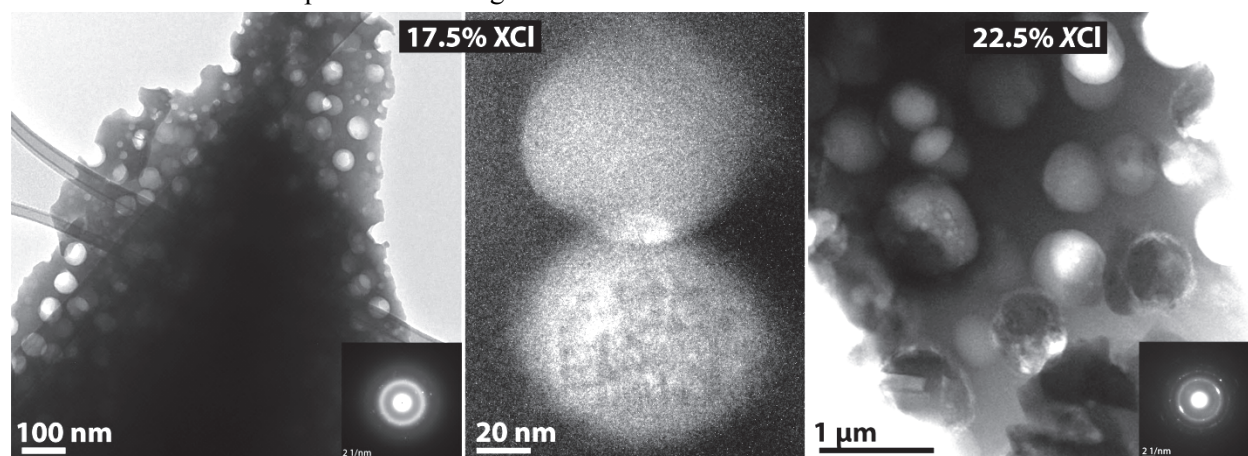
Figure 4.40. TEM micrographs showing phase separation and crystallization in TeO_2-PbO-XCl glasses (17, 22.5%). At 17.5% XCl_{20} loading, full phase separation is observed, with phase separation on the order of 30–60 nm in diameter. At 22.5% XCl_{20} loading, the phase separation is observed to be on the order of 300–400 nm in diameter.

4.3.2.7 *Thermogravimetric Analysis*

Thermogravimetric analysis (TGA) of the lead-tellurite glasses showed that a small mass loss occurred during heating up to ~600 °C (<1 mass%) with an increasing mass loss at $T > 600$ °C (<6 mass%) where the glasses began to melt (Figure 4.41a). It is worth noting that the cumulative mass loss up to the heat-

treatment temperature of 735 °C increased in a consistent manner up to 14 mass% XCl_{20}-loading, where it then plateaued (Figure 4.41b). This suggests that the XCl_{20} components, in addition to the maximum waste-loading (14 mass%), are probably retained in the glass as inclusions during cooling from liquid-liquid phase separation, as evidenced by SEM analysis (Figure 4.36), and not evolved.
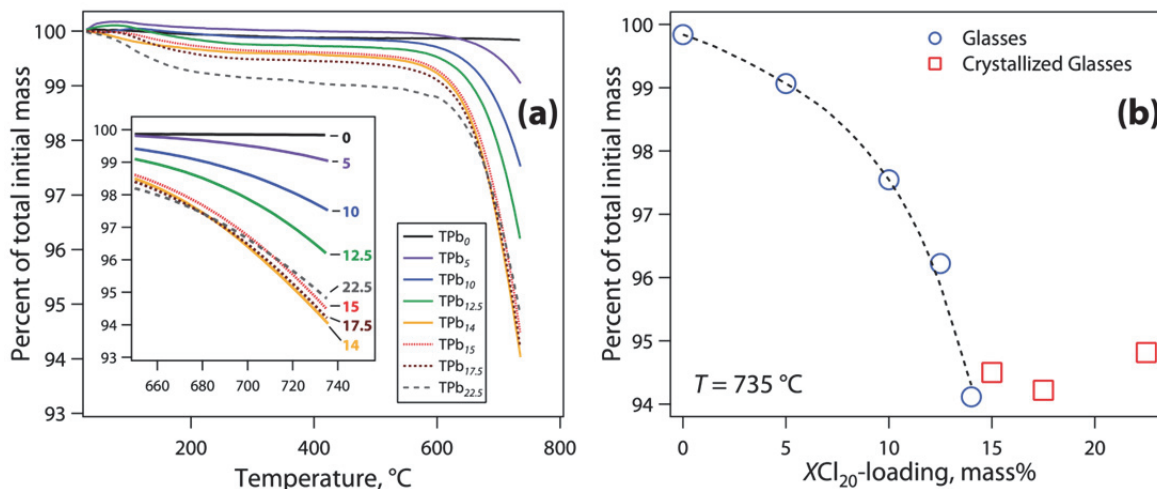
Figure 4.41. Summary of the TGA results for the lead-tellurite glasses. Figure (a) shows the thermogravimetric loss as a function of temperature; the inset shows a magnified view of the high-temperature end of the plot. (b) Cumulative mass retention at 735 °C for all of the glasses.

The DSC results on the lead-tellurite glasses were interesting. We had difficulty setting up the instrument with a good baseline, especially at temperatures above 500 °C. Thus, the data collected in that temperature range was not displayed in Figure 4.42a. Glass TPb_0 had a distinct glass transition temperature (T_g) and two distinct exothermic events denoted by upward peaks of crystallization, $T_{c(1)}$ at the lower temperature and $T_{c(2)}$ at the higher temperature.

Table 4.18. Summary of the DSC results for the lead-tellurite glasses. Variable headings are defined in the paragraph above.

Glass ID	Alternative ID	T_g, °C	$T_{c(1)}$, °C	$T_{c(2)}$, °C	T_M, °C
TPb_0	T2G-21	263.6	308.9	355.9	527.7
TPb_5	T2G-22	278.5	-	383.2	-
TPb_{10}	T2G-23	258.6	-	382.5	-
$TPb_{12.5}$	T2G-24	246.1	348.6	379.3	-
TPb_{14}	T2G-31	220.3	267.7	397.1	-
TPb_{15}	T2G-26	244.2	290.5	381.9	-
$TPb_{17.5}$	T2G-25	228.0	283.5	373.1	-
$TPb_{22.5}$	T2G-30	220.7	292.1	373.7	-
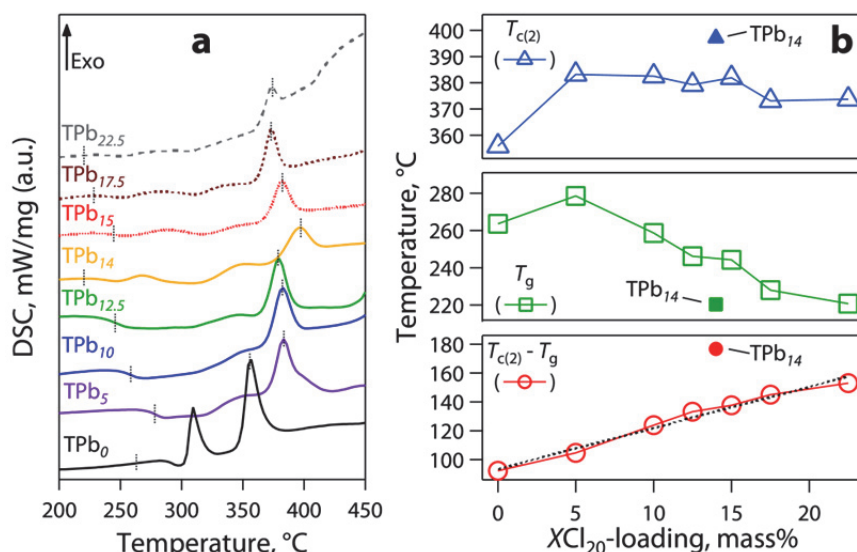
Figure 4.42. DSC results for the lead-tellurite glasses. Figure (a) shows the heat-flow curves as a function of temperature where the calculated T_g and $T_{c(2)}$ are marked with vertical lines. Figure (b), plotted from the data in Table 4.18, shows the trends for $T_{c(2)}$ (top), T_g (middle), and $T_{c(2)} - T_g$ (bottom); TPb_{14} did not fit well on any of the plots so it is denoted by solid symbols on each trend.

As the XCl_{20} was added to the TPb_0 composition, the T_g shifted (both to higher and lower temperatures) the $T_{c(1)}$ peak became buried in the noise, and the distance between the T_g and $T_{c(2)}$ became larger and larger (Figure 4.42b), suggesting a greater glass formation ability—see Equation (9).

These data revealed a few things that were occurring in the glasses during heating:

1) The thermogravimetric mass loss during heating was very low at $T \leq 600\ °C$ (<1 mass%) but increased at $T > 600\ °C$ (≤6 mass%) where the glasses melted. Since all of these glasses were melted at the same temperature of 700 °C, which is not likely to be the ideal temperature for all of them, this volatility could be reduced by melting the glasses at their ideal melting temperatures.
2) The total mass loss as a function of XCl_{20}-loading increased to the glass that had the maximum loading without phase separation (TPb_{14}) where it then plateaued. This suggests that the glass was stabilized by the added waste components at a waste loading above 14 mass% XCl_{20}-loading.
3) Glassy phase(s) present seem to be stabilized by greater additions of the XCl_{20} components according to Figure 4.42b as evidenced by a greater K_{gl} as XCl_{20}-loading was increased. However, it is difficult to feel confident with this assessment after considering the phase-separation observed with the SEM in the glasses with ≥15 mass% XCl_{20}-loading (Figure 4.36).

4.3.2.8 Nuclear Magnetic Resonance

Spectra of ^{125}Te NMR are often difficult to interpret, since ^{125}Te is a spin $I = 1/2$ nucleus with a large gyromagnetic ratio (-8.5×10^{-7} rad/(T·s)) and a long spin-lattice relaxation time, resulting in a large chemical shift range of several thousands of ppm (Edwards et al., 2011). The relaxation time can be shortened if Fe_2O_3 is added to the samples, but this was not done for the current study (Sakida et al., 1999a; Sakida et al., 1999c). Experimental data was simulated to extract the isotropic chemical shift (δ_{iso}), chemical shift anisotropy ($\Delta\delta$), and asymmetry parameter (η). Disorder on the various NMR parameters was simulated to match the experimental data. It was found that providing ±100 ppm Gaussian disorder in δ_{iso} provided the necessary smoothing to match the experimental data, while providing disorder in $\Delta\delta$ (±100 ppm) or η (±0.1) had little effect. All subsequent simulations were performed with this δ_{iso} disordering. All spectra could be fit with two Te sites, while one was insufficient and three did not significantly improve the fits. Figure 4.43 shows an example of experimental data,

simulation, and deconvolution. A summary of all the NMR data collected for the TeO_2-PbO XCl_{20} series is shown in Figure 4.44.
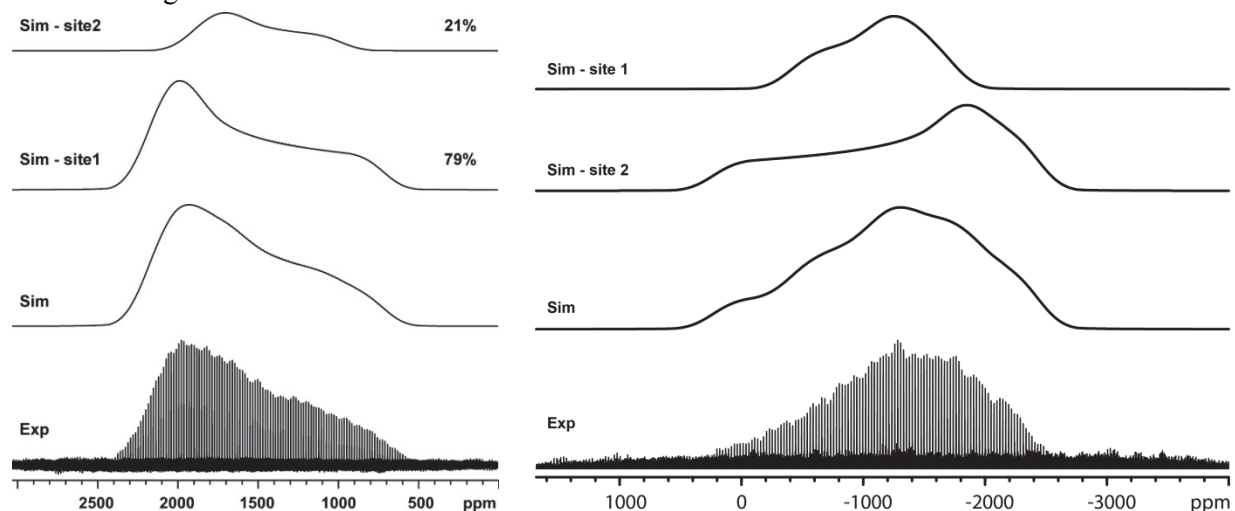
Figure 4.43. (left) ^{125}Te NMR for 10% XCl_{20} glass showing experiment (Exp), simulation (Sim), and site deconvolution. (right) ^{207}Pb NMR results for 15% XCl_{20} glass.
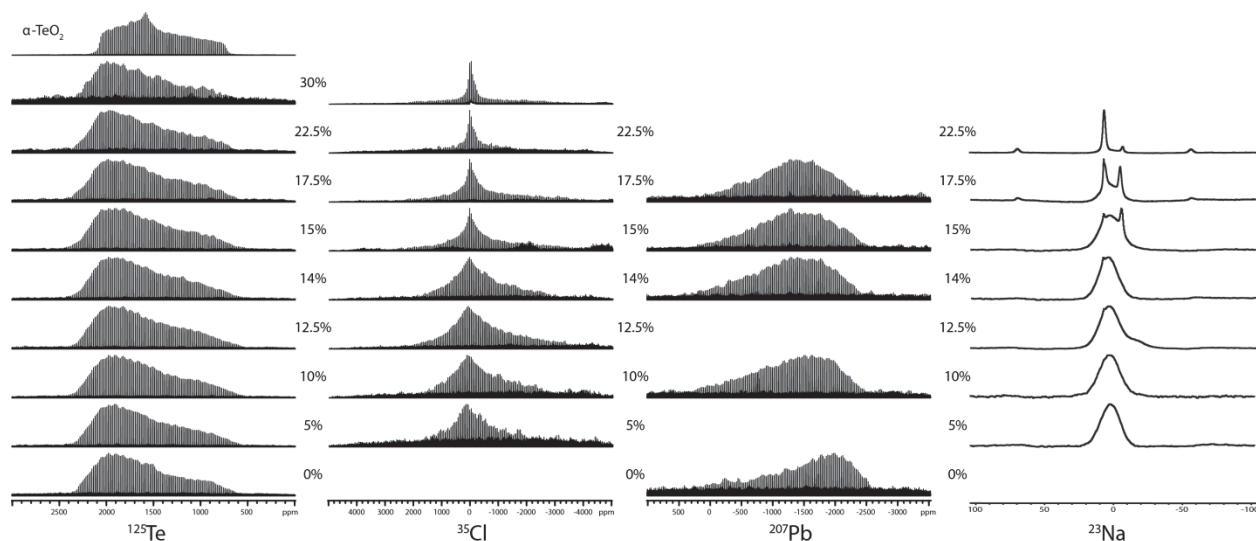
Figure 4.44. Summary of ^{125}Te, ^{35}Cl, ^{207}Pb, and ^{23}Na NMR as a function of waste loading. Spectra are aligned by glasses and the gaps show were data was not collected.

The ^{125}Te fit results of the constant Te/Pb ratio suggest that Te site distribution does not change with the addition of XCl_{20} (see Table 4.19). The fit resulted in one Te site with larger chemical shift (mean 1642 ppm) having the greater area fraction (mean 78.7%), herein assigned to TeO_4. A second site with the smaller chemical shift (mean 1558 ppm) and area fraction (21.3%) was assigned to TeO_3.

For TPb_0, the glass without chlorides, the area fractions were 78% (TeO_4) and 22% (TeO_3); these results are quite similar to results of Sakida et al. (1999b) for glasses in the range of PbO comparable to TPb_0. However, the δ_{iso} and $\Delta\delta$ from our fits contradict the assessment of Sakida et al. In fitting the static ^{125}Te NMR data, Sakida et al. (1) fixed $\Delta\delta$ (-1285 ppm) and η (0.74) based on pure TeO_2 glass and assigned it to TeO_4 *tbp* units, then (2) fit the second site (TeO_3 *tp* units) at the lowest PbO concentration and fixed $\Delta\delta$ (-805 ppm) and η (0.39) for all other glasses in the PbO series. The only adjustable parameters, then,

became δ_{iso} and the fraction of sites. Their resulting δ_{iso} for the TPb$_0$–equivalent glass was δ_{iso}(TeO$_4$) ~1577 ppm and δ_{iso}(TeO$_3$) ~1870 ppm. By contrast, in our fit, the lower chemical shift species with smaller area fraction was assigned to TeO$_3$, so the assignments by area fractions were similar to Sakida et al. but the higher versus lower chemical shifts are reversed.

Table 4.19. ^{125}Te static NMR fit results.

XCl	Site 1 (TeO$_4$)				Site 2 (TeO$_3$)			
Mass%	δ_{iso}	$\Delta\delta$	η	Area%	δ_{iso}	$\Delta\delta$	η	Area%
0	1649	-1364	0.217	78.2	1603	-697	0.330	21.8
5	1647	-1370	0.282	79.1	1540	-843	0.406	20.9
10	1640	-1387	0.259	78.6	1540	-847	0.428	21.4
12.5	1638	-1418	0.270	77.8	1569	-798	0.670	22.2
14	1641	-1425	0.263	77.5	1549	-804	0.426	22.5
15	1641	-1384	0.280	79.6	1556	-829	0.443	20.4
17.5	1636	-1423	0.265	80.8	1538	-854	0.294	19.2
22.5	1643	-1441	0.215	77.9	1568	-816	0.444	22.1
Mean	1642	-1401	0.256	78.7	1558	-812	0.430	21.3
Std. Dev.	4	29	0.026	1.1	22	51	0.112	1.1
14 (high Pb)	1666	-1383	0.183	71.8	1663	-792	0.446	28.2
5 (XO)	1650	-1369	0.257	80.0	1599	-714	0.443	20.0

These discrepancies between our results and that of Sakida et al. (Sakida et al., 1999b) warrant further comment. Unlike those in Sakida et al., the methods used in the current study did not fix $\Delta\delta$ or η for either of the Te sites but rather allowed all parameters to vary. In a different study, Sakida et al. (Sakida et al., 1999a) also modeled a large number of Te-containing crystals, and assigned the Te structure based on a diagram of $\Delta\delta$ versus η, later applying this to glass as well (Sakida et al., 1999c). Recently, Holland et al. have observed that Sakida's model did not work for their Na$_2$O-TeO$_2$ crystallized glasses studied with ^{23}Na and ^{125}Te NMR, suggesting that caution is advised in comparing glass spectra to crystalline line shapes and inferring local structures (Holland et al., 2005). Likewise, our data for the TeO$_4$ site ($|\Delta\delta| = 1401$, $\eta = 0.26$) does not fit in one of Sakida's regions, but rather near some of the data from Holland et al.; on the other hand, our TeO$_3$ site ($|\Delta\delta| = 811$, $\eta = 0.43$) does fit in Sakida's "terminal TeO$_3$" region similar to other glasses (Sakida et al., 1999c).

The lack of change of the Te site distribution with increasing metal chloride addition contradicts commonly held assumptions about the effects of M$^+$, M^{2+} and M^{3+} cations on the structure of TeO$_2$ glasses in the following way (Heo et al., 1992; Sakida et al., 1999a; Sakida et al., 2001, 1999c; Sekiya et al., 1994b; Sekiya et al., 1992; Sekiya et al., 1995). In previous FTIR, Raman, and NMR studies where M$^+$, M^{2+} and M^{3+} oxides are added to TeO$_2$, increasing amounts of these oxides added to TeO$_2$ glass are found to increase the TeO$_3$ fraction of sites at the expense of TeO$_4$ sites. In the case of the TeO$_2$-PbO-XCl glasses, on the other hand, the Te site distribution is not changed by the addition or subtraction of cations and anions.

To test whether the Te:Pb ratio was controlling the Te speciation, a new "high Pb" glass (TG12-02) with a Te:Pb ratio of 3.0 was prepared and analyzed. The ^{125}Te fitted spectrum showed that the Te speciation changed slightly (but measurably) from other samples, with a noticeably higher TeO$_3$ fraction (28.2% for high Pb versus 21.3% average for other samples). This glass showed that $\Delta\delta$ was within the range of the other glasses, but η, δ_{iso}, and area fractions were clearly different. This sample should be compared directly with the 14% XCl$_{20}$ glass. Additionally, the all-oxide XO glass, which should be compared with the 5% XCl$_{20}$ glass, appears distinguishable from the chloride glasses, with site 2 (TeO$_3$) $\Delta\delta$ and δ_{iso} being slightly different, closer to the 0% XCl$_{20}$ than the 5% XCl$_{20}$, but otherwise within the range of the XCl$_{20}$ glasses.

To further understand this behavior, [207]Pb NMR spectra were collected on a subset of samples. The [207]Pb NMR spectra consist of broad lineshapes ~3000 ppm wide which can be deconvoluted into two Pb sites, as shown for example in Figure 4.43. Both sites have negative chemical shifts, characteristic of ionically bonded Pb compounds (Fayon et al., 1997). Ionically bonded $PbCl_2$ has a δ_{iso} of -1717 ppm and a Pb coordination number of seven, while covalently bonded PbO has a δ_{iso} of 1939 ppm (red tetragonal litharge) or 1515 ppm (yellow orthorhombic massicot) and coordination number of four (Fayon et al., 1997). Contrary to the results for the Te-Pb-O- X-Cl glasses here, Cd-Pb-O-Cl glasses show a mixed bonding character for Pb in NMR, with a peak characteristic of covalent Pb-O (positive chemical shift) and one of ionic Pb–Cl (negative chemical shift) (Montagne et al., 2001). Empirical correlations between δ_{iso}, coordination number around lead, and Pb–O bond distance suggest that the two sites in our Te-Pb-O-X-Cl glass likely represent 5- and 6-coordinated Pb with Pb–O distance of 0.252–0.257 nm (Fayon et al., 1997). Note that two sites were present even in the glass without chlorides. Bond lengths and coordination for the TeO_2 glasses suggest that some PbO_aCl_b octahedra exist, similar to crystal forms of Pb-O-Cl such as mendipite ($Pb_3O_2Cl_2$) (Lezal et al., 2002; Montagne et al., 2001; Porter and Halasyamani, 2003). In mendipite, Pb atoms are 6- or 7-coordinated with the first Pb coordination sphere containing oxygen at Pb–O ~0.23 nm and chlorine at Pb–Cl ~0.31 nm (Montagne et al., 2001).

The relative fraction of the two Pb sites changes monotonically with XCl$_{20}$ addition (Table 4.20) with a noticeable jog in the trend between 14% and 15% XCl$_{20}$, the same region of the phase separation. The ~11% fraction of Pb site 1 (δ_{iso} = -1371 ppm at XCl$_{20}$ = 0) increases to ~40% fraction at the highest chloride loading measured (δ_{iso} = -1168 ppm at XCl$_{20}$ = 17.5%), with a complementary decrease of the Pb site 2 (δ_{iso} = -1402 ppm at XCl$_{20}$ = 0) (see Figure 4.45). This result, combined with the lack of change in the [125]Te NMR, indicates that the addition of the alkali, alkaline earth, and lanthanide chlorides primarily effects the Pb environment and not the Te environment.

Table 4.20. [207]Pb static NMR fit results.

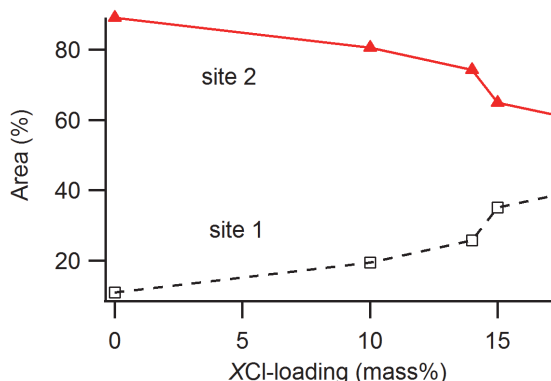| XCl$_{20}$ (mass%)	Site 1				Site 2			
	δ_{iso}	$\Delta\delta$	η	Area%	δ_{iso}	$\Delta\delta$	η	Area%
0	-1371	1015	0.438	10.9	-1402	2555	0.321	89.1
10	-1082	1059	0.604	19.4	-1240	2526	0.361	80.6
14	-1059	1085	0.670	25.7	-1272	2352	0.416	74.3
15	-1129	1101	0.677	35.1	-1350	2384	0.382	64.9
17.5	-1168	1150	0.850	39.0	-1316	2358	0.453	61.0
14 (high Pb)	-906	2649	0.925	26.2	-1157	2088	0.530	73.8

Figure 4.45. Variation of Pb site distribution with XCl$_{20}$-loading.

From the [23]Na data in Figure 4.44, it is apparent that there is one disordered Na site at the 5, 10, and 12.5 mass% XCl$_{20}$ level, with a possible shoulder ~-16 ppm in the latter glass. At 14 mass%, the threshold

phase separation, a peak is present at 7 ppm that becomes very prominent in loadings ≥15 mass%. Additionally, a peak at ~-6 ppm becomes apparent at ≥15 mass%, potentially shifting ±1 ppm up to the highest level of 22.5 mass%. The peak at 7 ppm is tentatively identified as NaCl, and that at -6 ppm as NaClO$_4$. The trend in line shape clearly shows the appearance of sharp, crystalline peaks related to Na phases beginning ~14 mass% XCl$_{20}$ loading.

The ^{35}Cl data shown in Figure 4.44, suggests a similar behavior to the ^{23}Na. A broad distribution of chemical shift is evident from 5–14 mass% XCl$_{20}$, centered ~-8 ppm. In the 15–30 mass% XCl$_{20}$ range, the distribution of chemical shift narrows considerably, again suggesting that chlorine is occupying a narrower range of sites. Taken together with the ^{23}Na data, the ^{35}Cl data indicates that crystalline, or at least highly ordered, chlorine sites are increasingly present as XCl$_{20}$ is increased above 14 mass%.

4.4 Tellurite Glasses – Overview

No studies of tellurite glasses exist in the literature with the complexity of constituents as considered here, including both a modifier (and co-glass former) like PbO and multiple alkali, alkaline earth, and lanthanide chlorides. Therefore, comparison must be made to simpler systems to gain corroboratory insight into the glass structure change with composition.

Several studies have investigated binary compositions of metal chlorides with TeO$_2$. Notably, neutron diffraction experiments of TeO$_2$ with up to 35 mol% BiCl$_3$ (Neov et al., 1990) or 20 mol% CsCl, MnCl$_2$, FeCl$_2$, or FeCl$_3$ (Neov et al., 1995) noted no change in the tellurite structural configuration from 4-coordination, suggesting that the chlorides exist quasi-independently of the tellurite network and do not participate in *tbp* network breaking. In other words, the salt exists as an independent phase-separated entity on the local level. Very few studies exist in the literature on tellurite glasses with oxide modifiers in addition to halide modifiers. Recently, Solokov et al. studied TeO$_2$-BaO-BaCl$_2$ systems, both experimentally and computationally, and concluded that the barium and chlorine were present as free ions in the interstices of the tellurite matrix, as Ba^{2+} and Cl$^-$ (Sokolov et al., 2009). In comparing the effects of BaO with BaCl$_2$ using *ab inito* molecular dynamics simulations, the authors state that each Ba atom, when added as an oxide, forms two N_4^- species and one N_3^- species, whereas when it is added as a chloride, it forms three N_3^- species. In both cases, this indicates a depolymerization of the N_4^0 tellurite network.

These two examples illustrate the two models usually offered for structure of halide-containing oxide glass systems (Chowdari et al., 1998). In the first case with TeO$_2$ + chlorides (Neov et al., 1995; Neov et al., 1990), the salt phase can be understood as being composed of clusters in the interstices of the host oxide glass which do not modify the glass structure. Alternatively, the glass structure may change systematically with the halide salt dopant, as is the case in TeO$_2$-BaO-BaCl$_2$ (Sokolov et al., 2009) and TeO$_2$-PbF$_2$ (Kabalcı et al., 2009). Similarly, a TeO$_2$-CuI-Cu$_2$O glass was observed to phase separate, causing difficulty in interpretation of glass transition and crystallization processes (Chowdari et al., 2000). These authors reported 60–920 nm phase-separation in the form of droplets and clusters where the size was composition-dependent.

In the case of the TeO$_2$-PbO-XCl system studied here, interpreting the Raman data alone suggests that the increase of the XCl$_{20}$ mixed salt dopant resulted in a progressive depolymerization of the glass network up to the point of ~14 mass% XCl$_{20}$. However, ^{125}Te NMR showed no change in the site distribution of Te, rather suggesting that the polymerization of the glass network was fixed by the Te:Pb ratio, which remained constant. An alternative interpretation of the Raman data is that the local vibrational modes for *tp* and *tbp* change as a function of composition due to the near-presence of increasing amounts of alkali metals and chlorine. The ^{23}Na and ^{35}Cl NMR show a broad distribution of Na sites up to 14 mass%, indicating that Na and Cl are present in the glass structure in a variety of sites. The Raman vibrations of the tellurite units could change as a function of composition due to these additional ions, even if the site distribution of Te sites is not effected. A small peak in the ^{23}Na NMR at 14 mass% seems to correlate with the low concentration of crystalline or weakly crystalline inclusions seen in TEM in this specimen.

Above 14 mass% XCl_{20}, SEM, TEM, XRD, and ^{23}Na and [35]Cl NMR all support the progressive formation of crystalline salt phases. Sharp peaks in [23]Na suggest multiple crystalline Na phases are present, and the [35]Cl spectrum progressively narrows. It is unclear whether the mechanism is phase separation in the melt followed by crystallization, or crystallization out of the melt. At the highest salt doping level of 22.5 mass%, the mole fraction of the TeO_2 is roughly equal to that of XCl_{20}, and a partially percolated network of the salt is realized. Up to the solubility of the mixed salt phase in the glass (~15 mass% XCl_{20}), the salt systematically changes the tellurite glass structure by incorporating Cl, Na, and probably other cations, but does not affect the Te site distribution. Above this solubility, the excess salt no longer systematically affects the local environment (and hence vibrational states) of the glass network but phase separates and crystallizes, and the glass vibrational structure remains essentially as it was at the 15 mass% XCl_{20} level. The remaining salt phase can be thought of as being distributed in the interstices of the glass network.

The role of the Pb in this glass system should not be discounted, especially since it appears that the Pb determines the Te site distribution. Additionally, the [207]Pb NMR shows that the distribution of the two Pb sites changes significantly with the addition of mixed salt, favoring site 1 (more negative chemical shift, hence more ionic) at higher loadings. Lead also helps to polymerize the network (probably as PbO_aCl_b octahedra), keeping the glass network continuous when it might otherwise be completely broken. One can envision Te–Cl bonds (Lezal et al., 2002), particularly Te–Cl$_{eq}$ that may strengthen Te–O$_{ax}$ and prevent some *tp* formation (Tanaka et al., 1988b), Pb–Cl bonds (at least in the compositions with less XCl_{20}), and Te–O–Pb bonds (Silva et al., 2001). Given their size (see Table 2.2), the lanthanides are likely in interstices in the tellurite or lead networks (Nachimuthu and Jagannathan, 1995), but recent results on TeO_2-PbO-Eu_2O_3 oxide glasses indicate that Eu, at significant concentrations, can favor the creation of PbO_4 units in tellurite glass (Rada et al., 2011).

It is likely that the combination of highly polarizable Te and Pb allow for large salt concentrations. Both Te^{4+} and Pb^{2+} have a lone pair of electrons that result in a highly polar asymmetry and, in some Te-Pb-O-Cl crystals, the lone pairs point toward the chlorine atoms in the structure to minimize electrostatic effects (Porter and Halasyamani, 2003). A comparison of glasses with the same cation molar concentrations but without Cl (e.g., T2G-34 vs. T2G-22), suggests that *tbp*/*tp* ratios increase when Cl is substituted for O, indicating that Cl-containing glasses are relatively more polymerized than their oxygen counterparts. This could be due to the scavenging effects of Cl on alkalis, preventing the incorporation of some Na and Li into the glass. This appears to be due to an ionic component of charge compensation.

Previous results with the 10 mass% XCl_{20} loading showed very high chemical durability for the TeO_2-PbO-XCl glasses compared to other candidates (Riley et al., 2010; Riley et al., 2012b). This effort was focused on determining the maximum XCl_{20}-loading for this particular glass system. It appears that the TeO_2-PbO-XCl system with 14 mass% XCl_{20} is a highly metastable system, with energy from an electron microscope being sufficient to induce phase separation and crystallization. This suggests that 14 mass% XCl_{20}-loading is the upper limit for use as a waste form with this particular laboratory quenching method and batch size. It may be that waste forms processed at a larger scale, resulting in slower cooling in some portions, would result in faster crystallization and thus lower loading limit (based on phase separation). Additionally, it is noteworthy that the actual chloride stream will contain some radioactivity that will add energy to the system, thus potentially promoting phase separation and crystallization. It is presumed that the chemical durability of the phase separated and crystallized glass would be lower than uncrystallized glass because of the water-soluble, salt-rich phases observed here as found in other systems (Rodriguez et al., 2011), but this has not been verified for the TeO_2-PbO-XCl system.

4.5 Polycrystalline Tellurite Compounds as Standards

In FY2011, five tellurite crystals were fabricated and included: $ZnTeO_3$, $Zn_2Te_3O_8$, $SnTe_3O_8$, $ZrTe_3O_8$, and $TiTe_3O_8$. The procedures used to fabricate these samples were first attempted with those laid out in Table 3.12, but modifications were made in some cases. Pictures of these crystals are presented in Figure 4.46. It was difficult to achieve 100% of the target phases in all cases without at least minor impurities

from unincorporated reactants with the exception of $ZnTeO_3$. A summary of the crystalline phases found in these samples during XRD analysis is presented in Table 4.21.
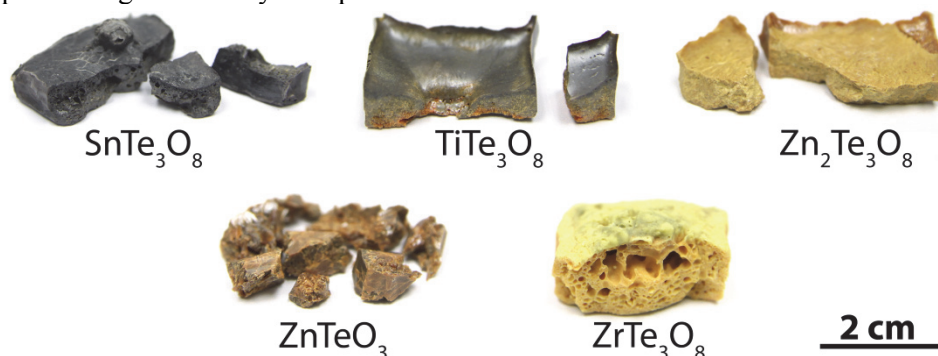
Figure 4.46. Pictures of the tellurite crystals fabricated in FY2011. The scale-bar is the same for all micrographs.

Table 4.21. Summary of crystalline phases identified in tellurite crystals.

Phase	PDF#	ICSD#	SG (SG#)	Reference
$SnTe_3O_8$	70-2440	9077	*Ia*-3 (206)	(Meunier and Galy, 1971)
$TiTe_3O_8$	70-2439	9076	*Ia*-3 (206)	(Meunier and Galy, 1971)
$ZnTeO_3$	44-0240	N/A	*Pbca* (61)	[a]
$ZnTeO_3$	72-1410	16937	*Pbca* (61)	(Hanke, 1967)
$Zn_2Te_3O_8$	89-4454	50705	*C2/c* (15)	(Feger et al., 1999)
$ZrTe_3O_8$	70-2442	9079	*Ia*-3 (206)	(Meunier and Galy, 1971)
SnO_2	70-6153	91517	*P42/mnm* (136)	(Kim et al., 2000)
SnO_2	41-1445	N/A	*P42/mnm* (136)	(McCarthy and Welton, 1989)
α-TeO_2	42-1365	27515	*P41212* (92)	[b]
α-TeO_2	74-0269	25706	*P41212* (92)	(Leciejewicz, 1961)
TiO_2	70-7347	93097	*P42/mnm* (136)	(Ballirano and Caminiti, 2001)
ZrO_2	89-9069	89429	*Fm*-3*m* (225)	(Wang et al., 1999)

[a]Rosenstingl, J., CH Hoffmann, E Irran, CH Lengauer, E Tillmanns, Vienna, Austria. ICDD Grant-in-Aid (1992)

[b] Information given in PDF card: Blanchard, F., Department of Geology, University of Florida, Gainesville (1990).

4.5.1 TeO$_3$-Isolated Crystals

The only crystal in this category that was made successfully was the $ZnTeO_3$ crystal, which we made as phase-pure because all of the diffraction peaks fit well to the ICSD standard in the database. The XRD pattern is presented in Figure 4.47. This sample seemed to be the most brittle of the five that we made.
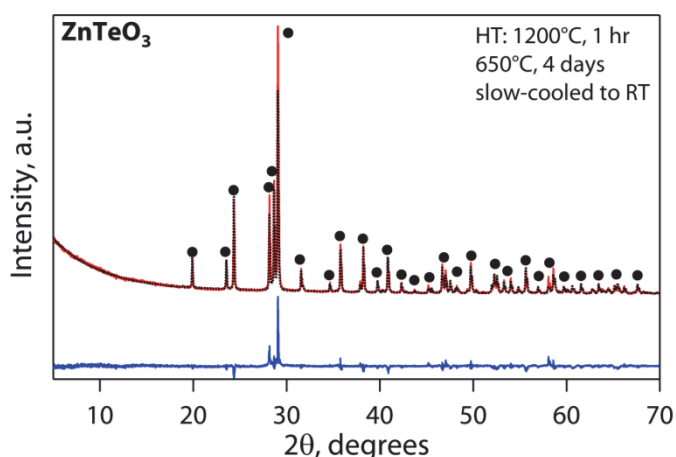
Figure 4.47. Rietveld refinement on $ZnTeO_3$ crystals showing the measured, calculated, and difference spectra. Here, ● represents the target phase ($ZnTeO_3$, PDF#72-1410, Table 4.21).

4.5.2 TeO$_3$-Terminal Crystals

The only crystal that was attempted in the class of TeO_3-terminal crystals was $Zn_2Te_3O_8$; this was achieved at high purity levels with minor impurities of what appeared to be the $ZnTeO_3$ phase. The Rietveld refinement of this pattern is presented in Figure 4.49.
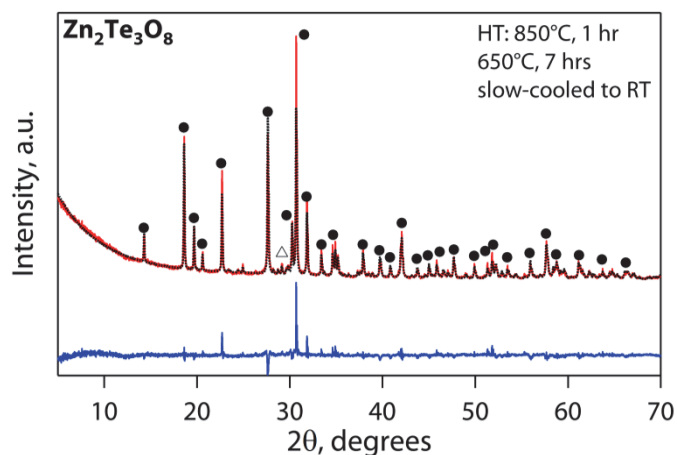
Figure 4.48. Rietveld refinement on $Zn_2Te_3O_8$ crystals showing the measured, calculated, and difference spectra. Here, ● represents the target phase ($Zn_2Te_3O_8$, PDF#89-4454) at 97.08 mass% and △ represents a minor impurity phase, $ZnTeO_3$ (PDF#75-1410) at 2.92 mass% (Table 4.21).

4.5.3 α-TeO$_2$ Tellurite Crystals

Three phases in this class of materials were investigated in FY2011: $ZrTe_3O_8$, $SnTe_3O_8$, and $TiTe_3O_8$. $SnTe_3O_8$ and $TiTe_3O_8$ were both heat-treated at 650 °C for several days and did not melt, although they did result in relatively pure materials of the target compounds. However, the target goal was to melt the mixtures and fire them to both achieve phase-pure materials of the target composition and have particles large enough to size for chemical durability tests if they are sieved to isolate the larger particle sizes. Thus, high-temperature ($T > 900$ °C) soaks were attempted prior to the lower temperature heat treatment for a long duration. These heat treatments did not always have the desired results; in some cases heat treatment at these higher temperatures resulted in a decrease of the target phase. For the $SnTe_3O_8$ and $TiTe_3O_8$ samples, the Rietveld refinements of the XRD data are presented in Figure 4.49.
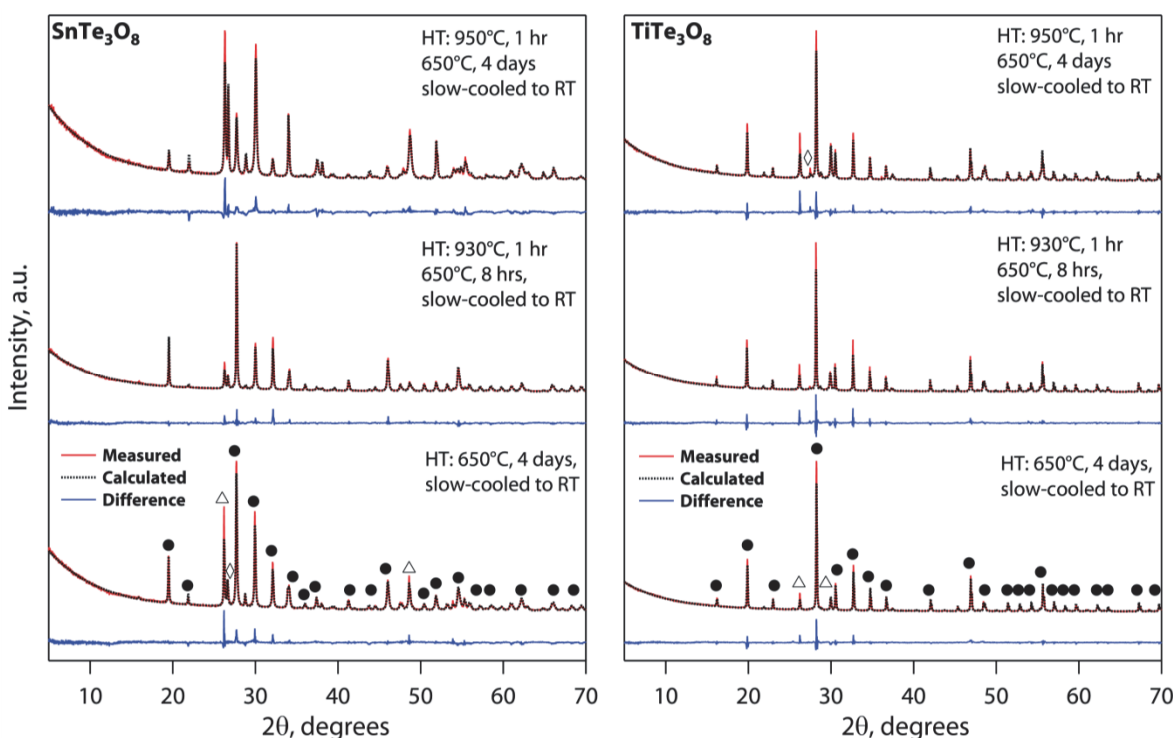
Figure 4.49. Rietveld refinement of XRD spectra for the $SnTe_3O_8$ (left) and $TiTe_3O_8$ (right) samples after various heat treatments. The samples were run sequentially from the bottom spectra toward the top spectra. Here, ● represents the target phases of $SnTe_3O_8$ (PDF#70-2440) and $TiTe_3O_8$ (PDF#70-2439), △ represents α-TeO_2 (PDF#42-1365), and ◇ represents the metal oxides of SnO_2 (PDF#70-6153) and TiO_2 (PDF#70-7347) in the corresponding figures (right and left, respectively) (see Table 4.21). The quantities of the constituents of these samples after each heat treatment are presented in Table 4.22.

Table 4.22. Mass% of components in $SnTe_3O_8$ and $TiTe_3O_8$ samples after Rietveld refinements. The phases correspond to phases in Table 4.21 with graphical representations in Figure 4.49. The temperatures correspond to the heat treatment temperatures.

Components	$SnTe_3O_8$			$TiTe_3O_8$		
	650 °C	930 °C	950 °C	650 °C	930 °C	950 °C
$SnTe_3O_8$	56.83	75.32	23.84	-	-	-
SnO_2	11.41	6.59	20.12	-	-	-
TeO_2	31.76	18.09	56.04	10.07	17.33	23.1
$TiTe_3O_8$	-	-	-	84.95	73.46	69.38
TiO_2	-	-	-	4.98	9.21	7.52

For the $ZrTe_3O_8$ sample, the single heat treatment at 950 °C resulted in a very highly pure sample with only minor impurities of the unincorporated reactants. The Rietveld refinement of that sample is presented in Figure 4.50.
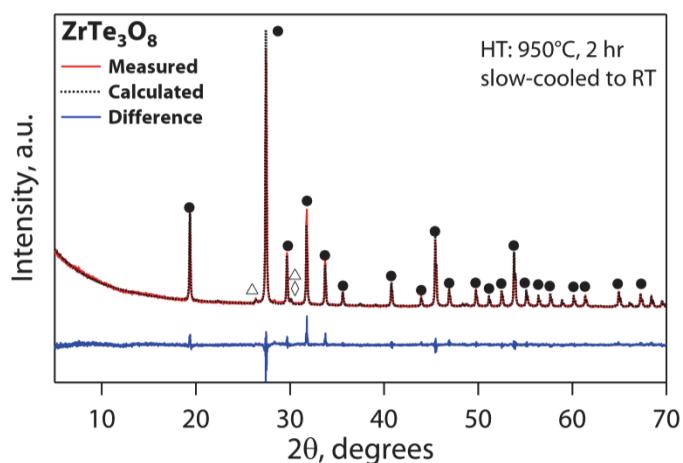
Figure 4.50. Rietveld refinement of XRD spectra for $ZrTe_3O_8$ after the 950 °C heat treatment. Here, ● represents the target phase ($ZrTe_3O_8$, PDF#70-2442), △ represents α-TeO_2 (PDF#42-1365), and ◇ represents ZrO_2 (PDF#89-9069). Here, the $ZrTe_3O_8$ phase represents 97.21 mass% and TeO_2 represents 2.79 mass% of the crystalline content.

According to the results this far, it is apparent that it is possible to fabricate melted solids of highly pure tellurite crystals that can be used for chemical durability testing. This was a scoping study to see if it was possible to make solids of these crystals so they could be powdered after achieving phase-pure samples and then sized for chemical durability testing.

5   CONCLUSIONS

5.1 Tellurite Glasses

We performed several concurrent studies with the tellurite glass waste form in FY2011 and FY2012. These studies included the following: 1) structural investigations on the P-series tellurite glasses from FY2010, 2) an expanded study on the lead-tellurite glasses that had high chemical durability in the FY2010 study, 3) a study on a series of glasses designed to reveal the glass-structural effects of anion/cation substitutions into the tellurite glass network, and 4) a study on the chemical durability of tellurite crystals with known crystal structure and tellurium-oxygen coordination.

Study 1 – *Lead-tellurite variation glasses*. A series of TeO_2-PbO glasses were fabricated with various amounts of a mixed chloride waste simulant (nonradioactive) intended to represent the EChem waste stream from the electrochemical process used for processing nuclear fuel. The structure of these glasses was studied by characterization with nuclear magnetic resonance, Raman spectroscopy and X-ray diffraction, and indicated that the medium-range order in the glass decreased and the tellurite network was depolymerized as the waste fraction was increased. It was apparent that glass network-breaking was predominantly caused by the additions of the waste cations and that the presence of chloride may have actually caused some repolymerization of the network by scavenging alkalis and preventing it from acting as a network modifier. Under the processing conditions used in this study, the waste loading limit was determined to be around 14 mass% XCl_{20}, above which phase separation was observed resulting in a Te-rich phase and a alkali-chloride-rich phase, and some chloride-containing crystals.

Study 2 – *Compositional variation glasses*. In this study, which was the ground work for Study 2, we learned the various interpretations of the diverse set of Raman spectra observed in tellurite glasses. We measured the Raman spectra for all 10 of the P-series glasses that were analyzed with the PCT. The primary goal of the structural interrogation of the P-series glasses was to see whether we could find a correlation between the tellurium-oxygen coordination environment and the chemical durability, considering that the chemical durability of these glasses was so diverse. However, we failed to find a simple correlation.

Study 3 – *Structural variation glasses*. A series of glasses were designed to investigate the glass structural effects when select species in the glasses from Study 1 and Study 2 were substituted for other species. The aim of these studies was to better understand the difference between the roles of the cations and anions from both the lead and the XCl_{20} components. We looked at (1) lead-tellurite glasses with K_2O or KCl, (2) a lead-tellurite glass in which XCl_{20} components were substituted for XO_{20} components ("X" cation ratios to Te and Pb retained from the TPb_5 glass), and (3) some lead-tellurite glasses in which $PbCl_2$ was substituted for PbO. Structural analysis on these glasses indicated that the chloride in XCl_{20} actually *repolymerizes* the tellurite network compared to the oxygen in the XO_{20} glass with the same modifier cations, by scavenging some of the alkalis into a separate phase that is ultimately present as nano-phase-separated droplets at the highest XCl_{20}-loadings. This local removal of alkali from the role of network modifier of the tellurite network, even in the low waste loading glasses devoid of visible phase separation, is believed to be the mechanism responsible for preventing formation of some *tp* units indicative of depolymerization. The comparison of the K_2O and KCl glasses having the same relative amount of K compared to Te and Pb indicated the same trend, i.e., that the chloride-containing glass is slightly more polymerized than the one without chloride when both contain the same relative amount of alkali to the main glass formers.

Study 4 – *Polycrystalline tellurite compounds as standards*. A study on tellurite crystals was identified in the literature as a potentially valuable contribution to our work. In this study, a wide range of binary and ternary Te-O crystals were made and categorized into groups in which the structures were composed of either TeO_3, TeO_{3+1}, α-TeO_2, or β-TeO_2 Te-O structural units. The primary goal of pursuing these was to make a few of the crystals in each "category" and test the chemical durability of the crystals. If one of

these structural units is preferred for high chemical durability, then since the crystals are composed of a single structural unit throughout, crystals from certain categories may show better chemical durability than others. We successfully made five crystals, some of them nearly phase-pure.

5.2 Halide Minerals

In order to improve upon our results from past years on solution-derived sodalites, we made some changes to the process in FY2011. These changes included the following: (1) replacing CS with TEOS as the silica source in the process, (2) replacing Si with Ge in the sodalite with germanium (IV) ethoxide, and (3) optimizing the sintering aid for low-temperature firing to reduce chloride volatility and maximize sodalite production.

Study 1 – *Organic silica source*. We replaced the CS with TEOS as the silica source in the process to see whether it altered the reaction rate, allowing for a higher concentration of sodalite in the dried product (90 °C). The change was a noticeable improvement for the dried product from 76 mass% sodalite in the S5A specimens with CS to 96 mass% sodalite in the S5C specimen with TEOS.

Study 2 – *Organic germania source*. Here, we wanted to look at an organic source of germania as a replacement for silica, i.e., germanium (IV) ethoxide. The primary goal of this substitution was that we predicted that the germania-based gel, when pressed into pellets, would sinter at a lower temperature and that would reduce the Cl volatility and increase the density of the fired pellets for a higher volumetric waste loading. The drawback with exchanging Si for Ge is the increased costs associated with Ge. However, we wanted to explore this potential option. The high porosity in the initially fired pellets was a deterrent to pursuing this route any farther, though we did demonstrate a high germania-based sodalite concentration (82 mass%) in the as-made gel.

Study 3 – *Alternative sintering aids*. Here, we investigated alternative glass-binders to the NBS-1 glass. Since the viscosity of the NBS-1 glass is so high, the temperatures required for pellet densification were rather high (950 °C) and that led to chloride volatility, evidenced by a decrease in the sodalite concentration. In order to reduce the sintering temperatures, six alternative sintering aids were fabricated and added to the solution during the process. These sintering aids included four sodium borosilicate formulations, a sodium aluminophosphate formulation, and a lead-tellurite glass formulation (TPb_0). These samples were dried, pressed into pellets, fired at different temperatures, and the phases quantified. The sodium borosilicate glasses proved to dramatically improve the densification, up to 92% of ρ_t, of the fired pellets at much-reduced temperatures of ~750 °C, where reasonable amounts of sodalite were still produced (71 mass%).

In addition to adding a sintering aid to help consolidate the materials, we will be investigating alternative sintering techniques that include pressure control in order to maintain the stability of the sodalite structure. This will provide the ability to reduce porosity and increase density. We propose using spark-plasma sintering because it has high pressure capability plus the added benefit of voltage, which promotes grain bonding, resulting in reduced surface area. The spark-plasma sintering process is also rapid, <1 h, compared to traditional sintering which takes 10 to 24 h and this reduced heat-treatment time is expected to reduce chloride volatility.

Study 4 – *Gibbsite (SM-1), NaAlO$_2$ (SM-2), and Metakaolin (SM-3) Approaches*. In FY2012, we took a different approach to making high density sodalite pellets. Three different solution-based formulations were evaluated to make sodalite with the same simulated XCl_{20} salt. Several aspects were varied during the process including: the reactants, the amount of sintering aid added (0, 5, and 10 mass%), the step in the process when the sintering aid was added, calcination, and the timing of the calcination step in the process. The three sodalite methods (*SM-#*) used in the current study are *SM-1*, *SM-2*, and *SM-3*, simplified as:
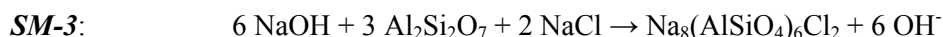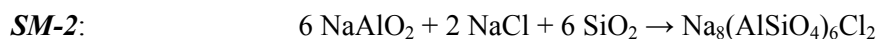
> ***SM-1***: $6\ NaOH + 6\ Al(OH)_3 + 2\ NaCl + 6\ SiO_2 \rightarrow Na_8(AlSiO_4)_6Cl_2 + 24\ OH^-$

SM-2: $6\ NaAlO_2 + 2\ NaCl + 6\ SiO_2 \rightarrow Na_8(AlSiO_4)_6Cl_2$

SM-3: $6\ NaOH + 3\ Al_2Si_2O_7 + 2\ NaCl \rightarrow Na_8(AlSiO_4)_6Cl_2 + 6\ OH^-$

The equations above are listed with the salt being denoted as ''NaCl'' but, in fact, the actual salt compositions contain R^{1+}, R^{2+}, and R^{3+} cations so the R:Cl ratio is not 1:1. The reactants were added in the proper amounts to obtain the targeted value for Al:Cl (3:1) and Si:Cl (3:1) where the alkali fraction (R^{1+}) was intentionally below the target of 4:1 (R^{1+}:Cl) to help influence the incorporation of alkaline earth and Ln components from the XCl$_{20}$ into the sodalite structure. The results from this study showed that each formulation had advantages and disadvantages where SM-3 pellets had high density and low sodalite production and SM-2 pellets had very high sodalite production with modestly high densities. A mixture of these methods will likely be considered in FY2013.

6   ACKNOWLEDGEMENTS

7   REFERENCES

ASTM C 1285-08. 2008. *Standard Test Methods for Determining Chemical Durability of Nuclear, Hazardous, and Mixed Waste Glasses and Multiphase Glass Ceramics: The Product Consistency Test (PCT)*, American Society for Testing and Materials International, West Conshohocken, PA.

Babad, H and DM Strachan. 1980. "Method for immobilizing radioactive iodine." US Patent No. 4229317.

Bak, M, JT Rasmussen, and NC Nielsen. 2000. "SIMPSON. A general simulation program for solid-state NMR spectroscopy." *Journal of Magnetic Resonance* **147**(2):296-330.

Ballirano, P and R Caminiti. 2001. "Rietveld refinements on laboratory energy dispersive X-ray diffraction (EDXD) data." *Journal of Applied Crystallography* **34**(6):757-62.

Barrett, WT and WE Wallace. 1954. "Studies of NaCl-KCl solid solutions. I. Heats of formation, lattice spacings, densities, Schottky defects and mutual solubilities." *Journal of the American Chemical Society* **76**(2):366-69.

Barth, TFW. 1932a. "The structure of the minerals of the sodalite family." *Zeitschrift für Kristallographie, Kristallgeometrie, Kristallphysik, Kristallchemie* **83**:405-14.

Barth, TFW. 1932b. "The structures of the minerals of the sodalite family." *Z. Kristallogr., Kristallgeom., Kristallphys., Kristallchem.* **83**:405-14.

Bateman, KJ, CJ Knight, and CW Solbrig. 2007. *Current Status of Ceramic Waste Form Development*. Report No. INL/INT-06-11736, Rev. 1, Idaho National Laboratory, Idaho Falls, ID.

Beagley, B, CMB Henderson, and D Taylor. 1982. "The crystal structures of aluminoslicate-sodalites: X-ray diffraction studies and computer modelling." *Mineralogical Magazine* **46**:459-64.

Beyer, H. 1967. "Verfeinerung der kristallstruktur von tellurit, dem rhombischen TeO_2." *Kristallografiya* **124**:228-38.

Brow, RK, DR Tallant, and GL Turner. 1997. "Polyhedral arrangements in lanthanum aluminoborate glasses." *Journal of the American Ceramic Society* **80**(5):1239-44.

Brunauer, S, PH Emmett, and E Teller. 1938. "Adsorption of gases in multimolecular layers." *Journal of the American Chemical Society* **60**(2):309-19.

Chowdari, BVR and PP Kumari. 1999. "Raman spectroscopic study of ternary silver tellurite glasses." *Materials Research Bulletin* **34**(2):327-42.

Chowdari, BVR, KL Tan, and F Ling. 2000. "Synthesis and characterization of $Cu_2O \cdot TeO_2$ and $CuI \cdot Cu_2O \cdot TeO_2$ glasses." *J. Mater. Sci.* **35**:2015-27.

Chowdari, BVR, KL Tan, and F Ling. 1998. "Characterization of $xCuI$-$(50-x)AgI$-yCu_2MoO_4-$(50-y)CuPO_3$ glasses." *Solid State Ionics* **107**(1-2):89-103.

Cressey, G. 2004. "Rock-forming minerals. Volume 4B. Second edition. framework silicates: Silica minerals, feldspathoids and the zeolites by Deer, W.A., Howie, R.A., Wise W.S. and Zussman, J." *Mineral. Mag.* **68**(5):831-32.

Crum, JV, BJ Riley, SK Sundaram, SA Arreguin, J Matyas, MJ Schweiger, BT Rieck, and JD Vienna. 2009. *Alternative Waste Forms for Electro-Chemical Salt Waste*. Report No. AFCI-WAST-PMO-MI-DV-2009-000293, Pacific Northwest National Laboratory, Richland, WA.

Darriet, J and J Galy. 1973. *Acta Crystallographica* **C2**:237-43.

Darriet, J, G Guillaume, K-A Wilhelmi, and J Galy. 1972. "Etude des composés $MVTeO_5$ (M = Na, K, Rb, Ag). Structure cristalline de $NaVTeO_5$." *Acta Chemica Scandinavica* **26**:59-70.

Dollase, WA and WM Thomas. 1978a. "The crystal chemistry of silica-rich, alkali-deficient nepheline." *Contributions to Mineralogy and Petrology* **66**(3):311-18.

Dollase, WA and WM Thomas. 1978b. "The crystal chemistry of silica-rich, alkali-deficient nepheline." *Contrib. Mineral. Petrol.* **66**(3):311-18.

Donald, IW, BL Metcalfe, SK Fong, LA Gerrard, DM Strachan, and RD Scheele. 2007. "A glass-encapsulated calcium phosphate wasteform for the immobilization of actinide-, fluoride-, and chloride-containing radioactive wastes from the pyrochemical reprocessing of plutonium metal." *Journal of Nuclear Materials* **361**(1):78-93.

Dong, Z, TJ White, B Wei, and K Laursen. 2002. "Model apatite systems for the stabilization of toxic metals: I, calcium lead vanadate." *Journal of the American Ceramic Society* **85**(10):2515-22.

Duverger, C, M Bouazaoui, and S Turrell. 1997. "Raman spectroscopic investigations of the effect of the doping metal on the structure of binary tellurium-oxide glasses." *Journal of Non-Crystalline Solids* **220**(2-3):169-77.

Ebert, WL. 2005. *Testing to Evaluate the Suitability of Waste Forms Developed for Electrometallurgically-Treated Spend Sodium-Bonded Nuclear Fuel for Disposal in the Yucca Mountain Repository*. Report No. ANL-05/43, Argonne National Laboratory-East, Argonne, IL.

Ebert, WL and SF Wolf. 1999. *Round-Robin Testing of a Reference Glass for Low-Activity Waste Forms*. Report No. ANL-99/22, Argonne National Laboratory, Argonne, Illinois.

Edwards, TG, EL Gjersing, S Sen, SC Currie, and BG Aitken. 2011. "125Te NMR chemical shifts and tellurium coordination environments in crystals and glasses in the Ge–As–Sb–Te system." *Journal of Non-Crystalline Solids* **357**(15):3036-41.

Ewing, RC, WJ Weber, and J Clinard, F.W. 1995. "Radiation effects in nuclear waste forms for high-level radioactive waste." *Progress in Nuclear Energy* **29**(2):63-127.

Fayon, F, I Farnan, C Bessada, J Coutures, D Massiot, and JP Coutures. 1997. "Empirical Correlations between 207Pb NMR Chemical Shifts and Structure in Solids." *Journal of the American Chemical Society* **119**(29):6837-43.

Feger, CR, GL Schimek, and JW Kolis. 1999. "Hydrothermal synthesis and characterization of $M_2Te_3O_8$ (M=Mn, Co, Ni, Cu, Zn): a series of compounds with the spiroffite structure." *Journal of Solid State Chemistry* **143**(2):246-53.

Fleet, ME. 1989. "Structures of sodium alumino-germanate sodalites [$Na_8(Al_6Ge_6O_{24})A_2$, A = Cl, Br, I]." *Acta Crystallographica* **C45**(6):843-47.

Folger, F. 1975a. "Die Kristallstruktur von Li_2TeO_3." *Journal of Inorganic and General Chemistry* **411**(2):103-10.

Folger, F. 1975b. "Die Kristallstruktur von $BaTeO_3$." *Journal of Inorganic and General Chemistry* **411**(2):111-17.

Foreman, N and DR Peacor. 1970. "Refinement of the nepheline structure at several temperatures." *Journal of Solid State - New Crystal Structures* **132**(1-6):45-70.

Frank, S, T Barber, and M Lambregts. 2005. " Powder diffraction of sodalite in a multiphase ceramic used to immobilize radioactive waste." *Powder Diffraction* **20**(3):212-14.

Frit, B, B Holmberg, and J Galy. 1970. "Structure cristalline de l'oxychlorure de baryum, Ba_4OCl_6." *Acta Crystallographica* **B26**(1):16-19.

Hanke, K. 1967. "Zinktellurit: kristallstruktur und beziehungen zu einigen seleniten." *Naturwissenschaften* **54**(8):199.

Hanke, K. 1966. "Die kristallstruktur von $Zn_2Te_3O_8$." *Naturwissenschaften* **53**(11):273.

Hartenbach, I and T Schleid. 2001. "Zwei Chloridsilicate des Yttriums: $Y_3Cl(SiO_4)_2$ und $Y_6Cl_{10}(Si_4O_{12})$." *Journal of Inorganic and General Chemistry* **627**(11):2493-98.

Haynes, WM, ed. Y-R Luo. 2011. *CRC Handbook of Chemistry and Physics*. 91st Ed., CRC Press/Taylor and Francis, Boca Raton, FL.

Heo, J, D Lam, GH Sigel, EA Mendoza, and DA Hensley. 1992. "Spectroscopic analysis of the structure and properties of alkali tellurite glasses." *Journal of the American Ceramic Society* **75**(2):277-81.

Hesse, K-F. 1977. "Refinement of the crystal structure of lithium polysilicate." *Acta Crystallographica* **B33**(3):901-02.

Himei, Y, A Osaka, T Nanba, and Y Miura. 1994. "Coordination change of Te atoms in binary tellurite glasses." *Journal of Non-Crystalline Solids* **177**:164-69.

Hocdé, S, SB Jiang, X Peng, N Peyghambarian, T Luo, and M Morrell. 2004. "Er^{3+} doped boro-tellurite glasses for 1.5 μm broadband amplification." *Optical Materials* **25**(2):149-56.

Holland, D, J Bailey, G Ward, B Turner, P Tierney, and R Dupree. 2005. "A 125Te and 23Na NMR investigation of the structure and crystallisation of sodium tellurite glasses." *Solid State Nucl. Magn. Reson.* **27**:16-27.

Hruby, A. 1972. "Evaluation of glass-forming tendency by means of DTA." *Czechoslovak Journal of Physics, Section B* **22**(11):1187-93.

Jacobson, AJ, BC Tofield, and BEF Fender. 1972. "The structures of $BaCeO_3$, $BaPrO_3$ and $BaTbO_3$ by neutron diffraction: lattice parameter relations and ionic radii in *O*-perovskites." *Acta Crystallographica* **B28**(3):956-61.

Kabalcı, İ, G Özen, and ML Öveçoğlu. 2009. "Microstructure and crystallization properties of TeO_2-PbF_2 glasses." *Journal of Raman Spectroscopy* **40**(3):272-76.

Kendrick, E and S Dann. 2004. "Synthesis, properties and structure of ion exchanged hydrosodalite." *Journal of Solid State Chemistry* **177**(4-5):1513-19.

Kim, Y-I, M-J Jung, and KH Kim. 2000. "Application of inverse pole figure to Rietveld refinement: III. Rietveld refinement of SnO_2 thin film using X-ray diffraction data." *Korean Journal of Ceramics* **6**(4):354-58.

Knop, O and G Demazeau. 1981. "The 1-6 weberite $Na_2Te_2O_7$ and some observations on compounds with the weberite structure." *Journal of Solid State Chemistry* **39**(1):94-99.

Konan, K, C Peyratout, A Smith, J Bonnet, S Rossignol, and S Oyetola. 2009. "Comparison of surface properties between kaolin and metakaolin in concentrated lime solutions." *Journal of Colloid and Interface Science* **339**(1):103-09.

Kondratyuk, IP, LA Muradyan, YV Pisarevskii, and VI Simonov. 1987. "Precision X-ray structure investigation of acoustooptical single crystals of α-TeO_2." *Kristallografiya* **32**(3):354-59.

Koyama, T. 1994. "Method to synthesize dense crystallized sodalite pellet for immobilizing halide salt radioactive waste." United States Patent No. 5340506.

Kozhukharov, VS, MR Marinov, and JN Pavlova. 1978. "Phase equilibria and immiscibility in the TeO_2-P_2O_5 system." *Journal of Materials Science* **13**(5):997-1005.

Kulcu, N. 1987. "Some new metastable compounds with a defect-type calcium fluoride (CaF_2) structure." *Doga: Turk Kimya Dergisi* **11**(1):27-31.

Larsen, FH, HJ Jakobsen, PD Ellis, and NC Nielsen. 1997. "Sensitivity-enhanced quadrupolar-echo NMR of half-integer quadrupolar nuclei. Magnitudes and relative orientation of chemical shielding and quadrupolar coupling tensors." *Journal Of Physical Chemistry A* **101**(46):8597-606.

Larsen, FH, AS Lipton, HJ Jakobsen, NC Nielsen, and PD Ellis. 1999. "67Zn QCPMG Solid-State NMR Studies of Zinc Complexes as Models for Metalloproteins." *Journal of the American Chemical Society* **121**(15):3783-84.

Leciejewicz, J. 1961. "The crystal structure of tellurium dioxide. A redetermination by neutron diffraction." *Journal of Solid State - New Crystal Structures* **116**(3-6):345-53.

Levenberg, K. 1944. "A method for the solution of certain problems in least squares." *Quart. Appl. Math* **2**:164-68.

Lezal, D, J Bludska, J Horak, A Sklenar, S Karamazov, and M Vlcek. 2002. "Raman spectra of TeO_2-$PbCl_2$ glasses." *Physics and Chemistry of Glasses* **43**(6):296-99.

Li, H, J Addai-Mensah, JC Thomas, and AR Gerson. 2005. "The influence of Al(III) supersaturation and NaOH concentration on the rate of crystallization of $Al(OH)_3$ precursor particles from sodium aluminate solutions." *Journal of Colloid and Interface Science* **286**(2):511-19.

Li, H, P Hrma, JD Vienna, M Qian, Y Su, and DE Smith. 2003. "Effects of Al_2O_3, B_2O_3, Na_2O, and SiO_2 on nepheline formation in borosilicate glasses: chemical and physical correlations." *Journal of Non-Crystalline Solids* **331**(1-3):202-16.

Lindner, G-G, W Massa, and D Reinen. 1995. "Structure and properties of hydrothermally synthesized thiosulfate cancrinite." *Journal of Solid State Chemistry* **117**(2):386-91.

Lipton, AS, JA Sears, and PD Ellis. 2001. "A general strategy for the NMR observation of half-integer quadrupolar nuclei in dilute environments." *Journal of Magnetic Resonance* **151**(1):48-59.

Lipton, AS, TA Wright, MK Bowman, DL Reger, and PD Ellis. 2002. "Solid-state Zn-67 NMR spectroscopy in bioinorganic chemistry. Spectra of four- and six-coordinate zinc pyrazolylborate complexes obtained by management of proton relaxation rates with a paramagnetic dopant." *Journal of the American Chemical Society* **124**(20):5850-60.

Liu, Q, A Navrotsky, CF Jove-Colon, and F Bonhomme. 2007. "Energetics of cancrinite: effect of salt inclusion." *Microporous and Mesoporous Materials* **98**(1-3):227-33.

Loopstra, BO and K Goubitz. 1986. "The structures of four caesium tellurates." *Acta Crystallographica* **C42**(5):520-23.

Mazzuca, M, J Portier, B Tanguy, F Romain, A Fadli, and S Turrell. 1995. "Raman scattering in tellurium-metal oxide glasses." *Journal of Molecular Structure* **349**:413-16.

McCarthy, GJ and JM Welton. 1989. "X-Ray diffraction data for SnO_2. An illustration of the new powder data evaluation methods." *Powder Diffraction* **4**(3):156-59.

McMullan, RK, S Ghose, N Haga, and V Schomaker. 1996. "Sodalite, $Na_4Si_3Al_3O_{12}Cl$: structure and ionic mobility at high temperatures by neutron diffraction." *Acta Crystallgraphica B* **52**:616-27.

Meier, WM. 1973. "Symmetry Aspects of Zeolite Frameworks." In *Molecular Sieves: Pt. 1 (Advances in Chemistry Series)*, eds. WM Meier and JB Uytterhoeven, Vol 121, pp. 39-51. Schweizerische Chemische Gesellschaft, Bern, Switzerland.

Meunier, G and J Galy. 1971. "Sur une déformation inédite du reseau de type fluorine. Structure cristalline des phases MTe$_3$O$_8$ (M = Ti, Sn, Hf, Zr)." *Acta Crystallographica* **B27**:602-08.

Meyer, G, J Soose, A Moritz, V Vitt, and TH Holljes. 1985. "Ternaere Halogenide der seltenen Erden vom Typ A_2MX_5. (A=K, In, NH_4, Rb, Cs; X=Cl, Br, I)." *Journal of Inorganic and General Chemistry* **521**:161-72.

Mineralogy Database. 2011. Accessed 2009-2011 at http://www.webmineral.com/ (last updated 10/01/2011).

Misra, C. 1970. "Methods, apparatus: new product research, process development and design: Solubility of aluminium trihydroxide (hydrargillite) in sodium hydroxide solutions." In *Chemistry and Industry*, ed. TF West, Vol 19, pp. 619-23. Society of Chemical Industry, London.

Moller, CK. 1957. "A phase transition in caesium plumbochloride." *Nature* **180**(4593):981-82.

Montagne, L, S Donze, G Palavit, JC Boivin, F Fayon, D Massiot, J Grimblot, and L Gengembre. 2001. "207Pb and 113Cd NMR and XPS characterization of PbO–PbCl2–CdCl2 glasses." *Journal of Non-Crystalline Solids* **293–295**(0):74-80.

Murugan, GS, T Suzuki, and Y Ohishi. 2006. "Raman characteristics and nonlinear optical properties of tellurite and phosphotellurite glasses containing heavy metal oxides with ultrabroad Raman bands." *Journal of Applied Physics* **100**(2):023107-1 - 07-6.

Nachimuthu, P and R Jagannathan. 1995. "Tb3+ fluorescence as a probe of cluster formation in lead oxyfluoride glasses." *Journal of Non-Crystalline Solids* **183**(1–2):208-11.

Neov, S, I Gerasimova, V Kozhukharov, P Mikula, and P Lukas. 1995. "Structural study of complex tellurite glasses." *Journal of Non-Crystalline Solids* **192-193**:53-56.

Neov, S, V Kozhukharov, I Gerasimova, and B Sidzhimov. 1990. "Neutron diffraction investigation of the short range order in TeO2---BiCl3 glassy system." *Journal of Non-Crystalline Solids* **126**(3):255-58.

Ocanto, F, R Alvarez, CU de Navarro, A Lieb, and CF Linares. 2008. "Influence of the alkalinity and NO$_3^-$/Cl$^-$ anionic composition on the synthesis of the cancrinite-sodalite system." *Microporous and Mesoporous Materials* **116**(1-3):318-22.

Ocanto, F, E Figueredo, M Brikgi, CUd Navarro, and CF Linares. 2009. "Oxidation-reduction reactions: a novel method in the synthesis of nitrate cancrinite-type zeolites." *Materials Letters* **63**(1):11-14.

Ott, H. 1923. "Die raumgitter der lithiumhalogenide." *Physikalische Zeitschrift* **24**:209-13.

Park, H-S, I-T Kim, H-Y Kim, K-S Lee, S-K Ryu, and J-H Kim. 2002. "Application of Apatite Waste Form for the Treatment of Water-Soluble Wastes Containing Radioactive Elements. Part I: Investigation on the Possibility." *Journal of Industrial and Engineering Chemistry* **8**(4):318-27.

Porter, Y and PS Halasyamani. 2003. "Syntheses, Structures, and Characterization of New Lead(II)−Tellurium(IV)−Oxide Halides: Pb$_3$Te$_2$O$_6$X$_2$ and Pb$_3$TeO$_4$X$_2$ (X = Cl or Br)." *Inorganic Chemistry* **42**(1):205-09.

Rada, S, A Dehelean, and E Culea. 2011. "FTIR and UV-VIS spectroscopy investigations on the structure of the europium-lead-tellurate glasses." *Journal of Non-Crystalline Solids* **357**(16-17):3070-73.

Riley, BJ, JV Crum, J Matyas, JS McCloy, and WC Lepry. 2012a. "Solution-derived, chloride-containing minerals as a waste form for alkali chlorides." *Journal of the American Ceramics Society (in press)*.

Riley, BJ, JS McCloy, JV Crum, CP Rodriguez, CF Windisch Jr., WC Lepry, J Matyas, MP Westman, BT Rieck, JB Lang, and DA Pierce. 2011. *Alternative Electrochemical Salt Waste Forms, Summary of*

FY/CY2011 Results. Report No. FCRD-SWF-2012-000028, Pacific Northwest National Laboratory, Richland, WA.

Riley, BJ, BT Rieck, JV Crum, J Matyas, J McCloy, SK Sundaram, and JD Vienna. 2010. *Alternative Electrochemical Salt Waste Forms, Summary of FY2010 Results*. Report No. FCRD-WAST-2010-000129, Pacific Northwest National Laboratory, Richland, WA.

Riley, BJ, BT Rieck, JS McCloy, JV Crum, SK Sundaram, and JD Vienna. 2012b. "Tellurite glass as a waste form for mixed alkali-chloride waste streams: candidate materials selection and initial testing." *Journal of Nuclear Materials* **424**(1-3):29-37.

Rodriguez, CP, J McCloy, MJ Schweiger, JV Crum, and A Winschell. 2011. *Optical basicity and nepheline crystallization in high alumina glasses*. Report Pacific Northwest National Laboratory, Richland, WA.

Rong, QJ, A Osaka, T Nanba, J Takada, and Y Miura. 1992. "Infrared and Raman spectra of binary tellurite glasses containing boron and indium oxides." *Journal of Materials Science* **27**(14):3793-98.

Sakida, S, S Hayakawa, and T Yoko. 1999a. "Part 1. ^{125}Te NMR study of tellurite crystals." *Journal of Non-Crystalline Solids* **243**(1):1-12.

Sakida, S, S Hayakawa, and T Yoko. 2001. "^{125}Te, ^{27}Al, and ^{71}Ga NMR Study of M_2O_3–TeO_2 (M = Al and Ga) Glasses." *Journal of the American Ceramic Society* **84**(4):836-42.

Sakida, S, S Hayakawa, and T Yoko. 1999b. "^{125}Te NMR Study of MO-TeO_2 (M=Mg, Zn, Sr, Ba and Pb) Glasses." *Journal of the Ceramic Society of Japan* **107**(5):395-402.

Sakida, S, S Hayakawa, and T Yoko. 1999c. "Part 2. ^{125}Te NMR study of M_2O-TeO_2 (M = Li, Na, K, Rb and Cs) glasses." *Journal of Non-Crystalline Solids* **243**(1):13-25.

Sciau, P, J Lapasset, and J Moret. 1986. "Structure de la phase quadratique de $PbTeO_3$." *Acta Crystallographica* **C42**(12):1688-90.

Seemann, H. 1956. "Die kristallstruktur des lithiummetasilikates, $(Li_2SiO_3)_x$." *Acta Crystallographica* **9**(3):251-52.

Sekiya, T, N Mochida, and S Ogawa. 1994a. "Structural study of WO_3-TeO_2 glasses." *Journal of Non-Crystalline Solids* **176**(2-3):105-15.

Sekiya, T, N Mochida, and A Ohtsuka. 1994b. "Raman spectra of MO-TeO_2 (M = Mg, Sr, Ba and Zn) glasses." *Journal of Non-Crystalline Solids* **168**(1-2):106-14.

Sekiya, T, N Mochida, A Ohtsuka, and M Tonokawa. 1992. "Raman spectra of $MO_{1/2}TeO_2$ (M = Li, Na, K, Rb, Cs and Tl) glasses." *Journal of Non-Crystalline Solids* **144**:128-44.

Sekiya, T, N Mochida, and A Soejima. 1995. "Raman spectra of binary tellurite glasses containing tri- or tetra-valent cations." *Journal of Non-Crystalline Solids* **191**(1-2):115-23.

Shannon, RD. 1976. "Revised effective ionic radii and systematic studies of interatomic distances in halides and chalcogenides." *Acta Crystallographica Section A* **32**:751-67.

Silva, MAP, Y Messaddeq, SJL Ribeiro, M Poulain, F Villain, and V Briois. 2001. "Structural studies on TeO$_2$-PbO glasses." *Journal of Physics and Chemistry of Solids* **62**(6):1055-60.

Sokolov, VO, VG Plotnichenko, and VV Koltashev. 2009. "Structure of barium chloride-oxide tellurite glasses." *Journal of Non-Crystalline Solids* **355**(31–33):1574-84.

Sokolowski, J and A Kotarba. 1998. The structure of potassium aluminium oxide KAlO$_2$. In *Proceedings of 6th European Powder Diffraction Conference*. 954-59 pp.

Sokolowski, J and A Kotarba. 2000. "The structure of potassium aluminum oxide." *Materials Science Forum* **321-324**:954-59.

Srinivasa, RB and SP Sanyal. 1990. "Structural and elastic properties of sodium halides at high pressure." *Physical Review B: Condensed Matter and Materials Physics* **42**(3):1810-16.

Stratton, SW. 1924. *Standard density and volumetric tables*, 6th ed., United States National Bureau of Standards, Government Printing Office, Washington.

Tait, KT, E Sokolova, FC Hawthorne, and AP Khomyakov. 2003a. "The crystal structure of nepheline." *The Canadian Mineralogist* **41**(1):61-70.

Tait, KT, E Sokolova, FC Hawthorne, and AP Khomyakov. 2003b. "The crystal chemistry of nepheline." *Canadian Mineralogist* **41**:61-70.

Tamazyan, RA, YA Malinovskii, and AM Il'inets. 1988. "Atomic structure and microtwinning of sodalite." *Soviet Physics, Crystallography* **33**(3):325-29.

Tanaka, K, T Yoko, H Yamada, and K Kamiya. 1988a. "Structure and ionic conductivity of LiCl-Li$_2$O-TeO$_2$ glasses." *Journal of Non-Crystalline Solids* **103**(2-3):250-56.

Tanaka, K, T Yoko, H Yamada, and K Kamiya. 1988b. "Structure and ionic conductivity of LiCl-Li$_2$O-TeO$_2$ glasses." *Journal of Non-Crystalline Solids* **103**:250-56.

Tatar, D, G Özen, FB Erim, and ML Öveçoğlu. 2010. "Raman characterizations and structural properties of the binary TeO$_2$-WO$_3$, TeO$_2$-CdF$_2$ and ternary TeO$_2$-CdF$_2$-WO$_3$ glasses." *Journal of Raman Spectroscopy* **41**(7):797-807.

Thompson, JG, RL Withers, A Melnitchenko, and SR Palethorpe. 1998a. "Cristobalite-related phases in the NaAlO$_2$-NaAlSiO$_4$ system. I. Two tetragonal and two orthorhombic structures." *Acta Crystallographica* **B54**(5):531-46.

Thompson, JG, RL Withers, A Melnitchenko, and SR Palethorpe. 1998b. "Cristobalite-related phases in the NaAlO$_2$-NaAlSiO$_4$ system. I. Two tetragonal and two orthorhombic structures." *Acta Crystallogr., Sect. B: Struct. Sci.* **B54**(5):531-46.

Tromel, M and H Ziethen-Reichnach. 1970. "Magnesiumtellurite." *Journal of Inorganic and General Chemistry* **378**(3):238-44.

Vance, ER, J Davis, K Olufson, I Chironi, I Karatchevtseva, and I Farnan. 2012. "Candidate waste forms for immobilisation of waste chloride salt from pyroprocessing of spent nuclear fuel." *Journal of Nuclear Materials* **420**(1-3):396-404.

Vienna, J. 2010. "Nuclear waste vitrification in the United States: recent developments and future options." *Inernational Journal of Applied Glass Science* **1**(3):309-231.

Vienna, JD, J Luey, PR Hrma, DE Smith, RD Scheele, HL Wigent, and JV Crum. 1998. Glass frit development for encapsulation of rocky flats ash. Presented at *Environmental Issues and Waste Management Technologies in the Ceramic and Nuclear Industries IV*, Vol. 93, 399-407 pp., The American Ceramics Society, Westerville, OH.

Vogel, W, H Burger, G Zerge, B Muller, K Forkel, G Winterstein, A Boxberger, and H Romhild. 1974. "Halogenid- und sulfathaltige telluritglaser." *Silikattechnik* **25**(6):207-08.

Wang, D-N, Y-Q Guo, K-M Liang, and K Tao. 1999. "Crystal structure of zirconia by Rietveld refinement." *Science in China - Series A: Mathematics, Physics, Astronomy & Technological Sciences* **42**(1):80-86.

Wang, JS, EM Vogel, and E Snitzer. 1994. "Tellurite glass: a new candidate for fiber devices." *Optical Materials* **3**(3):187-203.

Weber, WJ, RP Turcotte, LR Bunnell, FP Roberts, and JH Westsik. 1979. "Radiation effects in vitreous and devitrified smulated waste glass." In *Ceramics in Nuclear Waste Management*, eds. TD Chikalla and JE Mendel, pp. 294-99. National Technical Information Service, Springfield, VA.

Withers, RL and JG Thompson. 1993. "Modulation wave approach to the structural parameterization and Rietveld refinement of low carnegieite." *Acta Crystallographica* **B49**(4):614-26.

Yakhkind, AK and SA Chebotarev. 1980. "Glass formation, crystallization ability, density and thermal expansion of glasses in ternary tellurite halogen systems." *Fizika i Khimiya Stekla* **6**(2):164-69.

Yoo, TS. Personal communication. 2009. "Personal Communication by electronic mail."

Zachariasen, WH. 1929. "The crystal structure of sodium chlorate." *Journal of Solid State - New Crystal Structures* **71**(5-6):517-29.

Zaslavsky, AI, D Kondrashev, and S Tolkachev. 1950. "The new modification of lead dioxide and the texture of anode sediments." *Doklady Akademii Nauk SSSR* **75**:559-61.

Appendix A: Structural Notations in Tellurite Glass

Overview of Structural Units in Tellurite Glass

A tellurite glass network consists of several different structural arrangements depending on the specific glass network modifiers, intermediates, and other additives present in the glass. X-ray diffraction (XRD) (Brady, 1956, 1957; Dimitriev et al., 1987), neutron diffraction (Neov et al., 1979), Fourier transform infrared (FTIR) spectroscopy (Dimitriev et al., 1987; Heo et al., 1992), Raman spectroscopy (Khatir et al., 1993; Duverger et al., 1997; Dimitriev et al., 1983; Kashchieva, 1984; Sekiya et al., 1994a; Chowdari and Kumari, 1999; Murugan et al., 2005, 2006; Sekiya et al., 1994b), nuclear magnetic resonance (^{125}Te NMR) (Sakida et al., 1999c; Sakida et al., 1999a, b; Sakida et al., 2001), extended X-ray absorption fine structure (Shimizugawa et al., 1995; Yamamoto et al., 1994), and Mössbauer spectroscopy (Nishida et al., 1990) have all been used to determine the various structural configurations present in tellurite glasses. Also, observations of tellurite structural units have been discussed in the literature as they are affected by alkali (Rao and Bhat, 2001a; Bhat et al., 2004; Arnaudov et al., 1982; Akagi et al., 1999), alkaline earth (Arnaudov et al., 1982), and transition metal (Arnaudov et al., 1982; Kuzhukharov et al., 1986; Bürger et al., 1992) oxide additives.

Thus far, at least eight different Te structural units have been identified that can be broadly categorized as either asymmetrical trigonal bipyramidal (*tbp* or TeO$_4$) or trigonal pyramidal (*tp* or TeO$_3$) units. These different structural units are referred to with a wide variety of notations, with the most common being the polyhedral (e.g., TeO$_4$, TeO$_3$) and NMR (Sakida et al., 2001) notations. In the NMR notation, N_4^0, for example, indicates a Te polyhedron with four bonding oxygens (subscript) and a zero net charge (superscript). When modifiers are introduced into the tellurite network, the *tbp* structural units are no longer crystallographically constrained (Akagi et al., 1999; Neov et al., 1978). Additives stabilize the vitreous state, depolymerizing it to include fractions of TeO$_3$ or *tp*-type units, although glasses still retain the α-TeO$_2$ (*tbp*-type) framework structure (Arnaudov and Dimitriev, 2001). In the *tp* units, only three oxygens are bonded to the Te atom and one of the oxygens is double-bonded. Within all of these structures exist structural moieties where some (or all) of the oxygens are non-bridging.

In addition to the polyhedral notation (e.g., TeO$_4$, TeO$_3$), the $T_{b.o.}^c$ notation is quite useful, where "T" is the Te atom, "c" is the charge on the structural unit, and "b.o." is the number of bridging oxygens included in the structural unit. These notations with their equivalence are presented in Table A.1 with pictorial representations in Figure A.1, based on compiled data from the literature (Himei et al., 1994; Sekiya et al., 1994b; Lindqvist, 1968; Rao and Bhat, 2001b; Sakida et al., 1999c; Sakida et al., 1999a). For example, according to the literature (Lindqvist, 1968), in crystalline α-TeO$_2$, the Te has a 5s^2 lone pair of electrons in the valence shell, and the preferred structural units are TeO$_4$, more specifically T_4^0 (neutral charge on structure with four bridging oxygens), or in our shorthand, *tbp*1 (Bhat et al., 2004). In the *tpb*1 configuration, the distance between the Te atom and both axial oxygens (i.e., Te–O$_{ax}$) is 2.08 ± 0.02 Å, and the distance between the Te atom and both equatorial oxygens (i.e., Te–O$_{eq}$) is 1.90 ± 0.02 Å (Lindqvist, 1968; Kuzhukharov et al., 1986). The tetragonal α-TeO$_2$ ("paratellurite") crystal consists of corner-shared trigonal bipyramidal TeO$_4$ units and has a density of ~5.75 g/cm^3. The β-TeO$_2$ ("tellurite") crystal has an orthorhombic, layered structure, consisting of edge-shared trigonal bipyramidal TeO$_4$ units with a higher density of ~6.04 g/cm^3 (Patnaik, 2003). In all of the tellurite structural units, there exists a lone pair of electrons at the unoccupied equatorial position on the Te atom, a position that is generally accepted as being present in one of the sp^3d hybridized orbitals (Lindqvist, 1968; Rao and Bhat, 2001a).

Another structural unit, known usually as TeO$_{3+1}$ (denoted here *tp*0) can be found in tellurite crystals when one Te-O$_{ax}$ is stretched so that the local coordination is three with a fourth oxygen some further distance away (Kuzhukharov et al., 1986) (Figure A.1). In some sense this is intermediate between *tbp*, as it coordinated by four oxygens, and *tp*, as it has only three nearby oxygens. From another perspective, TeO$_{3+1}$ units result from a continuous section of a tellurite glass chain of mostly TeO$_4$ *tbp* units with TeO$_3$ *tp* units on either end, forming *tp*2-*tbp*3-*tp*2, or a [Te$_3$O$_8$]$^{4-}$ unit (Sekiya et al., 1994b). If several of these sections are put together, the end *tp* units of each section resemble "loosely associated" TeO$_{3+1}$, with the "other" oxygen being contributed by the next chain fragment. This gives a *tp*0-*tbp*3-*tp*0 sequence that can

be represented as $[Te_3O_8]_\infty^{4-}$ (Sekiya et al., 1994b). A detailed explanation for the formation of structural reconfigurations in tellurite glasses has been given elsewhere (Rao and Bhat, 2001a).

Table A.1. Tellurium oxide structural units present in glass according to the literature, represented in various notations.*

Unit	*tbp*1 (Himei et al., 1994)	*tbp*2 (Himei et al., 1994)	*tbp*3 (Sekiya et al., 1994b)	*tp*1 (Himei et al., 1994)	*tp*2 (Himei et al., 1994)	*tp*3 (Sakida et al., 1999a)
Polyhedron	TeO_4	TeO_4	TeO_4	TeO_3	TeO_3	TeO_3
Alternative polyhedron notation		$TeO_{3/2+1}{}^-$		$TeO_{2/2+1}$	$TeO_{1/2+2}{}^-$	$TeO_{1+1}{}^-{}_{+1}{}^-$
$T_{b.o.}^{chg}$ notation	T_4^0	T_3^{-1}	T_2^{-2}	T_2^0	T_1^{-1}	T_0^{-2}
NMR notation (Sakida et al., 2001)	N_4^0	N_4^-	N_4^{2-}	N_3^0	N_3^-	N_3^{2-}
Type	(α-TeO_2)			(Bridging)	(Terminal)	(Isolated)
Bonding	$TeO_{4/2}$	$O_{3/2}Te\text{-}O^-$	$O_{2/2}Te(\text{-}O^-)\text{-}O^-$	$O_{2/2}Te\text{=}O$	$O_{1/2}Te(\text{=}O)\text{-}O^-$	$O\text{=}Te(\text{-}O^-)\text{-}O^-$
Q^n	Q^4	Q^3	Q^2	Q^2	Q^1	Q^0
Number of NBO (including double bonds)	0	1	2	1	2	3
Number of double bonds	0	0	0	1	1	1
Equivalent in network	TeO_2	$[Te_2O_5]^{2-}$	$[TeO_3]^{2-}$	TeO_2	$[Te_2O_5]^{2-}$	$[TeO_3]^{2-}$
Description	--------- Trigonal bypramidal ---------				Pyramid pairs	Isolated pyramids

*Note that the TeO_{3+1} unit cannot be clearly considered by any of these models. It is nominally 4-coordinated like the other *tbp* units, but the 4th oxygen is farther away so it could be considered 3-coordinated like the *tp* units. It is therefore an intermediate configuration which in an uncharged state can be described as $O_{3/2}Te(\text{---}O)$ (Sekiya et al., 1994b). Depending on the number of non-bridging oxygens this structure could be described as N_4^0 or N_3^0 (0 NBO), N_4^- or N_3^- (1 NBO), or N_4^{2-} or N_3^{2-} (2 NBO), again depending on the convention of considering it as a *tp* or *tbp* unit. It is not clear whether these charged structures actually exist in real glasses. Whether considered as trigonal or tetrahedral, it represents structures which have been depolymerized by additives. According to Sakida et al. (Sakida et al., 1999c) and references therein, this unit can be said to be non-existent in tellurite glasses due to the lack of expected signature in the Raman spectrum at 900 cm^{-1}.
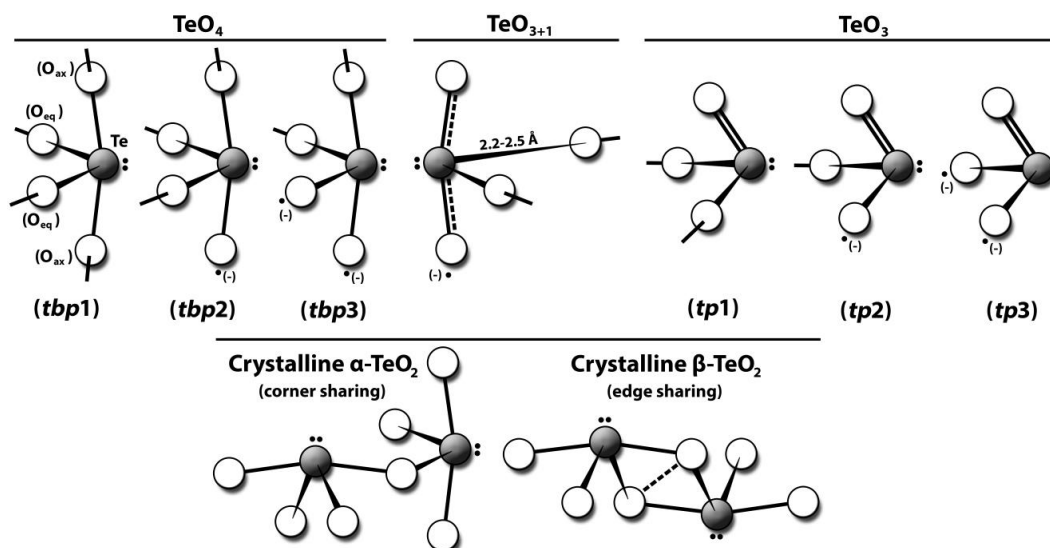
Figure A.1. TeO$_4$ trigonal bipyramidal, *tbp*, and TeO$_3$ trigonal pyramidal, *tp*, structural units in tellurite glasses based on representations in the literature. Species presented in order of decreasing quantity of bridging oxygens (4→0). Oxygen assignments are broken down into equatorial positions (O$_{eq}$) and axial positions (O$_{ax}$) for *tbp*1. Similar assignments could be made for *tbp*2 and *tbp*3. One oxygen of TeO$_{3+1}$ is unique as it is farther away. Lone pair electrons are shown as small black dots near the central dark Te atom.   Non-bridging oxygen (denoted as negative sign in parenthesis) assignments were chosen arbitrarily. This illustration is not exhaustive but shows the complexity of Te-O conformations.

Known effects of Pb and of Cl on tellurite glass structures

Few structural studies of lead-tellurite glasses have been reported, however, these did provide some insight to the current study. Studies based on Raman spectroscopy of lead-tellurite glasses revealed that TeO$_3$ structural units tend to dominate the glass structure as PbO is added to tellurite glass, thus Pb is deemed to act as a network modifier that depolymerizes the tellurite network (Khatir et al., 1993; Duverger et al., 1997; Kaur et al., 2010; Lezal et al., 2002; Komatsu and Mohri, 1999; Silva et al., 2001). However, according to X-ray absorption spectroscopy, increasing PbO also promotes the conversion of 6-coordinated PbO$_6$ octahedra into 4-coordinated PbO$_4$ tetrahedra with more non-bridging oxygens, indicating that the Pb also takes part in forming the glass network (Silva et al., 2001). Also, Te–O–Pb linkages exist in the network but are progressively broken by non-bridging oxygens as more PbO is added.

The structural effects of chlorides on the tellurite glass network have been studied to a lesser extent (Rao and Bhat, 2001a; Bhat et al., 2004; Rojo et al., 1990; Tanaka et al., 1988). In most studies where alkali chloride(s) are added to a tellurite glass, it is difficult to disentangle the effects of alkali and chloride addition on the depolymerization of the tellurite network. With XRD, Iwadate et al. (Iwadate et al., 2000) determined that the average coordination number of the Te atoms in LiCl-Li$_2$O tellurite glasses was three to four, indicating a mixture of *tp* and *tbp* Te species, and they suggested that Cl$^-$ substituted for O^{2-} in the network. Rao and Bhat (Rao and Bhat, 2001a) and Bhat et al. (Bhat et al., 2004) made several borotellurite glasses with and without Li$_2$O, including varying additions of LiCl, and they did not expect the LiCl to influence the tellurite glass network structure. In their studies, adding LiCl resulted in a *tbp* → *tp* conversion. In contrast, when studying TeO$_2$-Li$_2$O-LiCl glasses through vibrational spectroscopy, Tanaka et al. (Tanaka et al., 1988) found that when LiCl was added to a TeO$_2$-Li$_2$O matrix, the LiCl formed a non-bridging oxygen bond, Te–Cl$_{eq}$, in place of one of the Te–O$_{eq}$ bonds ("eq" denotes an equatorial oxygen – see Figure A.1). This, in turn, strengthened the Te–O$_{ax}$ bond and suppressed formation of the *tp* species ("ax" denotes an axial oxygen – see Figure A.1). A thorough understanding on the effect of Cl in the tellurite network is still lacking.

A very few studies have looked at systems with Te, Pb, O, and Cl. A study of the glass structure of TeO_2-$PbCl_2$ suggested that the glass was composed of tellurite *tbp* and *tp* units in addition to octahedral PbO_aCl_b and tetrahedral PbO_4 units in analogy to other PbO-PbZ glasses, where *Z* is a halogen (Lezal et al., 2002). In mixed PbO-PbF_2 glass, 8-coordinated lanthanides are thought to be incorporated in the interstitials formed by six PbO_xF_y octahedral (Nachimuthu and Jagannathan, 1995). Two known Te-Pb-O-Cl crystal structures are $Pb_3Te_2O_6Cl_2$ and $Pb_3TeO_4Cl_2$ and the bonds are considered to be Pb–O, Pb–Cl, and Te–O (Porter and Halasyamani, 2003). In other words, lead oxide-halide polyhedra (8 or 9 coordinated) are connected to tellurium oxide groups (3 or 4 coordinated). The lone pair electrons that exist both in Pb^{2+} and Te^{4+} are oriented toward the halide ions (Porter and Halasyamani, 2003).

References

Akagi, R, K Handa, N Ohtori, AC Hannon, M Tatsumisago, and N Umesaki. 1999. "High-temperature structure of K_2O-TeO_2 glasses." *Journal of Non-Crystalline Solids* **256&257**:111-18.

Arnaudov, M and Y Dimitriev. 2001. "Study on the structural transition in binary tellurite glasses by means of reduced infrared spectra." *Physics and Chemistry of Glasses* **42**(2):99-102.

Arnaudov, M, V Dimitrov, Y Dimitriev, and L Markova. 1982. "Infrared-spectral investigation of tellurites." *Materials Research Bulletin* **17**(9):1121.

Bhat, MH, M Kandavel, M Ganguli, and KJ Rao. 2004. "Li^+ ion conductivities in boro-tellurite glasses." *Bull. Mater. Sci.* **27**(2):189-98.

Brady, GW. 1956. "X-ray study of tellurium oxide glass." *Journal of Chemical Physics* **24**(2):477-78.

Brady, GW. 1957. "Structure of tellurium oxide glass." *Journal of Chemical Physics* **27**(1):300-03.

Bürger, H, K Kneipp, H Hobert, W Vogel, V Kozhukharov, and S Neov. 1992. "Glass formation, properties and structure in the TeO_2-ZnO system." *Journal of Non-Crystalline Solids* **151**:134-42.

Chowdari, BVR and PP Kumari. 1999. "Raman spectroscopic study of ternary silver tellurite glasses." *Materials Research Bulletin* **34**(2):327-42.

Dimitriev, Y, V Dimitrov, E Gatev, E Kashchieva, and H Petkov. 1987. "Effect of the mode formation on the structure of tellurite glasses." *Journal of Non-Crystalline Solids* **95-96**(2):937-44.

Dimitriev, Y, E Kashchieva, I Ivanova, and D Khristova. 1983. "Liquidation in three-component tellurite systems TeO_2-B_2O_3-M_nO_m. M_nO_m=Al_2O_3, Ga_2O_3, Cr_2O_3, CuO, Ag_2O, MoO_3, Sb_2O_3." *Stroit. Mater. Silikat. Prom.* **24**(9):24.

Duverger, C, M Bouazaoui, and S Turrell. 1997. "Raman spectroscopic investigations of the effect of the doping metal on the structure of binary tellurium-oxide glasses." *Journal of Non-Crystalline Solids* **220**(2-3):169-77.

Heo, J, D Lam, GH Sigel, EA Mendoza, and DA Hensley. 1992. "Spectroscopic analysis of the structure and properties of alkali tellurite glasses." *Journal of the American Ceramic Society* **75**(2):277-81.

Himei, Y, A Osaka, T Nanba, and Y Miura. 1994. "Coordination change of Te atoms in binary tellurite glasses." *Journal of Non-Crystalline Solids* **177**:164-69.

Iwadate, Y, H Kenmotsu, T Hattori, S Nishiyama, K Fukushima, N Umesaki, T Nakazawa, and K Noda. 2000. "X-ray diffraction study of the short-range structure of LiCl-Li$_2$O-TeO$_2$ glasses." *Journal of Alloys and Compounds* **305**:130-35.

Kashchieva, E. 1984. "Phase separation in tellurite systems." Sofia University, Sofia, Bulgaria: Thesis.

Kaur, A, A Khanna, C Pesquera, F González, and V Sathe. 2010. "Preparation and characterization of lead and zinc tellurite glasses." *Journal of Non-Crystalline Solids* **356**(18-19):864-72, 10.1016/j.jnoncrysol.2010.01.005.

Khatir, S, F Romain, J Portier, S Rossignol, B Tanguy, JJ Videau, and S Turrell. 1993. "Raman studies of recrystallized glasses in the binary TeO$_2$-PbO system." *Journal of Molecular Structure* **298**:13-16.

Komatsu, T and H Mohri. 1999. "Raman scattering spectra and optical properties of tellurite glasses and crystalline phases containing PbO and CdO." *Physics and Chemistry of Glasses* **40**:257-63.

Kuzhukharov, V, H Burger, S Neov, and B Sidzhimov. 1986. "Atomic arrangement of a zinc-tellurite glass." *Polyhedron* **5**(3):771-77.

Lezal, D, J Bludska, J Horak, A Sklenar, S Karamazov, and M Vlcek. 2002. "Raman spectra of TeO$_2$-PbCl$_2$ glasses." *Physics and Chemistry of Glasses* **43**(6):296-99.

Lindqvist, O. 1968. "Refinement of the structure of α-TeO$_2$." *Acta Chemica Scandinavica* **22**:977-82.

Murugan, GS, T Suzuki, and Y Ohishi. 2005. "Phospho-tellurite glasses containing heavy metal oxides for ultrabroad band fiber Raman amplifiers." *Applied Physics Letters* **86**(22):221109-1-3.

Murugan, GS, T Suzuki, and Y Ohishi. 2006. "Raman characteristics and nonlinear optical properties of tellurite and phosphotellurite glasses containing heavy metal oxides with ultrabroad Raman bands." *Journal of Applied Physics* **100**(2):023107-1 - 07-6.

Nachimuthu, P and R Jagannathan. 1995. "Tb3+ fluorescence as a probe of cluster formation in lead oxyfluoride glasses." *Journal of Non-Crystalline Solids* **183**(1–2):208-11, 10.1016/0022-3093(94)00586-9.

Neov, S, I Gerassimova, K Krezhov, B Sydzhimov, and V Kozhukharov. 1978. "Atomic arrangement in tellurite glasses studied by neutron diffraction." *physica status solidi (a)* **47**(2):743-50.

Neov, S, V Kozhukharov, I Gerasimova, K Krezhov, and B Sidzhimov. 1979. "A model for structural recombination in tellurite glasses." *Journal of Physics C: Solid State Physics* **12**(13):2475-85.

Nishida, T, M Yamada, H Ide, and Y Takashima. 1990. "Correlation between the structure and glass transition temperature of potassium, magnesium and barium tellurite glasses." *Journal of Materials Science* **25**(8):3546-50.

Patnaik, P. 2003. *Handbook of Inorganic Chemicals*, McGraw-Hill, New York.

Porter, Y and PS Halasyamani. 2003. "Syntheses, Structures, and Characterization of New Lead(II)−Tellurium(IV)−Oxide Halides: Pb$_3$Te$_2$O$_6$X$_2$ and Pb$_3$TeO$_4$X$_2$ (X = Cl or Br)." *Inorganic Chemistry* **42**(1):205-09, 10.1021/ic025750j.

Rao, KJ and MH Bhat. 2001a. "Investigation of lithium chloride-lithium borate-tellurium dioxide

glasses: an example of complex anionic speciation." *Phys. Chem. Glasses* **42**(3):255-64.

Rao, KJ and MH Bhat. 2001b. "Investigation of lithium chloride-lithium borate-tellurium dioxide glasses: an example of complex anionic speciation." *Physics and Chemistry of Glasses - European Journal of Glass Science and Technology Part B* **42**(3):255-64.

Rojo, JM, J Sanz, JM Reau, and B Tanguy. 1990. "Influence of ion distribution on the ionic conductivity of lithium tellurite glasses (Li_2O-TeO_2 and LiF-TeO_2)." *Journal of Non-Crystalline Solids* **116**(2-3):167-74.

Sakida, S, S Hayakawa, and T Yoko. 2001. "^{125}Te, ^{27}Al, and ^{71}Ga NMR Study of M_2O_3–TeO_2 (M = Al and Ga) Glasses." *Journal of the American Ceramic Society* **84**(4):836-42, 10.1111/j.1151-2916.2001.tb00749.x.

Sakida, S, S Hayakawa, and T Yoko. 1999a. "Part 1. ^{125}Te NMR study of tellurite crystals." *Journal of Non-Crystalline Solids* **243**(1):1-12.

Sakida, S, S Hayakawa, and T Yoko. 1999b. "^{125}Te NMR Study of MO-TeO_2 (M=Mg, Zn, Sr, Ba and Pb) Glasses." *Journal of the Ceramic Society of Japan* **107**(5):395-402.

Sakida, S, S Hayakawa, and T Yoko. 1999c. "Part 2. ^{125}Te NMR study of M_2O-TeO_2 (M = Li, Na, K, Rb and Cs) glasses." *Journal of Non-Crystalline Solids* **243**(1):13-25.

Sekiya, T, N Mochida, and S Ogawa. 1994a. "Structural study of WO_3-TeO_2 glasses." *Journal of Non-Crystalline Solids* **176**(2-3):105-15.

Sekiya, T, N Mochida, and A Ohtsuka. 1994b. "Raman spectra of MO-TeO_2 (M = Mg, Sr, Ba and Zn) glasses." *Journal of Non-Crystalline Solids* **168**(1-2):106-14.

Shimizugawa, Y, T Maeseto, S Suehara, S Inoue, and A Nukui. 1995. "EXAFS and RDF studies of TeO_2–Li_2O glasses." *Journal of Materials Research* **10**(2):405-10.

Silva, MAP, Y Messaddeq, SJL Ribeiro, M Poulain, F Villain, and V Briois. 2001. "Structural studies on TeO_2-PbO glasses." *Journal of Physics and Chemistry of Solids* **62**(6):1055-60.

Tanaka, K, T Yoko, H Yamada, and K Kamiya. 1988. "Structure and ionic conductivity of $LiCl$-Li_2O-TeO_2 glasses." *Journal of Non-Crystalline Solids* **103**:250-56.

Yamamoto, H, H Nasu, J Matsuoka, and K Kamiya. 1994. "X-ray absorption fine structure (XAFS) study on the coordination of Te in PbO-TiO_2-TeO_2 glasses with high third-order optical non-linearity " *Journal of Non-Crystalline Solids* **170**(1):87-96.